LOW-TEMPERATURE MAGNETISM

Surface and bulk spin excitations in ferromagnetic semiconductor superlattices

V. A. Tanriverdiyev, V. S. Tagiyev, and S. M. Seyid-Rzayeva

Institute of Physics of the National Academy of Sciences of Azerbaijan, pr. Javida 33, Baku, Az-1143

The propagation of surface and bulk spin excitations in ferromagnetic semiconductor superlattices consisting of alternating monoatomic layers of two types of cubic Heisenberg ferromagnets is considered. The Green's function method is used to obtain the dispersion relations describing the propagation of surface and bulk spin waves in the superlattices and also the temperature dependence of the magnetization of the localized spins. The results are integrated numerically and presented graphically. © *2003 American Institute of Physics.*
[DOI: 10.1063/1.1630716]

The problems of synthesizing and studying superlattices (SLs) made up of alternating layers of different magnetic materials have been attracting a great deal of attention recently. Such superlattices have new physical properties differing considerably from those of the constituent materials themselves.[1,2]

Research on crystalline magnetic semiconductor materials has been widely reported,[3–5] while SLs made from these materials have been studied much less. Surface and bulk spin waves (SSWs and BSWs) in ferromagnetic semiconductor crystals both with narrow and with wide conduction bands were considered in Refs. 6 and 7 for all temperatures $T < T_c$ (T_c is the critical temperature). Some of the qualitative features of SLs can be explained most easily for the example of a simple cubic structure consisting of alternating monoatomic planes of different materials.

Examples of the fabrication of short-period SLs, their experimental study,[8,9] and theoretical model calculations based on the experiments are given in Refs. 10 and 11. Those papers considered the magnetic properties of SLs consisting of layers of magnetic insulators. It is clearly of practical interest to study SLs consisting of magnetic semiconductor materials.
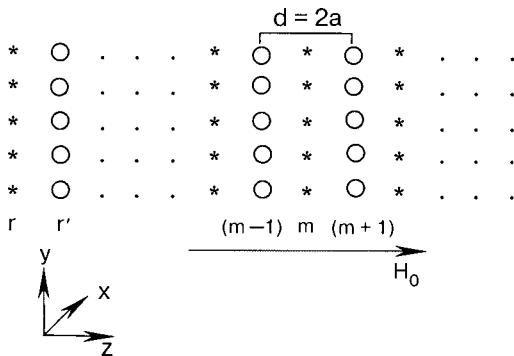

FIG. 1. Model of a semi-infinite superlattice consisting of alternating atomic layers of two different materials, the localized spins of which are represented by asterisks and circles, while the dots stand for a repetition of the unit cells of the superlattice.

In this paper we determine the regions of bulk spin waves, surface optical and acoustic modes, and the temperature dependence of the magnetization of the localized spins in semi-infinite simple cubic ferromagnetic semiconductor SLs. It is assumed that they are made up of monoatomic layers of material "1" alternating with monoatomic layers of material "2" and that each of these atomic layers lies in the [001] plane (Fig. 1).

1. HAMILTONIAN OF THE SYSTEM AND THE GREEN'S FUNCTION FOR LOCALIZED SPINS

In this Section we present calculations of the Green's function[12,13] for localized spins in ferromagnetic semiconductor SLs and use them to obtain the dispersion relations for BSWs at low temperatures in the narrow-band limit, where the exchange overlap integral t_{ij} for the conduction electrons is not taken into account. This approximation can be used when the relation $w \ll IS$ holds, where w is the width of the conduction band, I is the contact exchange integral, and S is the value of the localized spin.[4] In addition, we will give a relation for the temperature dependence of the localized magnetization of the SL layers.

The total Hamiltonian of the system under study is expressed as a sum of three terms: the Heisenberg Hamiltonian H_M for the localized spins (d and f types), the Hamiltonian H_E representing the kinetic and Zeeman energies of the conduction (s) electrons, and the Hamiltonian H_I of the $s-d$ ($s-f$) interaction:[6,7]

$$H = H_M + H_E + H_I, \tag{1}$$

$$H_M = -\frac{1}{2} \sum_{i,j} J_{i,j} S_i S_j - \sum_i g_i \mu_B H_0 S_i^z,$$

$$H_E = \sum_{i,j,\sigma} t_{i,j} a_{i\sigma}^+ a_{j\sigma} - g_e \mu_B H_0 \sum_i s_i^z,$$

$$H_I = -\sum_i I_i S_i s_i.$$

For studying the magnetic excitations of the system we introduce two Green's functions (one for the localized and one for the free electron spin operators), which are defined as $G_{i,j}(t)=\langle\langle S_i^+(t)|S_j^-(0)\rangle\rangle$ and $G'_{i,j}(t)=\langle\langle s_i^+(t)|S_j^-(0)\rangle\rangle$.

Using the Fourier transform of the Green's function in the random phase approximation, we can write the following combined equation:[6]

$$\begin{cases} \omega - g_i\mu_B H_0 - I_i\langle s_i^z\rangle - \dfrac{I_i^2\langle S_i^z\rangle\langle s_i^z\rangle}{\omega - g_e\mu_B H_0 - I_i\langle S_i^z\rangle} \\ \qquad - \sum_\delta J_{i,i+\delta}\langle S_{i+\delta}^z\rangle(\omega)\Bigg\} G_{i,j}(\omega) \\ \qquad + \langle S_i^z\rangle\sum_\delta J_{i,i+\delta}G_{i+\delta}(\omega) = 2\langle S_i^z\rangle\delta_{ij}. \end{cases} \quad (2)$$

Making use of the translational invariance in the xy plane, we define the Fourier transformation

$$G_{i,j}(\omega) = \frac{1}{N}\sum_{k_\parallel} G_{m,m'}(\omega,k_\parallel)\exp[ik_\parallel(r_i-r_j)], \quad (3)$$

where $k_\parallel=(k_x,k_y)$ is a two-dimensional wave vector parallel to the [001] plane, and m and m' are positive integers numbering the planes of the lattice, which contain sites i and j. The normalization constant N is the number of sites in each plane of the lattice.

Supposing that the mth layer consists of material "1" and the $(m+1)$th layer material "2" and taking (3) into account, we obtain from (2) the following system of equations:

$$\begin{cases} [\lambda_1(\omega)-4J_1\langle S_1^z\rangle\gamma(k_\parallel)]G_{m,m'}(\omega,k_\parallel)+J\langle S_1^z\rangle[G_{m-1,m'}(\omega,k_\parallel)+G_{m+1,m'}(\omega,k_\parallel)]=2\langle S_1^z\rangle\delta_{m,m'}, \\ [\lambda_2(\omega)-4J_2\langle S_2^z\rangle\gamma(k_\parallel)]G_{m+1,m'}(\omega,k_\parallel)+J\langle S_2^z\rangle[G_{m,m'}(\omega,k_\parallel)+G_{m+2,m'}(\omega,k_\parallel)]=2\langle S_2^z\rangle\delta_{m+1,m'}. \end{cases} \quad (4)$$

Here $\gamma(k_\parallel)=1-0.5(\cos k_x a+\cos k_y a)$,

$$\lambda_l(\omega)=\omega-g_l\mu_B H_0-I_l\langle s_l^z\rangle-2J\langle S_{l'}^z\rangle$$
$$\quad -\frac{I_l^2\langle S_l^z\rangle\langle s_l^z\rangle}{\omega-g_e\mu_B H_0-I_l\langle S_l^z\rangle}\quad (l,l'=1,2;\quad l'\neq l),$$

J_1 and J_2 are the exchange interactions between atoms of a layer consisting of material "1" and material "2," respectively, and J is the exchange interaction between adjacent atoms of different layers.

The system is periodic in the direction of the z axis with a lattice constant $d=2a$. According to the Bloch theorem, one can take $G_{m+2;(m+1),m'}(\omega,k_\parallel)=G_{m;(m-1),m'}(\omega,k_\parallel)$ $\times\exp(ik_z d)$.[11,14] Then the system of equations (4) can be written in matrix form:

$$\begin{pmatrix} \lambda_1(\omega)-4J_1\langle S_1^z\rangle\gamma(k_\parallel) & J\langle S_1^z\rangle[1+\exp(-ik_z d)] \\ J\langle S_2^z\rangle[1+\exp(-ik_z d)] & \lambda_2(\omega)-4J_2\langle S_2^z\rangle\gamma(k_\parallel) \end{pmatrix}$$
$$\times\begin{pmatrix} G_{m,m'}(\omega,k_\parallel) \\ G_{m+1,m'}(\omega,k_\parallel) \end{pmatrix}=\begin{pmatrix} 2\langle S_1^z\rangle\delta_{m,m'} \\ 2\langle S_2^z\rangle\delta_{m+1,m'} \end{pmatrix}. \quad (5)$$

The dispersion relation describing the propagate of BSWs along the axis of the SL can be obtained from Eq. (5):

$$16J_1J_2\langle S_1^z\rangle\langle S_2^z\rangle\gamma^2(k_\parallel)-4[J_2\langle S_2^z\rangle\lambda_1(\omega)$$
$$+J_1\langle S_1^z\rangle\lambda_2(\omega)]\gamma(k_\parallel)+\lambda_1(\omega)\lambda_2(\omega)$$
$$-2J\langle S_1^z\rangle\langle S_2^z\rangle(1+\cos k_z d)=0. \quad (6)$$

Equation (6) in the particular case when the two materials are identical, i.e., $J_1=J_2=J$, $I_1=I_2$, $\langle S_1^z\rangle=\langle S_2^z\rangle$, simplifies to the three-dimensional dispersion relation for ferromagnetic semiconductor crystals.[7]

Unlike the dispersion relation of second order in ω given in Ref. 7 for bulk ferromagnetic semiconductors, Eq. (6) is of fourth order. Consequently, the bulk spin-wave spectrum of the SL under study, both in the low- and high-energy regions, has two energy branches instead of one.

The poles of the Green's function, which determine the energies of the elementary excitations, are the roots of the following fourth-order equation:

$$\omega^4+c_1\omega^3+c_2\omega^2+c_3\omega+c_4=0. \quad (7)$$

where

$$c_1=-\varphi_1-\varphi_2-4\gamma(k_\parallel)(J_1\langle S_1^z\rangle+J_2\langle S_2^z\rangle),$$

$$c_2=\psi_1+\psi_2+\varphi_1\varphi_2+4\gamma(k_\parallel)[J_2\langle S_2^z\rangle(g_e\mu_B H_0+I_2\langle S_2^z\rangle$$
$$\quad +\varphi_1)+J_1\langle S_1^z\rangle(g_e\mu_B H_0+I_1\langle S_1^z\rangle+\varphi_2)]$$
$$\quad -2\langle S_1^z\rangle\langle S_2^z\rangle[8J_1J_2\gamma^2(k_\parallel)-J^2(1+\cos k_z d)],$$

$$c_3=-4J_2\langle S_2^z\rangle\gamma(k_\parallel)[\varphi_1(g_e\mu_B H_0+I_2\langle S_2^z\rangle)+\psi_1]$$
$$\quad -4J_1\langle S_1^z\rangle\gamma(k_\parallel)[\varphi_2(g_e\mu_B H_0+I_1\langle S_1^z\rangle)+\psi_2]$$
$$\quad -2\langle S_1^z\rangle\langle S_2^z\rangle[8J_1J_2\gamma^2(k_\parallel)-J^2(1+\cos k_z d)]$$
$$\quad \times[2g_e\mu_B H_0+I_1\langle S_1^z\rangle+I_2\langle S_2^z\rangle]-\varphi_1\psi_2-\psi_1\varphi_2,$$

$$c_4=\psi_1\psi_2+4J_2\langle S_2^z\rangle\gamma(k_\parallel)\psi_1(g_e\mu_B H_0+I_2\langle S_2^z\rangle)$$
$$\quad +4J_1\langle S_1^z\rangle\gamma(k_\parallel)\psi_2(g_e\mu_B H_0+I_1\langle S_1^z\rangle)+2\langle S_1^z\rangle\langle S_2^z\rangle$$
$$\quad \times[8J_1J_2\gamma^2(k_\parallel)-J^2(1+\cos k_z d)](g_e\mu_B H_0$$
$$\quad +I_1\langle S_1^z\rangle)(g_e\mu_B H_0+I_2\langle S_2^z\rangle),$$

$$\varphi_l=g_e\mu_B H_0+g_l\mu_B H_0+I_l\langle S_l^z\rangle+I_l\langle s_l^z\rangle$$
$$\quad +2J\langle S_{l'}^z\rangle\quad (l,l'=1,2;\ l\neq l'),$$

$$\psi_l=(g_l\mu_B H_0+I_l\langle S_l^z\rangle+2J\langle S_{l'}^z\rangle)(g_e\mu_B H_0+I_l\langle S_l^z\rangle)$$
$$\quad -I_l^2\langle S_l^z\rangle\langle s_l^z\rangle.$$

We denote the four solutions of equation (7) as ω_{kl} ($l = \overline{1,4}$, $k = (k_\parallel, k_z)$). Then the expressions for the Green's function can be written in the form[11,14]

$$G_{m,m}(\omega_k) = \sum_{l=1}^{4} a_1(\omega_k)/(\omega_k - \omega_{kl}), \quad G_{m+1,m+1}(\omega_k)$$

$$= \sum_{l=1}^{4} a_2(\omega_k)/(\omega_k - \omega_{kl}), \quad (8)$$

$$a_{1;(2)}(\omega_{kl}) = 2\langle S^z_{1;(2)}\rangle[\lambda_{2;(1)}(\omega_{kl}) - 4J_{2;(1)}$$

$$\times \langle S^z_{2;(1)}\rangle \gamma(k_\parallel)]/\prod_{l'}(\omega_{kl} - \omega_{kl'}) \quad (l \neq l').$$

At low temperatures the local magnetization of the mth layer can be obtained from the relation[15,16]

$$\frac{\mu_m(T)}{\mu_m(0)} = 1 - \frac{i}{2\pi}\lim_{\tau \to 0}\left[\sum_{k \in B,Z}\right.$$

$$\left.\times \int \frac{G_{m,m'}(\omega_k + i\tau) - G_{m,m'}(\omega_k - i\tau)}{\exp(\omega_k/k_B T) - 1}d\omega_k\right]. \quad (9)$$

Using (9) and the Dirac relation[12]

$$\lim_{\tau \to 0}\left[\frac{1}{\omega_k - i\tau} - \frac{1}{\omega_k + i\tau}\right] = 2\pi i\,\delta(\omega_k),$$

we obtain

$$\frac{\mu_m(T)}{\mu_m(0)} = 1 - \sum_{l=1}^{4}\sum_{k \in B,Z}\frac{a_1(\omega_{kl})}{\exp(\omega_{kl}/k_B T) - 1},$$

$$\frac{\mu_{m+1}(T)}{\mu_{m+1}(0)} = 1 - \sum_{l=1}^{4}\sum_{k \in B,Z}\frac{a_2(\omega_{kl})}{\exp(\omega_{kl}/k_B T) - 1}. \quad (10)$$

2. SURFACE SPIN WAVES IN SEMI-INFINITE FERROMAGNETIC SEMICONDUCTOR SUPERLATTICES

It is known that surface effects influence the character of the behavior of magnetic systems and can substantially alter the magnetic properties of materials.[17,18] In some cases this leads to the formation of a macroscopically ordered structure even at temperatures above the critical temperature in the bulk of the sample. Of particular interest is the study of surface excitations in different infinite or semi-infinite magnetically ordered systems. These studies have been carried out for insulating magnetic SLs in the framework of the Heisenberg exchange model,[19,20] and it was shown that in addition to the bulk spin excitations there are also surface ones. The amplitudes of surface spin excitations are in principle localized on the surface or near it and fall off with distance from the surface into the interior of the system.[17,21] Acoustic SSWs have a constant phase, while optical SSWs have a phase change of 180° in going from one layer to another.

We assume that the surface layer in the semi-infinite ferromagnetic semiconductor SL consists of a material r ($r = 1,2$) and the second layer, of a material r' ($r' \neq r$, $r' = 1,2$). Then, by analogy with the procedure used to obtain (4), we can write the following system of equations for the surface layer and the layers neighboring it:

$$\begin{cases}
[\lambda_s(\omega) - 4J_s\langle S^z_s\rangle\gamma(k_\parallel)]G_{1,m'} + J\langle S^z_s\rangle G_{2,m'} \\
\quad = 2\langle S^z_s\rangle\delta_{1,m'}, \\
[\lambda_{r'}(\omega) - 4J_{r'}\langle S^z_{r'}\rangle\gamma(k_\parallel)]G_{2,m'} + J\langle S^z_{r'}\rangle(G_{1,m'} + G_{3,m'}) \\
\quad = 2\langle S^r_{r'}\rangle\delta_{2,m'}, \\
[\lambda_r(\omega) - 4J_r\langle S^z_r\rangle\gamma(k_\parallel)]G_{3,m'} + J\langle S^z_r\rangle\left(1 + \frac{1}{x}\right)G_{2,m'} \\
\quad = 2\langle S^z_r\rangle\delta_{3,m'},
\end{cases} \quad (11)$$

where $x = \exp(-ik_z d)$,

$$\lambda_s(\omega) = \omega - g_r\mu_B H_0 - I_s\langle s^z_s\rangle - J\langle S^z_{r'}\rangle - I^2_s\langle S^z_s\rangle\langle s^z_s\rangle/$$

$$(\omega - g_e\mu_B H_0 - I_s\langle S^z_s\rangle).$$

Using Eqs. (6) and (11) with allowance for the relation $\cos k_z d = (x + x^{-1})/2$, we obtain a dispersion relation linear in $\gamma(k_\parallel)$ for the SSWs:

$$\lambda_s(\omega_s)(x + 1)\langle S^z_r\rangle - \lambda_r(\omega_s)\langle S^z_s\rangle - 4\langle S^z_s\rangle\langle S^z_r\rangle$$

$$\times[J_s(1 + x) - J]\gamma(k_\parallel) = 0, \quad (12)$$

where $x = x(\omega_s)$ is the root of the cubic equation

$$d_1 x^3 + d_2 x^2 + d_3 x + d_4 = 0, \quad (13)$$

$$d_1 = -J^2 J^2_s\langle S^z_s\rangle^2\langle S^z_r\rangle^2\langle S^z_{r'}\rangle,$$

$$d_2 = \langle S^z_r\rangle[\lambda_{r'}(\omega_s)J_s\langle S^z_s\rangle - \lambda_s(\omega_s)J_{r'}\langle S^z_{r'}\rangle]$$

$$\times[\lambda_r(\omega_s)J_s\langle S^z_s\rangle - \lambda_s(\omega_s)J_r\langle S^z_r\rangle] - J^2 J_s(3J_s - 2J_r)$$

$$\times\langle S^z_s\rangle^2\langle S^z_r\rangle^2\langle S^2_{r'}\rangle,$$

$$d_3 = [\lambda_{r'}(\omega_s)\langle S^z_s\rangle\langle S^z_r\rangle(J_s - J_r) + J_{r'}\langle S^z_{r'}\rangle(\langle S^z_s\rangle\lambda_r(\omega_s)$$

$$- \langle S^z_r\rangle\lambda_s(\omega_s))][J_s\langle S^z_s\rangle\lambda_r(\omega_s) - J_r\langle S^z_r\rangle\lambda_s(\omega_s)]$$

$$- J^2(3J^2_s + J^2_r - 4J_s J_r)\langle S^z_s\rangle^2\langle S^z_r\rangle^2\langle S^z_{r'}\rangle,$$

$$d_4 = -J^2(J_s - J_r)^2\langle S^z_s\rangle^2\langle S^z_r\rangle^2\langle S^z_{r'}\rangle.$$

Equation (13) was obtained by eliminating $\gamma(k_\parallel)$ from Eqs. (6) and (11) and then transforming them with respect to x. In the case $x > 1$ the roots of Eq. (13) describe acoustic surface modes, for $x < -1$, optical modes, and for $|x| = 1$, BSWs.[17]

3. QUANTITATIVE RESULTS AND THEIR DISCUSSION

In this Section we present numerical calculations based on the theoretical results obtained. The dependence of $\omega/6J_1\langle S^z_1\rangle$ on $\gamma(k_\parallel)$ given in Fig. 2a for the bulk materials "1" and "2" was obtained by the method described in Ref. 7. Bulk spin waves propagating in the SL along the z axis appear in the region $[0; \pi/d]$ of the wave vector k_z. Using dispersion relation (6), we can in the same way construct the BSW bands for the SL under consideration (see Fig. 2b). It is seen that the BSW region is observed in two frequency ranges, low and high. The width of the BSW region in a SL depends on the transverse component of the wave vector, the exchange interaction between localized spins, and the $s-d$ or $s-f$ exchange interaction with the spins of the conduction electrons. With increasing exchange interaction between the
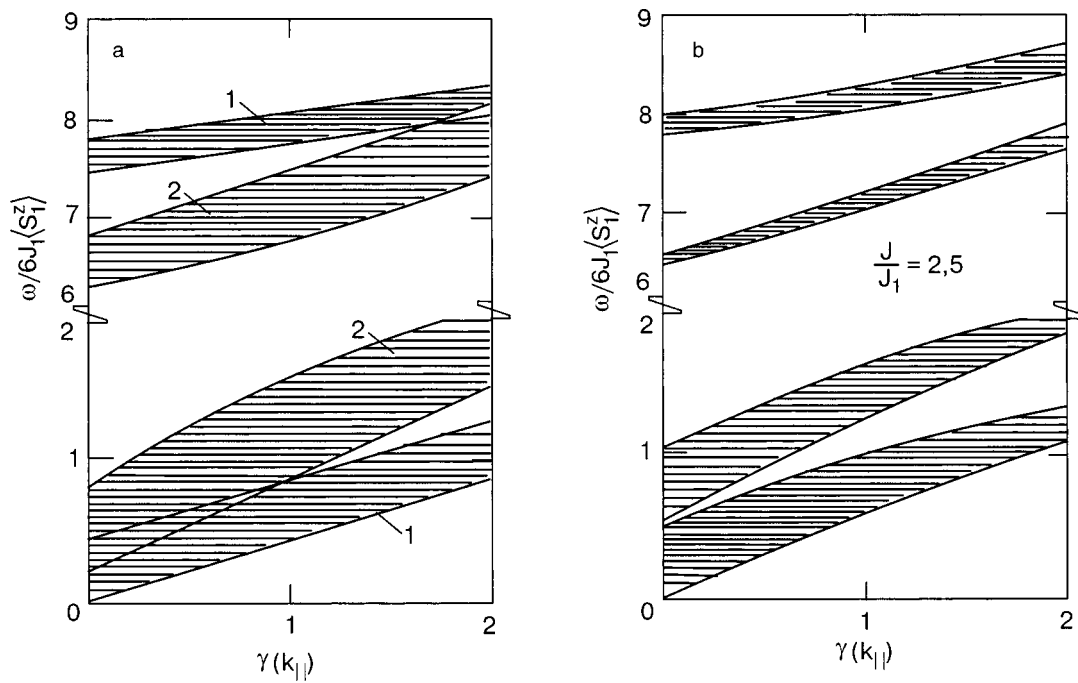
FIG. 2. The bulk spin-wave regions for the materials "1" and "2" which make up the superlattice (a), and for a ferromagnetic semiconductor SL with $J/J_1=2.5$ (b) for the following parameter values: $g_1\mu_B H_0/J_1\langle S_1^z\rangle=0.3$, $g_2=g_e=0.4g_1$; $\langle S_1^z\rangle=\langle S_2^z\rangle=1$; $\langle s_1^z\rangle=\langle s_2^z\rangle=0.5$; $J_2/J_1=2$; $I_1/J_1=30$; $I_2/J_1=25$.

layers of different materials making up the SL, the width of the bands increases. In addition, they are shifted to higher energies as the exchange coupling becomes stronger. In the case when the exchange interactions between the localized spins and the spins of the conduction electron differ strongly in materials "1" and "2," then the gap between the allowed regions increases strongly.

Selecting those roots of equation (13) which satisfy the conditions $x>1$ and $x<-1$, corresponding to acoustic and optical SSWs, and then taking their dispersions (12) into account, one can construct curves describing the surface spin waves (see Fig. 3). It is seen that the acoustic and optical SSWs appear both in the low- and high-frequency regions. The number of acoustic and optical branches can vary de-
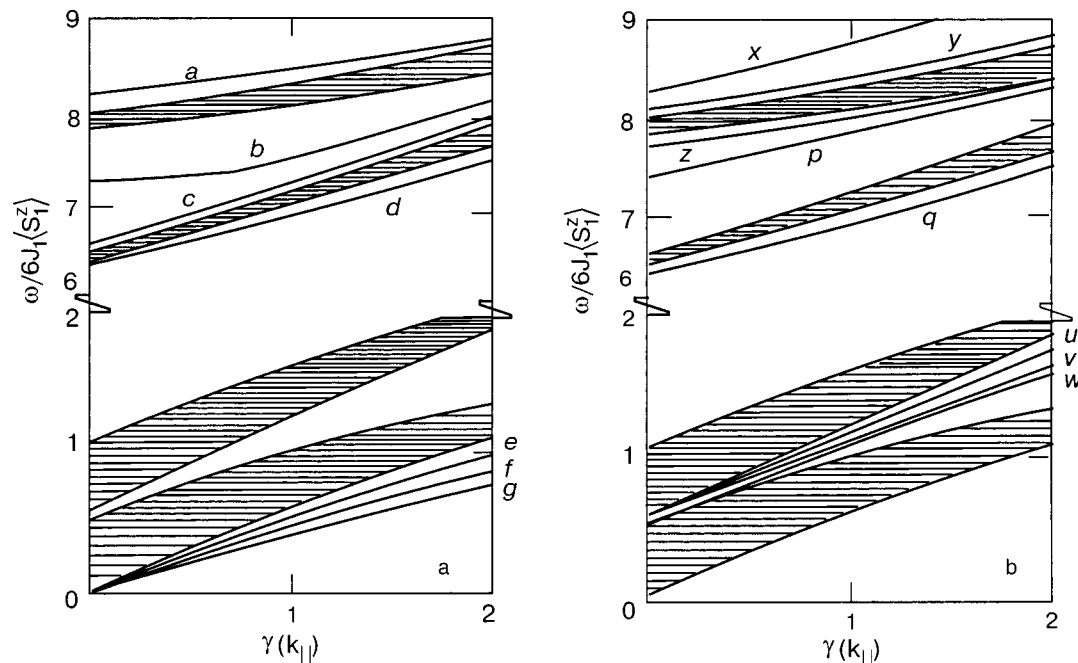

FIG. 3. Dispersion curves for surface spin waves in a semi-infinite ferromagnetic semiconductor superlattice. The shaded part is the bulk spin wave region, and the parameters not pertaining to the surface were chosen in accordance with Fig. 2b. a) For the case when the surface consists of material "1": acoustic branches a, d, e, f, and g correspond to values of the ratio $I_s/J_1=32$, 29, 32, 29, 10; the optical branches b and c to $I_s/J_1=29$, 10; b) for the case when the surface consists of material "2": acoustic branches x, y, q correspond to the values $I_s/J_1=32$, 29, 24; optical branches z, p, u, v, w to $I_s/J_1=32$, 29, 32, 29, 24, respectively. In all cases we took $\langle S_s^z\rangle=\langle S_1^z\rangle=\langle S_2^z\rangle$, $J_s=J_r$ ($r=1,2$).
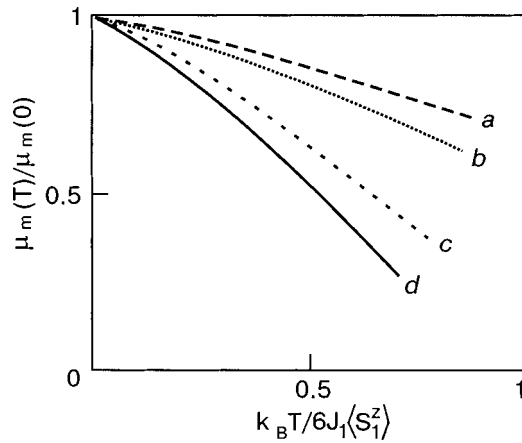
FIG. 4. Temperature dependence of the magnetization of localized spins of a superlattice for the case $g_1 \mu_B H_0 / J_1 \langle S_1^z \rangle = 0.05$; $g_1 = g_2 = g_e$; $J/J_1 = 0.5$; $\langle S_1^z \rangle = S_2^z \rangle = 1$, $\langle s_1^z \rangle = \langle s_2^z \rangle = 0.5$; branches *a* and *b* correspond to the values $I_1/J_1 = I_2/J_1 = 12$, and branches *c* and *d* to values $I_1/J_1 = I_2/J_1 = 8$. The solid curve gives the magnetization of the spins of a layer of material "1," and the dashed curve that for material "2."

pending on the choice of parameter values. For the parameter values indicated in Fig. 3, if a material with a weak $d-d$ or $f-f$ exchange interaction is found at the boundary, then in the low-frequency region only acoustic modes appear (Fig. 3a), while in the opposite case, only optical modes appear (Fig. 3b). In addition, the optical spin branches lie in the space between BSW bands. If the $s-d$ $(s-f)$ contact exchange interaction in the layers found at the boundary is strongly different from that inside the SL, the curves corresponding to the SSWs are strongly separated from the BSW bands.

Figure 4 shows the temperature dependence of the local magnetization in the high-temperature limit. The fourth-order equation (7) is relatively easily solved if it is assumed that $g_1 = g_2 = g_e$, $\langle S_1^z \rangle = \langle S_2^z \rangle$, $\langle s_1^z \rangle = \langle s_2^z \rangle$, and $I_1 = I_2$. Taking the roots of equations (7) and (8) and expressions (10) into account and then performing the summation over the first Brillouin zone $(0 \leq k_x \leq \pi/a, 0 \leq k_y \leq \pi/a, 0 \leq k_z \leq \pi/d)$,

one can construct the temperature dependence of the magnetization. The magnetization is significantly larger in the layers of the material with the stronger exchange between localized spins, and at high temperatures it naturally tends toward zero. The magnetization of the layers also increases with increasing exchange interaction between ions belonging to different layers of the SL. In addition, with weakening of the $s-d$ $(s-f)$ interaction the local magnetization also decreases and tends toward zero at lower temperatures.

[1] M. G. Cottam and D. R. Tilley, *Introduction to Surface and Superlattice Excitations*, Cambridge University Press, Cambridge (1989).
[2] R. E. Camley and R. L. Stamps, J. Phys.: Condens. Matter **5**, 3727 (1993).
[3] Tomasz Dietl, Semicond. Sci. Technol. **17**, 377 (2002).
[4] É. L. Nagaev, *Physics of Magnetic Semiconductors* [in Russian], Nauka, Moscow (1979).
[5] V. Yu. Irkhin, Fiz. Tverd. Tela (Leningrad) **28**, 3066 (1986) [Sov. Phys. Solid State **28**, 1725 (1986)].
[6] J. M. Wesselinova, E. Kroumova, N. Teofilov, and W. Nolting, Phys. Rev. B **57**, 6508 (1998).
[7] Sudha Gopalan and M. G. Cottam, Phys. Rev. B **42**, 10311 (1990).
[8] R. Du, F. Tsui, and C. P. Flynn, Phys. Rev. B **38**, 2941 (1988).
[9] J. J. Chen, G. Dresselhaus, M. S. Dresselhaus, G. Sprinhoulz, C. Picher, and G. Bauer, Phys. Rev. B **54**, 402 (1996).
[10] Yi-fang Zhou and Tsung-han Lin, Phys. Lett. A **134**, 257 (1989).
[11] H. T. Diep, Phys. Lett. A **138**, 69 (1989).
[12] D. N. Zubarev, Usp. Fiz. Nauk **71**, 1 (1960) [Sov. Phys. Usp. **3**, 320 (1960)].
[13] S. V. Tyablikov, *Methods in the Quantum Theory of Magnetism*, 1st ed., Plenum Press, New York (1967), Nauka, Moscow (1965).
[14] V. A. Tanriverdiyev, V. S. Tagiyev, and M. B. Guseynov, Transactions, Azerbaijan Academy of Sciences **2**, 45 (2000).
[15] Song-Tao Dai and Zhen-Ya Li, Phys. Lett. **146**, 450 (1990).
[16] A. Mauger and D. L. Mills, Phys. Rev. B **29**, 3815 (1983).
[17] T. Wolfram and R. E. DeWames, Prog. Surf. Sci. **2**, 233 (1972).
[18] J. H. Baskey and M. G. Cottam, Phys. Rev. B **42**, 4304 (1990).
[19] Feng Chen and H. K. Sy, J. Phys.: Condens. Matter **7**, 6591 (1995).
[20] V. A. Tanriverdiyev, V. S. Tagiyev, and S. M. Seyid-Rzayeva, Fizika (Baku) **6**, 28 (2000).
[21] R. E. DeWames and T. Wolfram, Phys. Rev. **185**, 720 (1969).

Translated by Steve Torstveit

Low-temperature magnetic properties of the monoclinic magnet RbDy(WO$_4$)$_2$

E. N. Khatsko,* A. S. Cherny, and A. I. Rykova

B. Verkin Institute for Low Temperature Physics and Engineering, National Academy of Sciences of Ukraine, pr. Lenina 47, 61103 Kharkov, Ukraine

M. T. Borowiec and H. Szymczak

Institute of Physics of the Polish Academy of Sciences, Al. Lotnikow 32/46, 02-688, Warsaw, Poland

V. P. Dyakonov

*Institute of Physics of the Polish Academy of Sciences, Al. Lotnikow 32/46, 02-688, Warsaw, Poland;
A. A. Galkin Donetsk Physicotechnical Institute, ul. R. Lyuksemburg 72, 83114 Donetsk, Ukraine*

The temperature dependence of the magnetic susceptibility along the principal magnetic axes of rubidium–dysprosium tungstate RbDy(WO$_4$)$_2$ is measured in the temperature interval 0.5–300 K. Strong anisotropy of the susceptibility is observed at all temperatures in that range. At $T_N = 0.8$ K the susceptibility along all three magnetic axes exhibits a sharp anomaly due to the phase transition to a magnetically ordered state. At 0.5 K the measured field dependence of the magnetization along all three axes demonstrates a metamagnetic orientational phase transition in the directions of the magnetic axes y and z. Another type of anomaly of the magnetic susceptibility is observed at temperatures of around 5, 8, and 50 K. Analysis shows that these anomalies correspond to structural phase transitions in this compound. © *2003 American Institute of Physics.* [DOI: 10.1063/1.1630717]

INTRODUCTION

Double molybdates and tungstates of the type MR(XO$_4$)$_2$, where M is a monovalent alkali-metal ion, R is a rare-earth ion, and X is molybdenum or tungsten, form a wide class of substances, including a number of families with different symmetry of the crystal structure, from tetragonal to triclinic. This class is of interest in connection with a number of features due to the low symmetry of the crystal lattice, the small value of the exchange, the significant contribution from the dipole–dipole interaction of the magnetic ions, the low dimensionality of the magnetic structure, and the competition between magnetic and electric interactions, which determines the energy spectrum of the magnetic ion and its features.

The layered structure and the strong electron–phonon interaction, together with a degenerate or quasidegenerate electronic ground state, make these compounds structurally unstable; they typically exhibit several structural phase transitions induced by weak external fields (temperature or magnetic), often due to the cooperative Jahn–Teller effect. For such structural transitions, as a rule, a lowering of the symmetry of the system and a rearrangement of the energy spectrum of the magnetic ion occur, and that should be reflected in features in such properties as the magnetic susceptibility. A peculiarity of the structural transitions in these systems is the rather low (in the present case, monoclinic) symmetry of the initial high-temperature state.

SAMPLES AND EXPERIMENTAL TECHNIQUE

The compound RbDy(WO$_4$)$_2$ investigated in the present study is a representative of the double alkali–rare-earth tung-

states; at room temperature it has monoclinic symmetry, isostructural to KY(WO$_4$)$_2$ (Ref. 1), space group C_{2h}^6, with the following unit cell parameters: $a = 10.66$ Å, $b = 10.45$ Å, $c = 7.569$ Å, monoclinic angle $\beta = 130°27'$ (Refs. 2 and 3). The unit cell contains four molecules. It should be noted that at a temperature of 820 °C (the melting point of RbDy(WO$_4$)$_2$ $t_{melt} = 1120$ °C) the crystal undergoes a polymorphous transformation from the α to the β modification.[3] Figure 1 shows a fragment of the crystal structure of RbDy(WO$_4$)$_2$ at room temperature.[1] It is seen that the magnetic ions Dy^{3+}, which are surrounded by oxygen octahedra, form planes which are separated by Rb$^-$ planes, which in turn are surrounded by oxygen polyhedra. Thus the structure of the magnetic ions is substantially two-dimensional just for crystallographic reasons. The ground state of the Dy^{3+} ion is $^6H_{15/2}$. In the crystalline field of monoclinic symmetry the degeneracy is lifted, and the multiplet is split into eight Kramers doublets.

Samples of the RbDy(WO$_4$)$_2$ single crystals were grown by crystallization from the flux at a programmed rate of cooling, and also by a modified Czochralski method. The single crystals grown were transparent, yellow in color, and naturally faceted. The samples were oriented with the aid of an x-ray diffractometer.

The magnetic properties of the RbDy(WO$_4$)$_2$ single crystal were investigated in the temperature range 0.5–300 K in magnetic fields up to 20 kOe.

The temperature dependence of the principal values of the magnetic susceptibility of the RbDy(WO$_4$)$_2$ single crystal were investigated in the temperature range 0.5–300 K. In the temperature region 1.8–300 K we used the Faraday
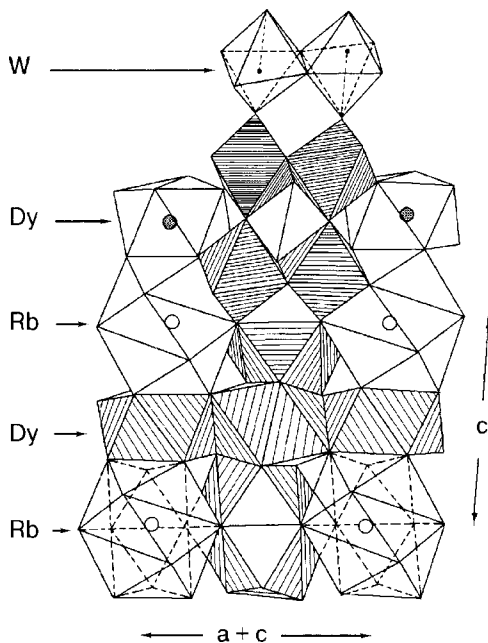
FIG. 1. Fragment of the crystal structure of $RbDy(WO_4)_2$ (Ref. 1).

FIG. 2. Temperature dependence of the principal magnetic susceptibilities of the $RbDy(WO_4)_2$ single crystal in the temperature range 0.5–300 K.

method with self-compensation and the possibility of rotating the magnetic field relative to the sample, making it possible to find the directions of the magnetic axes of the crystal. In the temperature region 0.5–4.2 K the susceptibility measurements were made by induction methods and also with the use of a vibrating magnetometer.[4] The temperature was regulated by pumping on ^{3}He vapor. The magnetization along the principal magnetic axes was investigated using a vibrating magnetometer in static magnetic fields up to 20 kOe.

EXPERIMENTAL RESULTS

A study of the angular dependences of the magnetic susceptibility of the $RbDy(WO_4)_2$ single crystal in two mutually perpendicular planes made it possible to determine the directions of the principal magnetic axes of the $RbDy(WO_4)_2$ crystal. The magnetic axis y coincides with the crystallographic axis b. The magnetic axes x and z lie in the plane perpendicular to the b axis, and the z axis is inclined to the c axis by an angle $\phi = 12°$.

Figures 2 and 3 show the temperature dependence of the magnetic susceptibility χ along the principal magnetic axes of the $RbDy(WO_4)_2$ single crystal in the temperature range 0.5–300 K.

It is seen that $RbDy(WO_4)_2$ has strongly anisotropic magnetic properties at all temperatures in this range. This anisotropy is due to the effect of the low-symmetry crystalline field on the Dy^{3+} ions.

The temperature dependence of the inverse magnetic susceptibility $1/\chi$, shown in Fig. 3, can be separated into several temperature regions. In the interval 300–50 K the $1/\chi(T)$ curves are well described by straight lines, i.e., they obey the Curie–Weiss law: $\chi_i = C_i/(T - \Theta_i)$. One notices the different signs of the Curie–Weiss constants Θ_i for the different magnetic axes. This attests to a different character of the spin–spin interaction along the different magnetic directions: ferromagnetic along the y axis, and antiferromag-
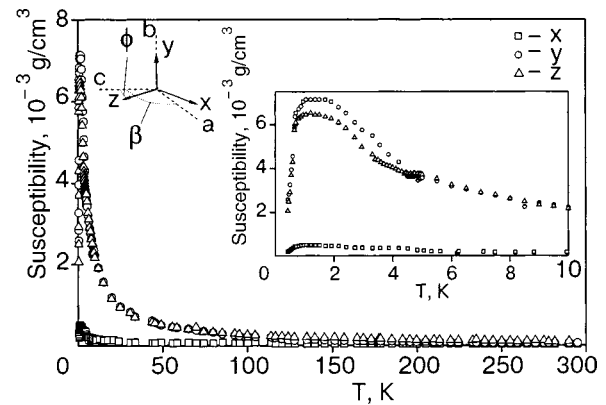
netic along the x and z axes. At 50 K a sharp kink appears on the $1/\chi_x(T)$ and $1/\chi_y(T)$ curves, and the anisotropy between the y and z axes vanishes. In the interval 50–5 K the Curie–Weiss law is obeyed, as before, but with different interaction constants. In the region 5–10 K two more anomalies of the magnetic susceptibility are observed, at 5 K and around 8 K. The $y-z$ anisotropy reappears, and the Curie–Weiss law with new constants holds down to ~ 2 K. Finally, below helium temperatures (Fig. 2), at $T_{mpt} = 0.8$ K, the susceptibility along all three magnetic axes exhibits a sharp anomaly typical for a phase transition to a magnetically ordered state. The transition temperature is determined from the maximum of the derivative $d\chi/dT$. This value is in good agreement with the heat-capacity data.[5] Above the temperature of the transition to the magnetically ordered state, in the region 1–2 K, broad maxima of χ are observed along all three magnetic axes.

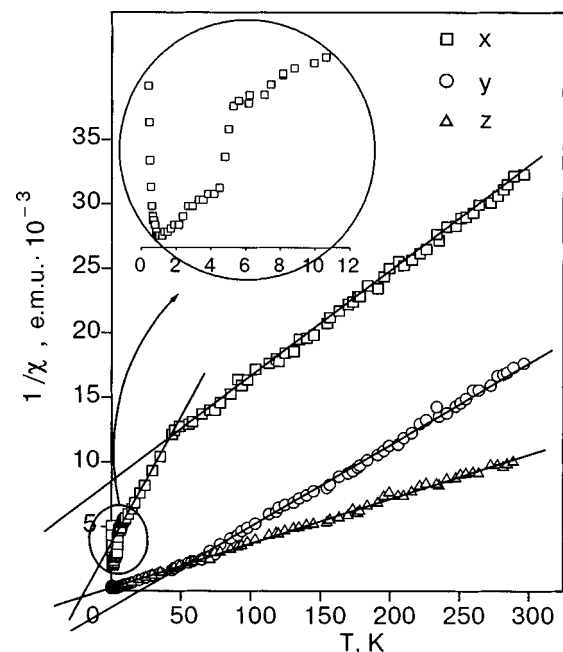We also investigated the field dependence of the magnetization **M** of the $RbDy(WO_4)_2$ single crystal along the prin-

FIG. 3. Temperature dependence of the inverse magnetic susceptibilities of the single crystal $RbDy(WO_4)_2$ in the temperature range 0.5–300 K.
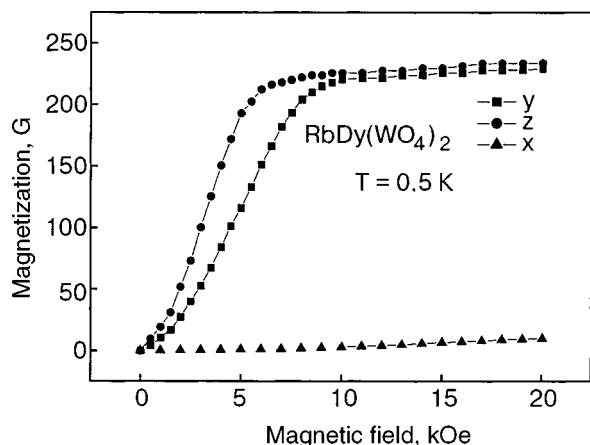
FIG. 4. Field dependence of the magnetization along the principal magnetic axes of the RbDy(WO$_4$)$_2$ single crystal at 0.5 K.

cipal magnetic axes over a wide range of temperatures. Figure 4 shows the results for a temperature $T=0.5$ K. When an external magnetic field is imposed along the magnetic axes y and z the magnetic moment increases rapidly and goes to saturation. The saturation moment along these axes has approximately the same value ≈ 224 G. Along the magnetic axis x the $M(H)$ curve remains linear to the maximum field, around 20 kOe, and the value of this moment remains small in comparison to the values for the other axes all the way to the highest magnetic fields used in the experiment ($M_{y(z)}/M_x \sim 24$ at 20 kOe). No hysteresis of $M(H)$ is observed. Above 4 K the dependence of the magnetization on the applied external magnetic field has a typically paramagnetic character.

DISCUSSION OF THE RESULTS

Since above helium temperatures the field dependence of the magnetization does not reveal the presence of a magnetically ordered state, and the temperature dependence of the susceptibility is described satisfactorily by the Curie–Weiss law, one can say that the sample is found in a paramagnetic state. In that case the susceptibility anomalies (and, hence, the rearrangement of the energy spectrum of the Dy^{3+} ion) are due not to magnetic but to structural phase transitions. It should be noted that the transition at 5 K is confirmed by measurements of the heat capacity[6] and EPR spectra.[7] Structural studies are needed to determine the symmetry of the low-temperature phase. The anomaly in the 8K region is apparently also due to a structural transition, which is observed in optical and thermal measurements,[6,8,9] but it is much less pronounced, apparently because it entails a much weaker rearrangement of the energy spectrum. The transition in the 50 K region has not been observed before.

Although RbDy(WO$_4$)$_2$ is paramagnetic at all temperatures above 2 K in the range investigated, the magnetic characteristics responsible for the transition to the magnetically ordered state at 0.8 K are determined by the temperature region below 5 K, i.e., below the last structural transition. From the data on the temperature dependence of the principal magnetic susceptibilities in this region, one can find the constants in the Curie–Weiss law $\chi = C_i/(T+\Theta_i)$:

$C_x=0.000362$ cm^3 k/g, $C_y=0.00556$ cm^3 k/g,

$C_z=0.0025$ cm^3 k/g,

$\Theta_x=-2.3$ K, $\Theta_y=-0.6$ K, $\Theta_z=-0.8$ K.

Using these data and the relation

$$C_i=[Ng_i^2\mu_B{}^2 S(S+1)]/3k, \tag{1}$$

where N is the number of spins per unit volume, μ_B is the Bohr magneton, S is the effective spin, equal to 1/2, and k is Boltzmann's constant, we can estimate the principal values of the g factors:

$$g_x=0.6, \quad g_y=2.38, \quad g_z=1.59.$$

These values differ substantially from the experimental values obtained in the EPR studies, both ours: $g_x=0.8$, $g_y=8.7$, $g_z=2.65$ and the estimated values obtained in Ref. 7. It should be noted that the EPR data attest to the presence of two nonequivalent magnetic centers, rotated in the yz plane by an angle close to 45°. The presence of two nonequivalent centers is characteristic for this class of crystals, which have a crystal lattice with four rare-earth ions in the unit cell.

A difference between the g factors obtained from susceptibility and EPR measurements is generally not surprising, since all the occupied energy levels of the magnetic ion contribute to the magnetic susceptibility, while the EPR characteristics are determined predominantly by the properties of the lowest doublet of the cobalt ion. In the present case this apparently means that the end levels of the dysprosium ion are not very high-lying and give a substantial contribution to the susceptibility. Unfortunately, in our case relation (1), from which the g factors were determined, ceases to hold exactly (it is valid under the condition that only the lowest Kramers doublet of those arising in the splitting of the $^6H_{15/2}$ state of the Dy^{3+} ion under the influence of the spin–orbit interaction and the crystalline field is occupied), and the estimates obtained for the g factors can only be regarded as rough estimates. For an exact calculation of the magnetic susceptibility in this case one needs to know the structure of the spectrum of the dysprosium ion, and that requires optical studies.

The transition to the magnetically ordered state occurs at $T=0.8$ K. The transition occurs to an antiferromagnetic state, since the negative values of the Curie constant Θ_i indicate an antiferromagnetic character of the exchange interaction along all three magnetic directions. A characteristic feature of the temperature dependence of the principal values of the magnetic susceptibility tensor of RbDy(WO$_4$)$_2$ is the presence of broad maxima of $\chi_i(T)$ above the transition temperature T_{mpt}. Generally speaking, such maxima are characteristic for low-dimensional magnets, although the question of low dimensionality of this magnetic system requires special examination, particularly since the Curie constants Θ_i obtained are not very different.

The low value of T_{mpt} indicates a small value of the exchange interaction between the Dy^{3+} ions, and it can be assumed that the contribution of the dipole–dipole interaction to the magnetic properties of this compound should be appreciable.

The energy of the magnetic dipole–dipole interaction between nearest neighbors can be estimated with the use of

the standard equation: $E_{dd} = -2Zg^2\mu_B^2/R^3$, where $Z=4$ for the a plane, $g \approx 2$, and $R \approx 4$ Å is the distance between neighboring ions. The estimated value of E_{dd} is around 0.3 K. With this value an estimate of the exchange interaction from the value of T_c in the molecular field model gives

$$J/k \approx T_c/[Zs(s+1)] \approx 0.27.$$

We see that the contribution of the dipole–dipole interaction to the spin–spin interaction is rather large. Unfortunately, the lack of data on the low-temperature structure of RbDy(WO$_4$)$_2$ does not permit a more precise calculation of the dipole–dipole contribution to the Dy–Dy interaction.

Let us consider the field dependence of the magnetization of RbDy(WO$_4$)$_2$ in the ordered state. As we have said, the magnetization along the magnetic axis x is small compared to that along y and z, indicating that the moments lie in the yz plane, which according to the experiment is rotated by $12°$ relative to the crystallographic plane bc. When a magnetic field is imposed along the magnetic axes y and z, one observes a rapid nonlinear growth of the magnetization with saturation in fields of around 10 kOe for the y axis and 6 kOe for the z axis. A magnetic-field-induced orientational phase transition occurs. In an antiferromagnet, depending on the relationship between the exchange energy E_E and the anisotropy energy E_A, this can be either a spin-flop transition ($E_E \gtrsim E_A$) or a metamagnetic transition ($E_E < E_A$). In a metamagnet the orientation of the magnetic moments is rigidly specified by the anisotropy fields, and the orientational phase transition occurs by hops of the magnetic moments from one allowed position to another when the energy of the external magnetic field exceeds the exchange field. In that case the transition can be either second-order (the magnetization changes continuously, and there is no hysteresis) or first-order (there is a jump in magnetization, and hysteresis is observed); see, e.g. Refs. 10 and 11. The second-order transition occurs below the ordering temperature but above the triple point, at which it gives way to a first-order transition. The shape of the sample and its finite size lead to demagnetizing fields, which smear the picture, so that the transition at a given temperature occurs not at a point but in an interval of fields on account of the demagnetizing factors. The width of the interval in which the metamagnetic phase transition occurs through a mixed state consisting of a mixture of regions of the flipped and unflipped phases is determined by the geometry of the sample. The demagnetizing factors can be estimated from the experimental data ($\delta H/\delta M = 4\pi N_i$). They are found to be $N_y \approx 2.5$ and $N_z \approx 1.6$. Unfortunately, however, since the shape of the samples was irregular and multifaceted, far from the simple bodies for which the demagnetizing factors can be calculated (ellipsoids, cylinders, planes), we cannot make any estimates of the field interval.

Based on all we have said and in view of the presence of strong single-ion anisotropy due to the low symmetry of the crystalline field, we assume that the observed transition is metamagnetic. Judging from the form of the $M(H)$ curves, the proximity of the temperature at which it is observed to the magnetic ordering temperature and the absence of any hysteresis, we can assume that it is a second-order transition.

The existence of a significant magnetic moment along both the y and z directions and the practical absence of a
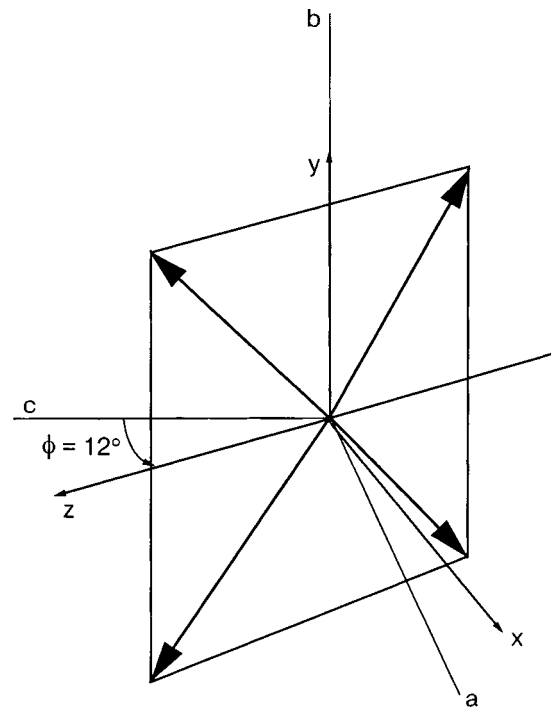

FIG. 5. Proposed magnetic structure of RbDy(WO$_4$)$_2$.

moment along the x axis indicate that the moments of the sublattices lie in the yz plane. Further, the fact that the behavior of $M(H)$ is about the same and the values of the saturation magnetization are the same along the y and z axes suggests that the projections of the moment along these magnetic axes are equal. No kind of collinear magnetic structure can account for this. Consequently, the magnetic structure realized in RbDy(WO$_4$)$_2$ must be noncollinear, with moments lying in the yz plane. This means that the moments of the sublattices deviate from the magnetic axes (both y and z) by an appreciable angle. Taking into account that the RbDy(WO$_4$)$_2$ lattice contains two macroscopically nonequivalent ions rotated by an angle of $\approx 45°$ (at four ions per unit cell) and the absence of a spontaneous moment in this compound, we can explain the experimental data on the field dependence of the magnetization by a planar four-sublattice noncollinear model (the alternative version, a two-sublattice model with canted sublattices, is contradicted by experiment, since in that case one should observe a nonzero spontaneous magnetic moment in one of the directions). The circumstance that the saturation magnetization is possibly the same in the y and z directions allows one to assume that the canting angle of the sublattices is close to $45°$, which is consistent with the EPR data.

Thus an analysis of the susceptibility and magnetization data makes it possible to determine that the magnetic structure of RbDy(WO$_4$)$_2$ is a noncollinear antiferromagnetic structure. The magnetic moments lie in the yz plane, deviated by $12°$ and rotated by an angle of around $45°$ to one of the principal magnetic axes y or z (Fig. 5). This conclusion does not agree with the conclusions of Ref. 12, where a collinear magnetic structure with the antiferromagnetic vector directed along the crystallographic axis b was proposed. However, such a structure disagrees with the magnetization experiment. We believe that there were two reasons for the

mistaken conclusion of Ref. 12: the chosen method of calculating the dipole sums[13] in principle ignored the noncollinearity of the moments, and the authors used parameters and estimates of the interactions for the structural phase above the final, lowest-temperature structural transition at 5 K, since the measurements were made only down to 4.2 K.

CONCLUSIONS

We have studied the magnetic properties of the $RbDy(WO_4)_2$ single crystal in the temperature range 0.5–300 K in magnetic fields up to 20 kOe. We determined the directions of the principal magnetic axes. We observed strong anisotropy of the magnetic properties due to the symmetry of the environment of the Dy^{3+} ion. We determined the Curie constants and the Curie–Weiss parameters for the low-temperature region (1–5 K); these indicate a magnetic phase transition and attest to the antiferromagnetic character of the interaction along all three magnetic axes.

At $T_N = 0.8$ K $RbDy(WO_4)_2$ undergoes a magnetic phase transition to an antiferromagnetic state. We have shown that there is an appreciable contribution from the dipole–dipole interaction.

In the magnetically ordered region the imposition of a magnetic field along the magnetic axes y and z induces orientational phase transitions, which are tentatively identified as metamagnetic. The fact that there is practically no magnetic moment along the x axis indicates that the moments lie in the yz plane.

In addition to the magnetic phase transition, structural phase transitions are observed at temperatures of 5, 8, and 50 K. Interestingly, above the observed structural phase transition at 50 K the exchange interaction along the y axis becomes ferromagnetic.

*E-mail: khatsko@ilt.kharkov.ua

[1] S. V. Borisov and R. F. Klevtsova, Kristallografiya **13**, 517 (1968) [Sov. Phys. Crystallogr. **13**, 420 (1968)].
[2] P. V. Klevtsov and R. F. Klevtsova, Zh. Strukt. Khim. **18**, 339 (1978).
[3] V. K. Trunov and V. K. Rybakov, Zh. Strukt. Khim. **19**, 636 (1974).
[4] E. N. Khats'ko, A. S. Chernyi, and A. I. Kaplienko, Fiz. Nizk. Temp. **19**, 1218 (1993) [Low Temp. Phys. **19**, 864 (1993)].
[5] M. T. Borowiec, V. P. Dyakonov, A. Jedrzejczak, V. I. Markovich, A. A. Pavlyuk, H. Szymczak, E. E. Zubov, and M. Zaleski, J. Low Temp. Phys. **110**, 1003 (1998).
[6] V. P. D'yakonov, V. I. Markovich, V. L. Kovarskiĭ, A. V. Markovich, M. Borowiec, A. Endzheĭchak (Jedrzejczak), and H. Szymczak, Fiz. Tverd. Tela (St. Petersburg) **40**, 2221 (1998) [Phys. Solid State **40**, 2017 (1998)].
[7] M. T. Borowiec, V. Dyakonov, V. Kamenev, A. Nabialek, A. Prokhorov, H. Szymczak, and M. Zaleski, Acta Phys. Pol. A **94**, 71 (1998).
[8] M. T. Borowiec, H. Szymczak, and M. Zaleski, Proc. SPIE **3724**, 292 (1999).
[9] M. T. Borowiec, Proc. SPIE **4412**, 196 (2001).
[10] E. Stryjewski and N. Giordano, Adv. Phys. **26**, 487 (1977).
[11] R. Carlin, *Magnetochemistry*, Springer, New York (1986), Mir, Moscow (1989).
[12] V. P. D'yakonov, É. E. Zubov, A. A. Pavlyuk, M. T. Borowiec, and H. Szymczak, Fiz. Tverd. Tela (St. Petersburg) **41**, 672 (1999) [Phys. Solid State **41**, 605 (1999)].
[13] T. H. Niemeyer, Physica (Amsterdam) **57**, 281 (1972).

Translated by Steve Torstveit

Phase diagram of a spin-1 non-Heisenberg antiferromagnet

Yu. A. Fridman,* Ph. N. Klevets, and D. V. Spirin

V. I. Vernadskii Tavricheskii National University, pr. Vernadskogo 4, 95007 Simferopol, Crimea, Ukraine
(Submitted April 2, 2003; revised June 19, 2003)

The phase transitions in temperature of an anisotropic antiferromagnet with a biquadratic exchange interaction are investigated. The conditions for realization of a quadrupolar phase in the study are determined, and the critical temperatures of the transition to the paramagnetic phase are found. The phase diagram are constructed for different relations among the material constants. © *2003 American Institute of Physics.* [DOI: 10.1063/1.1630718]

INTRODUCTION

The study of magnets with antiferromagnetic ordering has always attracted great interest from both theorists and experimentalists.[1–9] This is primarily because the technical implementation of the experimental studies on antiferromagnets is considerably simpler than for ferromagnets. As a rule, the Heisenberg model is used for describing antiferromagnetically ordered systems. However, there are a number of materials whose magnetic properties cannot be explained in the framework of that model. Such substances include, e.g., GdMg, EuS, and $CrBr_3$ (Refs. 10–13). In Refs. 10 and 12 it was conjectured that the magnetic properties of these compounds can be explained by taking the fourth-order (e.g., biquadratic) exchange interactions into account.

Interest in systems in which the influence of the biquadratic exchange interaction is substantial came up quite some time ago.[6–8] This interest arose, first, because non-Heisenberg ferromagnets can have a quadrupolar phase characterized by tensor order parameters. This is a clear example of the manifestation of the quantum properties of such systems. The non-Heisenberg character of the exchange interaction can be described by the following Hamiltonian:[7]

$$H = -\frac{1}{2}\sum_{n,m}[J\mathbf{S}_n\cdot\mathbf{S}_m + K(\mathbf{S}_n\cdot\mathbf{S}_m)^2], \qquad (1)$$

where J and K are the bilinear and biquadratic exchange constants, respectively.

Such a Hamiltonian permits description of a wider class of phenomena than the Heisenberg model. In particular, it has been shown[7–9] that ferromagnetic, antiferromagnetic, and quadrupolar phase states can form, depending on the relationship of the exchange constants in (1).

For a 3D ferromagnet, when $J > 0$ and $K > 0$, a ferromagnetic phase ($J > K$) and a quadrupolar phase ($K > J$) can exist. In a ferromagnet with a negative biquadratic interaction constant ($K < 0$) a ferromagnetic, quadrupolar, or quadrupolar–ferromagnetic phase can be realized.[7,14]

This raises the question of what phases can be realized in a non-Heisenberg antiferromagnet, i.e., when $J < 0$ and $K \neq 0$. The goal of this study is to examine this question in the framework of spin-wave theory.

The nature of the magnetism in two-dimensional systems is of fundamental interest, since it differs from the magnetism of three-dimensional systems. It is known that there is no long-range magnetic order at any finite temperature in an isotropic two-dimensional magnet.[15] The question of stabilization of long-range magnetic order in non-Heisenberg ferromagnets was studied in Refs. 16–18. However, as far as we know, the question of the stabilization of long-range magnetic order in a two-dimensional non-Heisenberg antiferromagnet has not been investigated. This question is the subject of the present study.

ANTIFERROMAGNET WITH "EASY PLANE" ANISOTROPY

Let us consider the question of the existence of a quadrupolar (Q) phase in an antiferromagnet with single-ion anisotropy (SA) of the "easy plane" type for the case $K > 0$. The antiferromagnet is two-sublattice, with equivalent sublattices, and the magnetic ion has spin $S = 1$. We choose the coordinate system such that the XOZ plane coincides with the basal plane of the system. The Hamiltonian of such a system can be written in the form

$$H = -\frac{1}{2}\sum_{n,m}[J\mathbf{S}_n\cdot\mathbf{S}_m + K(\mathbf{S}_n\cdot\mathbf{S}_m)^2] + \frac{\beta}{2}\sum_n (S_n^y)^2, \quad (2)$$

where $\beta > 0$ is the single-ion anisotropy constant. In Hamiltonian (2) each bond is counted twice, and the summation is over z nearest neighbors.

In the exchange part of Hamiltonian (2) we separate the mean field and the additional fields B_2^p ($p = 0,2$) due to the quadrupole moments; we then obtain the one-site Hamiltonian $H_0(n)$:

$$H_0(n) = -\bar{H}S_n^z - B_2^0 O_{2n}^0 - B_2^2 O_{2n}^2 + \frac{\beta}{2}(S_n^y)^2, \qquad (3)$$

where

$$\bar{H} = \left(J + \frac{K}{2}\right)\langle S_n^z\rangle; \quad B_2^0 = \frac{K}{6}q_2^0; \quad B_2^2 = \frac{K}{2}q_2^2;$$

$$O_{2n}^0 = 3(S_n^z)^2 - S(S+1); \quad O_{2n}^2 = \frac{1}{2}[(S_n^+)^2 + (S_n^-)^2];$$

$q_2^0 = \langle O_{2n}^0\rangle$, $q_2^2 = \langle O_{2n}^2\rangle$ are the quadrupolar order parameters. Here and below we use the notation $J = Jz$, $K = Kz$, where z is the number of nearest neighbors.

In separating the mean field and the additional quadrupole fields, we assume, as in Ref. 19, that in the first sublattice $S_n^x = 1/2(S_n^+ + S_n^-)$, $S_n^y = 1/2i\,(S_n^+ - S_n^-)$, S_n^z, and in the second sublattice one can make the following substitution: $S_m^x \to S_m^x$, $S_m^y \to -S_m^y$, $S_m^z \to -S_m^z$.

Solving the one-site problem with Hamiltonian (3), we determine the energy levels of the magnetic ion,

$$E_1 = \frac{\beta}{4} - B_2^0 - \chi, \quad E_0 = \frac{\beta}{2} + 2B_2^0, \quad E_{-1} = \frac{\beta}{4} - B_2^0 + \chi \tag{4}$$

and the eigenfunctions of the one-site Hamiltonian

$$\Psi(1) = \cos\varphi|1\rangle + \sin\varphi|-1\rangle, \quad \Psi(0) = |0\rangle,$$

$$\Psi(-1) = -\sin\varphi|1\rangle + \cos\varphi|-1\rangle, \tag{5}$$

where $\chi^2 = \bar{H}^2 + (\beta/4 + B_2^0)^2$, $|i\rangle$ are the eigenfunctions of the operator S^z ($i = 1, 0, -1$),

$$\cos\psi = \sqrt{\frac{\chi + \bar{H}}{2\chi}}, \quad \sin\varphi = \sqrt{\frac{\chi - \bar{H}}{2\chi}}.$$

Using the basis of eigenfunctions (5) of the magnetic ion, we construct the Hubbard operators $X_n^{MM'} = X_n^{\alpha(M'M)} \equiv |\Psi_n(M)\rangle\langle\Psi_n(M')|$ which describe the transition of the magnetic ion from the state M' to the state M. Here $\alpha(M'M)$ are the root vectors determined by the algebra of the Hubbard operators.[20] The spin operators are related to the Hubbard operators as

$$S_n^+ = \sqrt{2}[\cos\varphi(X_n^{10} + X_n^{0-1}) + \sin\varphi(X_n^{01} - X_n^{-10})],$$

$$S_n^z = \cos 2\varphi(X_n^{11} - X_n^{-1-1}) - \sin 2\varphi(X_n^{1-1} + X_n^{-11}),$$

$$S_n^- = (S_n^+)^+. \tag{6}$$

In studying the phase states of the system we use the method of bosonization of the Hubbard operators.[21] The basic idea of the method is to construct the Bose analog of Hamiltonian (2). The first step consists in the diagonalization of the one-site Hamiltonian and representation of the spin operators in terms of Hubbard operators. Then the Hubbard operators X_n^α are associated to pseudo-Hubbard operators $\tilde{X}_n^\alpha$, which are related to the Bose creation and annihilation operators as follows:[22,23]

$$\tilde{X}_n^{11} = 1 - a_n^+ a_n - b_n^+ b_n; \quad \tilde{X}_n^{00} = a_n^+ a_n;$$

$$\tilde{X}_n^{-1-1} = b_n^+ b_n; \quad \tilde{X}_n^{10} = (1 - a_n^+ a_n - b_n^+ b_n)a_n;$$

$$\tilde{X}_n^{01} = a_n^+; \quad \tilde{X}_n^{1-1} = (1 - a_n^+ a_n - b_n^+ b_n)b_n;$$

$$\tilde{X}_n^{-11} = b_n^+; \quad \tilde{X}_n^{0-1} = a_n^+ b_n; \quad \tilde{X}_n^{-10} = b_n^+ a_n. \tag{7}$$

Here the a's are Bose operators corresponding to the transition of an ion from state 1 to state 0 and vice versa, and the operators b correspond to the transition from state 1 to state -1 and vice versa.

As we have said, for a certain relationship of the material constants in (2) an antiferromagnetic or quadrupolar phase is realized in the system. From the expressions (6) relating the spin operators and Hubbard operators one can obtain equations for the order parameters for $T \to 0$:

$$\langle S_n^z \rangle \approx \cos 2\varphi, \quad q_2^0 \approx 1, \quad q_2^2 \approx \sin 2\varphi. \tag{8}$$

The system of equations (8) has two solutions: {1}. $\langle S_N^z \rangle = \sqrt{1 - (\beta/4J)^2}$, $q_2^0 = 1$, $q_2^2 = \beta/4J$, which corresponds to an antiferromagnetic phase; {2}. $\langle S^z \rangle = 0$, $q_2^0 = 1$, $q_2^2 = 1$, corresponding to a quadrupolar phase ($\beta \geq 4J$). As can be seen from the solutions of system (8), the realization of a Q phase in an antiferromagnet does not depend on the values of the biquadratic exchange interaction constants but is determined solely by the single-ion anisotropy constant and the bilinear exchange interaction constant. It is easy to see that $\langle S^z \rangle < 1$.

Let us assume that the relationship between the SA and Heisenberg exchange constants is such that an antiferromagnetic phase, corresponding to solution {1} is realized in the system. Using expressions (7), we rewrite (6) in terms of the Bose operators and write Hamiltonian (2) in the form

$$H^{(2)} = \sum_k (E_0 - E_1)a_k^+ a_k + \sum_k (E_{-1} - E_1)b_k^+ b_k$$

$$+ \frac{1}{2}\sum_k \left(J + \frac{K}{2}\right)\gamma_k(a_k^+ a_{-k}^+ + a_k a_{-k})$$

$$+ \frac{1}{4}\sum_k K\gamma_k(a_k^+ a_{-k}^+ + a_k a_{-k} - b_k^+ b_{-k}^+ - b_k b_{-k})$$

$$+ 2b_k^+ b_k), \tag{9}$$

where $\gamma_k = (\cos k_x + \cos k_y + \cos k_z)/3$ is the structure factor of a 3D antiferromagnet or $\gamma_k = (\cos k_x + \cos k_z)/2$ is the structure factor for a 2D system.

In Eq. (9) we have kept terms only to second-order in the creation and annihilation operators. Diagonalizing this Hamiltonian by means of a $u-v$ transformation, we get

$$H^{(2)} = \sum_k \varepsilon_\alpha(k)\alpha_k^+ \alpha_k + \sum_k \varepsilon_\beta(k)\beta_k^+ \beta_k, \tag{10}$$

where $\varepsilon_\alpha(k)$ and $\varepsilon_\beta(k)$ are, respectively, the spectra of the low-frequency and high-frequency magnons, which have the form

$$\varepsilon_\alpha(k)$$
$$= \sqrt{\left[\frac{\beta}{4} + (J+K)(1-\gamma_k)\right]\left[\frac{\beta}{4} + (J+K)(1+\gamma_k)\right]},$$

$$\varepsilon_\beta(k) = \sqrt{[2J + K(1-\gamma_k)][2J + K(1+\gamma_k)]}. \tag{11}$$

We now assume that the relation between the SA and exchange interaction constants is such that a quadrupolar phase is realized in the system, i.e., $\langle S_n^z \rangle = 0$, $q_2^0 = 1$, $q_2^2 = 1$; in that case a degeneracy of the excited energy levels occurs ($E_0 = E_{-1}$). In this phase the Hamiltonian (2), written in terms of the magnon creation and annihilation operators, has the form

$$H^{(2)} = \sum_k (E_0 - E_1) a_k^+ a_k + \sum_k (E_{-1} - E_1) b_k^+ b_k$$

$$+ \frac{1}{2} \sum_k \left(J + \frac{K}{2} \right) \gamma_k (a_k^+ a_{-k}^+ + a_k a_{-k} + 2 a_k^+ a_k$$

$$+ b_k^+ b_{-k}^+ + b_k b_{-k} + 2 b_k^+ b_k) + \frac{1}{4} \sum_k K \gamma_k (a_k^+ a_{-k}^+$$

$$+ a_k a_{-k} - 2 a_k^+ a_k + b_k^+ b_{-k}^+ + b_k b_{-k} - 2 b_k^+ b_k).$$
$$(12)$$

Diagonalizing Hamiltonian (12) by a $u-v$ transformation, we obtain the magnon spectra in the Q phase. Here we must take into account that the energy levels of the magnetic ion are degenerate in the Q phase. Because of this, the spectra of the a and b magnons are the same:

$$\varepsilon_\alpha(k) = \varepsilon_\beta(k)$$

$$= \sqrt{\left[\frac{\beta}{2} + K(1 - \gamma_k) \right] \left[\frac{\beta}{2} + K(1 + \gamma_k) + 2J\gamma_k \right]}.$$
$$(13)$$

As was shown in Refs. 7, 9, and 24, in an isotropic non-Heisenberg ferromagnet a Q phase can be realized for $|J| < |K|$. Analysis of expression (13) shows that the existence of a Q phase is also possible in an anisotropic non-Heisenberg antiferromagnet for $\beta \geqslant 4J$.

However, it was shown in Ref. 9 that if the exchange interaction constants are related as $J = -J \cos \theta$, $K = -J \sin \theta$, $\theta \in [-\pi/2; 0]$, then the Q phase is not realized in an isotropic non-Heisenberg antiferromagnet.

Let us consider an isotropic non-Heisenberg antiferromagnet described by Hamiltonian (1), assuming that $J < 0$ and $K > 0$. In this case we do not impose such rigid restrictions on the exchange interaction constants as in Ref. 9.

In this case the system of equations (8) has two solutions: {1}. $\langle S_n^z \rangle = 1$, $q_2^0 = 1$, $q_2^2 = 0$, which corresponds to an antiferromagnetic phase; {2}. $\langle S^z \rangle = 0$, $q_2^0 = 1$, $q_2^2 = 1$, which corresponds to a Q phase.

Let us assume that the system is found in the antiferromagnetic phase. The spectra of the low- and high-frequency magnons in this case are written in the form

$$\varepsilon_\alpha(k) = (J + K) \sqrt{1 - \gamma_k^2},$$

$$\varepsilon_\beta(k) = \sqrt{(2J + K)^2 - K^2 \gamma_k^2}.$$
$$(14)$$

We consider the solution corresponding to the Q phase. The magnon spectra obtained from Eq. (13) for $\beta = 0$ have the form

$$\varepsilon_\alpha(k) = \varepsilon_\beta(k) = \sqrt{K(1 - \gamma_k)[K(1 + \gamma_k) + 2J\gamma_k]}.$$
$$(15)$$

Spectrum (15) becomes nonphysical (imaginary) if $\gamma_k < -K/(2J + K)$. This indicates the impossibility of realizing a quadrupolar phase in an isotropic non-Heisenberg antiferromagnet and confirms the numerical results of Ref. 9, since the magnon dispersion relation (15) does not hold for arbitrary values of the wave vector **k**. This allows us to state that the Q phase does not exist in an isotropic non-Heisenberg antiferromagnet for any relationship of the exchange constants.

PHASE TRANSITIONS IN TEMPERATURE

To determine the temperature T_N of the transition from the antiferromagnetic to the paramagnetic phase, we consider the order parameter $\langle S_n^z \rangle$:

$$\langle S_n^z \rangle = \frac{1}{N} \sum_n \langle 1 - a_n^+ a_n \rangle. \tag{16}$$

Expression (16) can be rewritten as

$$\langle S_n^z \rangle = 1 - \frac{1}{(2\pi)^d} \int_{-\pi}^{\pi} \frac{(u_k^2 + v_k^2) d^d k}{\exp\left(\dfrac{\varepsilon_\alpha(k)}{T} \right) - 1} - S(0), \tag{17}$$

where d is the dimensionality of the system; u_k and v_k are the parameters of the Bogolyubov transformation, $u_k^2 + v_k^2 = (E_0 - E_1)/\varepsilon_\alpha(k)$; $S(0)$ are the zero-point vibrations, which are determined by the expression

$$S(0) = \frac{1}{(2\pi)^d} \int_{-\pi}^{\pi} v_k^2 d^d k. \tag{18}$$

In the case of an isotropic antiferromagnet the zero-point vibrations are independent of the value of the exchange interactions, and $S(0) = 0.078$. In the case of a 2D anisotropic antiferromagnet the zero-point vibrations are dependent on the value of the exchange interaction (a change in K from 0 to $1.5J$ will cause the value of $S(0)$ to increase from 0.167 to 0.177). In a 3D antiferromagnet the zero-point vibrations are almost a factor of 2 smaller than in a 2D antiferromagnet (a change in K from 0 to 1.5 will cause the value of $S(0)$ to increase from 0.075 to 0.077).

The antiferromagnetic–paramagnetic phase diagrams of the two-dimensional and three-dimensional anisotropic antiferromagnets in the variables $K-T$ are presented in Fig. 1.

To determine the temperature T_Q of the transition in an anisotropic antiferromagnet from the quadrupolar to the paramagnetic phase, we consider the order parameter q_2^2:

$$q_2^2 = \frac{1}{N} \sum_n \langle 1 - 3 a_n^+ a_n \rangle. \tag{19}$$

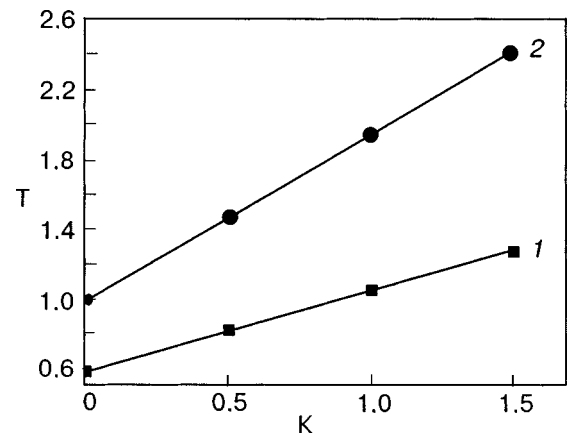FIG. 1. Antiferromagnetic-paramagnetic phase diagram of an anisotropic non-Heisenberg antiferromagnet in the variables $K-T$ (K is the biquadratic exchange constant and T is the temperature (in units of J) ($\beta/J = 0.02$): *1*—the line of the antiferromagnetic-paramagnetic phase transition for a 2D system; *2*—the line of the antiferromagnetic-paramagnetic phase transition for a 3D system.
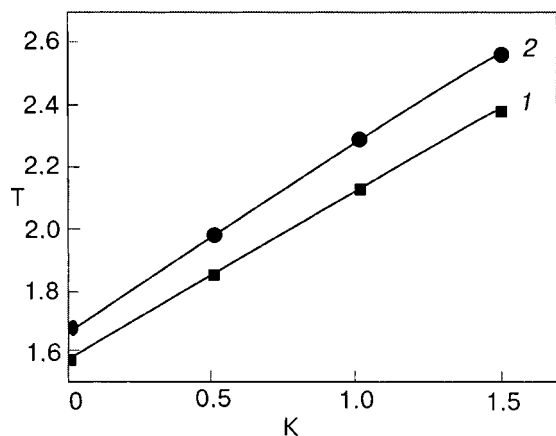
FIG. 2. Quadrupolar-paramagnetic phase diagram of an anisotropic non-Heisenberg antiferromagnet in the variables $K-T$ (K is the biquadratic exchange constant and T is the temperature (in units of J) ($\beta/J=5$): *1*—the line of the quadrupolar-paramagnetic phase transition for a 2D system; *2*—the line of the quadrupolar-paramagnetic phase transition for a 3D system.

In Eq. (19) we have taken into account that $\langle a_n^+ a_n \rangle = \langle b_n^+ b_n \rangle$ in the Q phase because of the degeneracy of the energy levels ($E_0 = E_{-1}$).

Expression (19) can be rewritten as

$$q_2^2 = 1 - \frac{3}{(2\pi)^d} \int_{-\pi}^{\pi} \frac{(u_k^2 + v_k^2) d^d k}{\exp\left(\dfrac{\varepsilon_\alpha(k)}{T}\right) - 1} - q(0), \qquad (20)$$

where

$$q(0) = \frac{1}{(2\pi)^d} \int_{-\pi}^{\pi} v_k^2 d^d k$$

are the zero-point vibrations in the Q phase.

The zero-point vibrations in the Q phase are smaller than in the antiferromagnetic phase: for a 2D system a change in K from 0 to 1.5J will increase the value of $q(0)$ from 0.016 to 0.037; for a 3D system the zero-point vibrations, as in the antiferromagnetic phase, are almost a factor of 2 smaller than in the 2D case; increasing K from 0 to 1.5J increases $q(0)$ from 0.009 to 0.022.

The quadrupolar–paramagnetic phase diagrams of 2D and 3D anisotropic antiferromagnets in the variables $K-T$ are shown in Fig. 2.

CONCLUSION

The goal of this study was to explore the possibility of realization of a quadrupolar phase in a non-Heisenberg antiferromagnet with spin 1. The studies showed that in an anisotropic non-Heisenberg antiferromagnet with "easy plane" anisotropy the appearance of a quadrupolar phase is possible for $\beta \geq 4J$, independently of the value of the biquadratic exchange interaction. In isotropic 2D and 3D non-Heisenberg antiferromagnets the quadrupolar phase is not realized under any conditions. Analogous results were obtained by a numerical simulation in Ref. 9. It should be noted, however, that in the present study the value of the exchange interaction constant was not so rigidly restricted as in Ref. 9.

Using expressions (17) and (20), we constructed phase diagrams of 2D and 3D anisotropic non-Heisenberg antiferromagnets for different values of the biquadratic exchange interaction constant. In comparing the phase diagrams of the 2D and 3D antiferromagnets (Fig. 1), one notices that the temperature of the transition from the antiferromagnetic to the paramagnetic phase for a 2D antiferromagnet is almost a factor of 2 lower than for the 3D system. This is due to the fact that fluctuations in the 3D systems are significantly smaller than in 2D systems, and that affects the value of the Néel temperature. The temperature of the transition from the quadrupolar to the paramagnetic phase (see Fig. 2) is practically the same for 2D and 3D antiferromagnets. Such a weak dependence of the transition temperature on the dimensionality of the system can be explained, we believe, by the circumstance that the quadrupolar phase is "less ordered" than the antiferromagnetic phase. This "disorder" is due to the fact that the magnetizations of the sublattices equal zero and to the specific structure of the ground-state wave functions, which in the quadrupolar phase are a superposition of the states $|1\rangle$ and $|-1\rangle$ of the operator S^z (see expression (5), with $\cos\varphi = \sin\varphi = 1/\sqrt{2}$). The small difference in the phase diagrams in the quadrupolar phase is due to the fact that the zero-point vibrations are larger for 2D systems than for 3D systems.

Thus the dimensionality of the system has a substantial influence on the temperature of the transition to the paramagnetic phase only in the antiferromagnetic phase.

The phase diagram of a 3D isotropic non-Heisenberg antiferromagnet in the antiferromagnetic phase is similar to that of a 3D anisotropic non-Heisenberg antiferromagnet. The small differences in the phase transition temperatures are due to the differences in the zero-point vibrations and the value of the single-ion anisotropy.

[*]E-mail: frid@tnu.crimea.ua

[1] P. W. Anderson, Phys. Rev. **79**, 350 (1950).
[2] P. W. Anderson, Phys. Rev. **86**, 694 (1952).
[3] F. Burr Anderson and Herbert B. Callen, Phys. Rev. **136**, 1068 (1964).
[4] F. D. M. Haldane, Phys. Rev. B **25**, 4925 (1982).
[5] E. V. Kuz'min, Fiz. Tverd. Tela (St. Petersburg) **44**, 1075 (2002) [Phys. Solid State **44**, 1122 (2002)].
[6] Nai Li Huang and R. Orbach, Phys. Rev. Lett. **12**, 275 (1964).
[7] H. H. Chen and Peter M. Levy, Phys. Rev. B **7**, 4267 (1973).
[8] V. M. Matveev, Zh. Éksp. Teor. Fiz. **65**, 1626 (1973) [Sov. Phys. JETP **38**, 813 (1974)].
[9] Kenji Harada and Naoki Kawashima, Phys. Rev. B **65**, 524031 (2002).
[10] E. A. Harris and R. Owen, Phys. Rev. Lett. **11**, 9 (1963).
[11] T. Kawae, M. Shimogai, M. Mito, K. Takeda, H. Ishii, and T. Kitai, Phys. Rev. B **65**, 124091 (2001).
[12] U. Kobler, R. Mueller, L. Smardz, D. Maier, K. Fischer, B. Olefs, and W. Zinn, Z. Phys. B: Condens. Matter **100**, 497 (1996).
[13] U. Kobler, R. M. Mueller, W. Schnelle, and K. Fischer, J. Magn. Magn. Mater. **188**, 333 (1998).

[14] Yu. A. Fridman, O. V. Kozhemyako, and B. L. Eingorn, Fiz. Nizk. Temp. **27**, 495 (2001) [Low Temp. Phys. **27**, 362 (2001)].

[15] N. Mermin and H. Wagner, Phys. Rev. Lett. **17**, 1133 (1966).

[16] S. V. Maleev, Zh. Éksp. Teor. Fiz. **70**, 2344 (1976) [Sov. Phys. JETP **43**, 1240 (1976)].

[17] B. A. Ivanov and E. V. Tartakovskaya, Fiz. Nizk. Temp. **24**, 1095 (1998) [Low Temp. Phys. **24**, 823 (1998)].

[18] A. Kashuba, Phys. Rev. Lett. **73**, 2264 (1994).

[19] Qing Jiang, Hai-Xia Cao, and Zhen-Ya Li, Phys. Status Solidi B **229**, 1233 (2002).

[20] R. O. Zaĭtsev, Zh. Éksp. Teor. Fiz. **68**, 207 (1975) [Sov. Phys. JETP **41**, 100 (1975)].

[21] V. V. Val'kov and T. A. Val'kova, Preprint No. 667F [in Russian], Krasnoyarsk, Russia (1990).

[22] Yu. A. Fridman and D. V. Spirin, J. Magn. Magn. Mater. **253**, 111 (2002).

[23] Yu. A. Fridman and D. V. Spirin, Phys. Status Solidi B **231**, 165 (2002).

[24] É. L. Nagaev, *Magnets with a Complex Exchange Interaction* [in Russian], Nauka, Moscow (1988).

Translated by Steve Torstveit

ELECTRONIC PROPERTIES OF METALS AND ALLOYS

High-temperature quantum size oscillations of the conductivity in thin metal films

I. V. Kozlov*

B. Verkin Institute for Low Temperature Physics and Engineering, National Academy of Sciences of Ukraine, pr. Lenina 47, 61103 Kharkov, Ukraine

The longitudinal electrical conductivity of a thin conducting film in the presence of electron and hole groups of charge carriers is calculated by the Kubo method under conditions such that the carrier motion is spatially quantized. It is shown that in the case of elastic scattering on impurities there are quantum high-temperature oscillations of the conductivity which are relatively insensitive to the temperature smearing of the Fermi level. © *2003 American Institute of Physics.* [DOI: 10.1063/1.1630719]

1. INTRODUCTION

The quantum size effect (QSE) in thin films has been well studied both experimentally and theoretically (see Ref. 1 and the literature cited therein). In spite of this, several experimentally observed phenomena have not been given an exhaustive theoretical explanation. For example, experimental studies of the QSE in bismuth[2–5] find evidence of the presence of quantum size oscillations of the conductivity at $T \gg \Delta E$ (ΔE is the distance between adjacent subbands formed by the size quantization, and T is the temperature in energy units), while at the same time the theoretical calculation (see Refs. 6 and 7) predicts that they should be strongly attenuated. Interestingly, a similar situation also arises in the case of magnetic quantization, as is attested to by a series of experimental studies of the Shubnikov–de Haas (SdH) effect in bismuth (see Refs. 8–10 and references cited therein). These high-temperature oscillations cannot be explained in the framework of the usual theory of the SdH effect (see, e.g., Ref. 11).

In this paper we consider a mechanism for the appearance of quantum high-temperature oscillations (QHTOs) in the presence of an elastic scattering potential. This mechanism, which was proposed in Ref. 12 for semiconductors placed in a quantizing magnetic field, consists in the following. In the case of two valleys, the electron density of states has a feature at values of the energy corresponding to the bottom of a subband (i.e., the point of the subband with the lowest value of the energy for the electron valley and the highest energy for the hole valley). The intensity of intervalley scattering increases substantially when the energies corresponding to the bottom of any two subbands in the different valleys coincide. This condition of a maximum in the scattering intensity will be sensitive to changes in the position of the subbands. As the quantization conditions are varied (i.e., the magnetic field strength in the case of quantization by a magnetic field or the thickness of the sample in the case of the QSE) the subbands from the different valleys will shift along the energy scale with different rates, periodically "overtaking" one another. In the case of valleys with differ-

ent signs of the charge carriers the subbands will be shifted in opposite directions. Of course, this condition must hold in the region of temperature smearing of the Fermi level.

This mechanism is also used to explain the high-temperature oscillations in bismuth in a quantizing magnetic field (the case of two valleys with different signs of the charge carrier was studied in Refs. 13–15) and in the case of a quasi-two-dimensional dispersion relation.[16,17]

2. STATEMENT OF THE PROBLEM

We consider a thin metal film with mirrorlike boundaries, $z = 0$ and $z = L_z$, and two groups of charge carriers: electron and hole. For simplicity we shall assume that the Fermi surface consists of two pockets with a quadratic dispersion relation in each, i.e., the energy ε of the charge carriers in the electron ε_e and hole ε_h valleys is equal:

$$\varepsilon_e = \frac{p_x^2 + p_y^2}{2m_e} + \alpha_e n^2,$$

$$\varepsilon_h = \varepsilon_{OL} - \frac{p_x^2 + p_y^2}{2m_h} - \alpha_h n^2, \tag{1}$$

where $m_{e,h}$ are the masses of the electrons and holes, respectively, ε_{OL} is the value of the band overlap, and

$$\alpha_{e,h} = \frac{\pi^2 \hbar^2}{2m_{e,h} L_z^2}.$$

We shall take into account only the scattering on a short-range impurity, the effective radius of which is much smaller than the de Broglie wavelength of an electron on the Fermi surface, and assume that the impurity centers are uniformly distributed over the volume of the film with a density n_{imp}. For simplicity we shall assume that the matrix elements of the impurity potential operator responsible for transitions within the electron and hole groups and for intervalley transitions are of the same order of magnitude, i.e.,

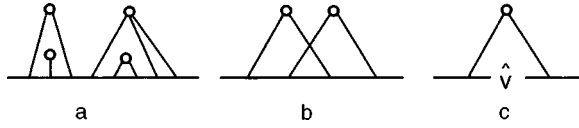$$\hat{V}_{ee} \simeq \hat{V}_{hh} \simeq \hat{V}_{eh}. \tag{2}$$

FIG. 1. Examples of the diagrams taken into account in the averaging over the distribution of impurity centers (a); a "crossing" diagram (b); a diagram in which the velocity operator leads to vanishing of the corresponding contribution after averaging over the position of the impurity center (c).

A severalfold difference in the values of these quantities will not qualitatively influence the result but will only affect the amplitude ratio of the various modes of oscillation while preserving the qualitative picture of the QSE.

3. CONDUCTIVITY AT ZERO TEMPERATURE

We write the expression for the conductivity in the form[18]

$$\sigma_{xx} = \frac{2\pi\hbar}{T} e^2 \int_{-\infty}^{\infty} dE f^0(E)(1 - f^0(E))$$

$$\times \langle \mathrm{Tr}\, \hat{v}_x \delta(\hat{H} - E) \hat{v}_x \delta(\hat{H} - E)\rangle_{\mathrm{imp}}, \tag{3}$$

where $f^0(E)$ is the Fermi–Dirac distribution function, $\hat{H} = \hat{\varepsilon} + \Sigma_i V(\hat{\mathbf{r}} - \mathbf{R}_i)$ is the energy operator with the impurity taken into account (the impurity contribution to the energy operator is equal to the sum of the potentials of the individual impurity centers, which are randomly distributed at the points $\mathbf{R}_i$), the summation in the trace Tr is done over the one-electron complete quantum set (n, P_x, P_y), and the angle brackets denote averaging over the distribution of impurity centers.

In averaging over the distribution of impurity centers we use the standard diagram technique, given, e.g., in Ref. 19 or in more detail for the case of an elastic impurity in Ref. 20. Simple estimates show that in expression (3) the contributions containing "crossing" diagrams (see Fig. 1b) can be neglected.[20] The contribution of expressions of the form in Fig. 1c, which contain the velocity operator between the impurity potential operators generated by the same impurity center, also turn out to be negligible (the contribution can be neglected after averaging the expression over the impurity coordinate). This makes it possible to replace the average of the product of delta functions over the distribution of impurity centers in expression (3) by the product of the averages:

$$\langle \hat{v}_i \delta(\hat{H} - E) \hat{v}_j \delta(\hat{H} - E)\rangle_{\mathrm{imp}}$$

$$= \hat{v}_i \langle \delta(\hat{H} - E)\rangle_{\mathrm{imp}} \hat{v}_j \langle \delta(\hat{H} - E)\rangle_{\mathrm{imp}}.$$

The latter can be represented in the form $\langle \delta(\hat{H} - E)\rangle_{\mathrm{imp}} = i/2\pi (\hat{G}_V^+(E) - \hat{G}_V^-(E))$, where

$$\hat{G}_V^{\pm}(E) = \left\langle \frac{1}{E - \hat{H} \pm i\delta} \right\rangle_{\mathrm{imp}} = \frac{1}{E - \hat{\varepsilon} - \hat{\Sigma}^{\pm}(E)} \tag{4}$$

is the total Green's function, the quantity $\hat{\Sigma}(E) = \langle \hat{\Sigma}_R(E)\rangle_{\mathrm{imp}}$ by definition (see Refs. 19 and 20) is the self-energy part averaged over the impurity distribution,

$$\hat{\Sigma}_R^{\pm}(E) = \hat{V}_R + \hat{V}_R \hat{G}_V^{\pm}(E) \hat{V}_R + \dots, \tag{5}$$

$\hat{V}_R$ is the potential operator of an individual impurity center at the point $\mathbf{R}$, and

$$\hat{G}^{\pm}(E) = \frac{1}{E - \hat{\varepsilon} \pm i\delta} \tag{6}$$

is the Green's function without the impurity taken into account.

In evaluating the series (5) we can use the analogy with the expression for the $\hat{T}^{\pm}$ operator:

$$\hat{T}_R^{\pm}(E) = \hat{V}_R + \hat{V}_R \hat{G}^{\pm}(E) \hat{V}_R + \dots . \tag{7}$$

It follows from the explicit form of the Green's function (4), (6) that the relation $\hat{G}_V^{\pm}(E) = \hat{G}^{\pm}(E - \hat{\Sigma}^{\pm}(E))$. Then $\hat{\Sigma}_R^{\pm}(E)$ can be expressed through the equation

$$\hat{\Sigma}_R^{\pm}(E) = \hat{T}_R^{\pm}(E - \Sigma^{\pm}(E)). \tag{8}$$

In solving equation (8) we can assume that the operator $\hat{\Sigma}^{\pm}(E)$ is diagonal: $\hat{\Sigma}^{\pm}(E) = \Sigma^{\pm}(E)\hat{I}$, where $\hat{I}$ is the unit operator.

For the operator $\hat{T}^{\pm}(E)$ the expression proposed in Ref. 21 is valid (with a correction for the form of the spectrum (1)):

$$T_{\nu\mu}^{\pm}(E) = t^{\pm}(E) \varphi_\nu^*(\mathbf{R}) \varphi_\mu(\mathbf{R}), \tag{9}$$

$$t^{\pm}(E, \mathbf{R}) = \frac{S}{1 - SG_q^{\pm}(E, Z)},$$

where $\mathbf{R} = (X, Y, Z)$ is the coordinate of the impurity center,

$$\varphi_\nu(\mathbf{r}) = \frac{1}{2\pi\hbar} \sqrt{\frac{2}{L_z}} e^{\frac{i}{\hbar}P_x x} e^{\frac{i}{\hbar}P_y y} \sin\left(\frac{\pi n z}{L_z}\right),$$

$$\nu = (n, P_x, P_y), \tag{10}$$

is the eigenfunction of the unperturbed energy operator $\hat{\varepsilon}$,

$$S = \int V(\mathbf{r}) \psi_0(\mathbf{r}) d^3\mathbf{r} \tag{11}$$

is the renormalized strength of the impurity (see Refs. 16 and 21), $\psi_0(\mathbf{r})$ is determined by Dyson's equation

$$\psi_0(\mathbf{r}) = 1 + \int G_{\mathrm{cl}}(\mathbf{r}, \mathbf{r}') V(\mathbf{r}') \psi_0(\mathbf{r}') d^3\mathbf{r}',$$

$V(\mathbf{r})$ is the impurity potential, and $G_q^{\pm}(E, Z)$ is the Green's function after subtraction of the singular contribution $G_{\mathrm{cl}}(\mathbf{r}, \mathbf{r}') \sim 1/|\mathbf{r} - \mathbf{r}'|$ and is given by the following relation in the coordinate representation:

$$G^{\pm}(E; \mathbf{r}, \mathbf{r}') = \sum_\nu \frac{\varphi_\nu(\mathbf{r}) \varphi_\nu^*(\mathbf{r}')}{E - \varepsilon_\nu \pm i\delta}$$

$$= G_{\mathrm{cl}}(\mathbf{r} - \mathbf{r}') + G_q^{\pm}(E, Z) \tag{12}$$

($G_{\mathrm{cl}}(\mathbf{r}, \mathbf{r}')$ is equal to the real part of the Green's function $G^{\pm}(E; \mathbf{r}, \mathbf{r}')$ (6) without the quantization taken into account, and $L_z \to \infty$; Ref. 21). In the case under consideration, that of a short-range impurity, the dependence of $G_q^{\pm}(E; \mathbf{r}, \mathbf{r}')$ on $|\mathbf{r} - \mathbf{r}'|$ can be neglected, but in contrast to the case of magnetic quantization considered in Ref. 21, there is dependence on the z component of the coordinate $\mathbf{r} = \mathbf{r}'$.

It follows from the definition of the Green's function that

$$G_q^\pm(E,z) = G_e^\pm(E,z) + G_h^\pm(E,z), \tag{13}$$

where the subscripts e and h indicate whether the summation in (12) is done only over the electron valley or only over the hole valley. Taking into account the explicit form of the energy spectrum (1) and the definition of the Green's function, we can write $G_h^\pm(E,z) = -G_e^\mp(\varepsilon_{OL} - E, z)|_{e \to h}$. After substituting $\varphi_\nu(\mathbf{r})$ in the explicit form (10) into expression (12) and using Poisson's formula [the divergent contribution of the zeroth harmonic is renormalized by $G_{cl}(\mathbf{r} - \mathbf{r}')$], we obtain

$$G_e^\pm(E,z) = \mp \frac{2\pi^2 i m_e}{L_z (2\pi\hbar)^2} \sqrt{\frac{E}{\alpha_e}} \left[1 \mp 2\sum_{k=1}^\infty \frac{i}{\sqrt{E}\beta_0^e} e^{\pm i\beta_0^e \sqrt{E}} \right.$$

$$\left. \pm \sum_{k=-\infty}^\infty \frac{i}{\sqrt{E}|\beta_z^e|} e^{\pm i|\beta_z^e|\sqrt{E}} \right], \tag{14}$$

where $\beta_0^{e,h} = 2\pi k/\sqrt{\alpha_{e,h}}$, $\beta_z^{e,h} = (2\pi/\sqrt{\alpha_{e,h}})(k + z/L_z)$.

In making the transition to $\Sigma^\pm(E)$ we must perform the average of $\hat{T}_R^\pm(E)$ over the Z coordinate of the impurity center. The series in formula (14) contains a singularity with respect to z, and therefore in the expansion in the small parameter $1/n_F \sim \sqrt{\alpha_e/\varepsilon_F}$, $\sqrt{\alpha_h/(\varepsilon_{OL} - \varepsilon_F)} \ll 1$ (n_F is the index of the highest-numbered subband that overlaps the Fermi surface) it is more convenient to leave the singular part in the denominator of expression (9). The off-diagonal matrix elements of the operator $T_{\mu\nu}^\pm(E)$ after averaging over Z are smaller by a factor of $1/n_F$ than the diagonal ones for both the monotonic part and oscillatory part, and they can be neglected. In solving Eq. (8) it is sufficient to use the approximation $\hat{\Sigma}_R^\pm(E) \approx \hat{T}_R^\pm(E - \Sigma_{cl}^\pm)$, where $\Sigma_{cl}^\pm$ is the nonquantum, monotonic part of $\Sigma^\pm(E)$, since the last terms of the expansion are small in the parameter $\hbar/\tau\varepsilon_F$, $\hbar/\tau(\varepsilon_{OL} - \varepsilon_F) \ll 1$. In the equation for the conductivity, $\mathrm{Re}\,\Sigma_{cl}$ can be taken into account by a simple renormalization of ε_F:

$$\varepsilon_F \Rightarrow \tilde{\varepsilon}_F = \varepsilon_F - \mathrm{Re}\,\Sigma^\pm(\tilde{\varepsilon}_F) \tag{15}$$

(as is shown in Refs. 20 and 22). From here on, ε_F will be understood to mean the latter, renormalized quantity. The $\mathrm{Im}\,\Sigma_{cl}^\pm$ in the argument of the T matrix leads to the Dingle factor.

Let us consider expression (3) for $T = 0$ with allowance for the renormalization (15) of ε_F. After some transformations the impurity potential will appear in expression (3) only in the combination

$$\frac{1}{\tau(E)} = \frac{i}{\hbar}[\Sigma^+(E) - \Sigma^-(E)], \tag{16}$$

which plays the role of the relaxation time (in the framework of the approximations made, this is the same as the method of the quantum kinetic equation[22]).

Conductivity oscillations not due to scattering on impurities (i.e., oscillations that survive when $\tau(E)$ is replaced by a constant in the expression for the conductivity) which arise in evaluating the trace Tr in formula (3), have the same frequency as in (16) but a substantially smaller amplitude, which, after calculation of (3) is smaller in order of magnitude by a factor of $1/n_F^2$ than the monotonic part of the conductivity, and they can be neglected. The reason for their

smallness is that the velocity operator $\hat{v}_x$ appears under the Tr sign in expression (3), and its eigenvalues are close to zero in the vicinity of the points $\mathbf{p} = (0, 0, \pm p_F)$ which determine the oscillation frequency. Therefore expression (3) can be replaced by its classical analog, the quantization being taken into account only in the evaluation of expression (16). At $T = 0$ the conductivity will be proportional to the relaxation time:

$$\sigma_{xx} \sim \tau(\varepsilon_F). \tag{17}$$

To make the resulting expression for the conductivity less awkward, we shall restrict discussion to the limiting case of a weak impurity with a scattering amplitude much less than the de Broglie wavelength at the Fermi level. Then

$$\frac{1}{\tau(E)} = \frac{1}{\tau_0}\left(1 + \sum_{k=1}^\infty R_k^e(E) + \sum_{k=1}^\infty R_k^h(E) \right), \tag{18}$$

where

$$R_k^e(E) = \frac{1}{2\pi k}\sqrt{\frac{\alpha_e}{E}}\exp\left(-\frac{\pi k\hbar}{2\tau_0\sqrt{\alpha_e E}} \right)\sin\left(2\pi k\sqrt{\frac{E}{\alpha_e}} \right), \tag{19}$$

$$R_k^h(E) = \frac{1}{2\pi k}\sqrt{\frac{\alpha_h}{\varepsilon_{OL} - E}}$$

$$\times \exp\left(-\frac{\pi k\hbar}{2\tau_0\sqrt{\alpha_h(\varepsilon_{OL} - E)}} \right)\sin\left(2\pi k\sqrt{\frac{\varepsilon_{OL} - E}{\alpha_h}} \right).$$

It follows from the assumptions made earlier that $\sum_{k=1}^\infty R_k^{e,h} \sim 1/n_F \ll 1$, i.e., the oscillatory part of the relaxation time is much smaller than the classical part τ_0. Thus the expression for the conductivity can be written in the form

$$\sigma_{xx} = \sigma^{cl}\left(1 + \sum_{k=1}^\infty R_k^e(\varepsilon_F) + \sum_{k=1}^\infty R_k^h(\varepsilon_F) \right)^{-1}$$

$$\approx \sigma^{cl}\left(1 - \sum_{k=1}^\infty R_k^e(\varepsilon_F) - \sum_{k=1}^\infty R_k^h(\varepsilon_F) \right.$$

$$\left. + 2\sum_{k,l=1}^\infty R_k^e(\varepsilon_F) R_l^h(\varepsilon_F) \right), \tag{20}$$

where in the terms of second-order smallness in $1/n_F$ we have kept only the contributions responsible for the QHTOs; σ^{cl} is the classical part of the conductivity σ_{xx}.

4. CONDUCTIVITY AT FINITE TEMPERATURE

The Fermi–Dirac distribution function appears in expression (3) for the conductivity only in the combination

$$\frac{1}{T}f^0(E)(1 - f^0(E)) = -\frac{\partial f^0(E)}{\partial E}.$$

Thus we can write

$$\sigma_{xx} = \int \left(-\frac{\partial f^0(E)}{\partial E} \right) F(E)\,dE, \tag{21}$$

where $F(E)$ is a function of E that is independent of T. At $T = 0$

$$\sigma_{xx}|_{T=0} = F(\varepsilon_F), \tag{22}$$

which makes it possible to obtain the explicit form of $F(E)$ from the dependence of the conductivity on ε_F (20). After that it remains only to substitute it into expression (21), the evaluation of which will give the temperature dependence of the conductivity. The derivation given here is analogous to the calculation of the temperature dependence of the thermodynamic potential Ω in Ref. 11.

The nonclassical part of the conductivity at $T=0$ in formula (20) behaves as an oscillatory function of ε_F. At a certain value $\varepsilon_F = E_{k,l}$

$$E_{k,l} = \varepsilon_{OL} \frac{\alpha_h k^2}{\alpha_h k^2 + \alpha_e l^2},\qquad(23)$$

the condition $k\Delta E_h^F = l\Delta E_e^F$ is satisfied, where k and l are integers. Here

$$\Delta E_e^F = 2\sqrt{\varepsilon_F \alpha_e},\quad \Delta E_h^F = 2\sqrt{(\varepsilon_{OL} - \varepsilon_F)\alpha_h}\qquad(24)$$

is the distance between adjacent subbands with positions close to the Fermi level in the electron and hole valleys, respectively. That is, at $\varepsilon_F = E_{k,l}$ the frequency of the conductivity oscillations (for one of the harmonics) as a function of ε_F goes to zero, which leads to a softer than exponential temperature dependence. In the calculation of the temperature dependence of the conductivity we shall distinguish two limiting cases: the energy level $E_{k,l}$ lies far outside the limits of the temperature smearing of the Fermi level, making it possible to neglect the unequal spacing of the energy spectrum, and the opposite limiting case with $|E_{k,l} - \varepsilon_F| \ll T$, when the unequal spacing determines the region of energy values that gives the main contribution to the integral (21). Substituting the expression (20) for the conductivity into the integral (21), we obtain

$$\sigma_{xx} = \sigma^{\mathrm{cl}} + \sigma^h + \sigma^e + \sum_{k,l=1}^{\infty}(\sigma_{k,l}^- + \sigma_{k,l}^+),\qquad(25)$$

where σ^{cl} is the monotonic part of the conductivity,

$$\sigma^e = -\sigma_{xx}^{\mathrm{cl}} \sum_{k=1}^{\infty} \frac{1}{2\pi k}\sqrt{\frac{\alpha_e}{\varepsilon_F}}\,\Psi\!\left(\frac{2\pi^2 kT}{\Delta E_e^F}\right)$$

$$\times \exp\!\left(-\frac{\pi k\hbar}{\tau_0 \Delta E_e^F}\right)\sin\!\left(2\pi k\sqrt{\frac{\varepsilon_F}{\alpha_e}}\right),\qquad(26)$$

$$\sigma^h = -\sigma_{xx}^{\mathrm{cl}} \sum_{k=1}^{\infty} \frac{1}{2\pi k}\sqrt{\frac{\alpha_h}{\varepsilon_{OL} - \varepsilon_F}}\,\Psi\!\left(\frac{2\pi^2 kT}{\Delta E_h^F}\right)$$

$$\times \exp\!\left(-\frac{\pi k\hbar}{\tau_0 \Delta E_h^F}\right)\sin\!\left(2\pi k\sqrt{\frac{\varepsilon_{OL} - \varepsilon_F}{\alpha_h}}\right).\qquad(27)$$

Expressions (26) and (27) agree with the results of Refs. 6 and 7:

$$\sigma_{k,l}^{\pm} = \mp\,\sigma^{\mathrm{cl}} \frac{1}{4\pi^2 kl}\sqrt{\frac{\alpha_e}{\varepsilon_F}}\sqrt{\frac{\alpha_h}{\varepsilon_{OL} - \varepsilon_F}}\,\Psi\!\left(2\pi^2 T\!\left(\frac{k}{\Delta E_e^F}\right.\right.$$

$$\left.\left.\mp\frac{l}{\Delta E_h^F}\right)\right)\exp\!\left(-\frac{\pi k\hbar}{\tau_0}\!\left(\frac{k}{\Delta E_e^F} + \frac{l}{\Delta E_h^F}\right)\right)$$

$$\times \cos\!\left(2\pi\sqrt{\frac{\varepsilon_F}{\alpha_e}}\pm 2\pi l\sqrt{\frac{\varepsilon_{OL} - \varepsilon_F}{\alpha_h}}\right),\qquad(28)$$

where

$$\Psi(x) = \frac{x}{\sinh x}.$$

Expressions (26)–(28) for $\sigma^{e,h}$ and $\sigma_{k,l}^-$ are given for any T, the contribution $\sigma_{k,l}^+$ is determined by expression (28) if at least one of the following two conditions is met:

$$T \ll |E_{k,l} - \varepsilon_F|,\qquad(29)$$

$$T \ll \min\{\alpha_e^{1/4} E_{k,l}^{3/4},\ \alpha_h^{1/4}(\varepsilon_{OL} - E_{k,l})^{3/4}\}.\qquad(30)$$

Condition (30) describes the region near $T=0$ in which the temperature dependence of $\sigma_{k,l}^+$ can be neglected.

In the opposite case, when the condition

$$T \gg |E_{k,l} - \varepsilon_F|\qquad(31)$$

holds along with at least one of the inequalities

$$T \gg \alpha_e^{1/4} E_{k,l}^{3/4},\quad T \gg \alpha_h^{1/4}(\varepsilon_{OL} - E_{k,l})^{3/4},\qquad(32)$$

the expression for $\sigma_{k,l}^+$ will have the form

$$\sigma_{k,l}^+ = -\sigma^{\mathrm{cl}} \frac{1}{8\pi^2 klT}\sqrt{\frac{\alpha_e}{E_{k,l}}}\sqrt{\frac{\alpha_h}{\varepsilon_{OL} - E_{k,l}}}$$

$$\times \frac{1}{\sqrt{k/\sqrt{\alpha_e E_{k,l}^3} + l/\sqrt{\alpha_h(\varepsilon_{OL} - E_{k,l})^3}}}$$

$$\exp\!\left(-\frac{\pi\hbar}{2\tau_0}\!\left(\frac{k}{\sqrt{\alpha_e E_{k,l}}} + \frac{l}{\sqrt{\alpha_h(\varepsilon_{OL} - E_{k,l})}}\right)\right)$$

$$\times \cos\!\left(2\pi k\sqrt{\frac{E_{k,l}}{\alpha_e}} + 2\pi l\sqrt{\frac{\varepsilon_{OL} - E_{k,l}}{\alpha_h}} - \frac{\pi}{4}\right).\qquad(33)$$

The oscillation frequency of the contributions (26)–(28), as in the case $T=0$, is determined by $\tau(\varepsilon_F)$ (but the coefficients of proportionality in formula (17) for $T\neq 0$ will be different for different harmonics). The oscillation frequency of contribution (33) is determined by $\tau(E_{k,l})$ and is not necessarily a combination of the frequencies of the low-temperature contributions (26) and (27).

In formulas (25)–(28) and (33) and in conditions (29) and (31) one can restrict consideration to the case of small k,l, since the quantum oscillations are exponentially suppressed by the Dingle factor as these indices increase.

CONCLUSIONS

We have shown that the presence of an elastic short-range impurity can give rise to high-temperature oscillations.

Unlike the case of valleys with the same type of charge carrier, when QHTOs would be expected only at values of ΔE at the Fermi level which are close to multiples, in the case of two types of charge carriers the high-temperature character of the oscillations is manifested at any values of ΔE_e and ΔE_h, reaching a maximum amplitude at values which are multiples. Indeed, the presence of electron and hole valleys leads to a difference in the signs in the temperature factor and in the argument of the cosine in formula (28), i.e., the contribution $\sigma_{k,l}^+$ will be simultaneously higher-temperature and higher-frequency in comparison with the contributions (26) and (27) (as in the case of magnetic quantization; see Refs. 13–15). In the case of two groups of

charge carriers of the same type those signs will be the same, and the high-temperature oscillations will be low-frequency (see Ref. 16 for the case of magnetic quantization, where the role of the two groups of charge carriers is played by regions near the extremal cross sections).

Because of the unequal spacing of the size-quantized energy spectrum, the condition of multiples, $l\Delta E_e = k\Delta E_h$, can be satisfied only in regions of momentum space which are characterized by an energy $E_{k,l}$. The latter, together with ε_F, can determine the frequency and amplitude of the size oscillations and the character of the temperature dependence of the conductivity. Here the frequency of the QHTOs need not be a combination of the frequencies of the low-temperature modes of oscillation.

The author thanks Prof. V. G. Peschansky for valuable comments which decided the key points of this paper, and O. V. Kirichenko for his unflagging interest in this study and for valuable discussions. The author is grateful to Yu. F. Komnik for an understanding of how matters stand with the large volume of experimental material and for the choice of problem.

*E-mail: kozlov@ilt.kharkov.ua

[1] Yu. F. Komnik, *Physics of Metal Films. Size and Structure Effects* [in Russian], Atomizdat, Moscow (1979).
[2] Yu. F. Komnik and E. I. Bukhshtab, Zh. Éksp. Teor. Fiz. **54**, 63 (1968) [Sov. Phys. JETP **27**, 34 (1968)].
[3] Yu. F. Komnik, E. I. Bukhshtab, Yu. V. Nikitin, and V. V. Andrievsky, Zh. Éksp. Teor. Fiz. **60**, 669 (1971) [Sov. Phys. JETP **33**, 364 (1971)].
[4] H. A. Combet and J. Y. Le Traon, Solid State Commun. **6**, 85 (1968).
[5] J. Y. Le Traon and H. A. Combet, J. Phys. **30**, 419 (1969).
[6] V. B. Sandomirsky, Zh. Éksp. Teor. Fiz. **52**, 158 (1967) [Sov. Phys. JETP **25**, 101 (1967)].
[7] I. O. Kulik, JETP Lett. **5**, 345 (1967).
[8] Yu. A. Bogod, V. B. Krasovistsky (Krasovitsky), and V. G. Gerasimechko, Zh. Éksp. Teor. Fiz. **66**, 1362 (1974) [Sov. Phys. JETP **39**, 667 (1974)].
[9] Yu. A. Bogod, Vit. B. Krasovitsky, and E. T. Lemeshevskaya, Fiz. Nizk. Temp. **9**, 832 (1983) [Sov. J. Low Temp. Phys. **9**, 431 (1983)].
[10] Vit. B. Krasovitsky, V. V. Khotkevich, A. G. M. Jansen, and P. Wyder, Fiz. Nizk. Temp. **25**, 903 (1999) [Low Temp. Phys. **25**, 677 (1999)].
[11] D. Shoenberg, *Magnetic Oscillations in Metals*, Cambridge University Press, Cambridge (1984), Mir, Moscow (1986).
[12] V. L. Gurevich, JETP Lett. **5**, 210 (1967).
[13] V. M. Polyanovsky, JETP Lett. **46**, 132 (1987).
[14] V. M. Polyanovsky, Ukr. Fiz. Zh. **33**, 1575 (1988).
[15] V. M. Polyanovsky, Ukr. Fiz. Zh. **34**, 459 (1989).
[16] O. V. Kirichenko and I. V. Kozlov, Fiz. Nizk. Temp. **28**, 509 (2002) [Low Temp. Phys. **28**, 359 (2002)].
[17] M. V. Kartsovnik, P. D. Grigoriev, W. Biberacher, N. D. Kushch, and P. Wyder, Phys. Rev. Lett. **89**, 126802 (2002).
[18] R. Kubo, J. Phys. Soc. Jpn. **12**, 570 (1957); Russian translation: *Voprosy Kvantovoĭ Teorii Neobratimykh Protsessov*, V. L. Bonch-Bruevich (ed.), Izd. Inostr. Lit., Moscow (1961), p. 39.
[19] A. A. Abrikosov, A. P. Gor'kov, and I. E. Dzyaloshinskiĭ, *Methods of Quantum Field Theory in Statistical Physics*, Prentice-Hall, Englewood Cliffs, NJ (1963), Fizmatgiz, Moscow (1962).
[20] S. Doniach and E. H. Sondheimer, *Green's Functions for Solid State Physicists*, Imperial College Press, London (1998).
[21] V. G. Skobov, Zh. Éksp. Teor. Fiz. **39**, 689 (1960) [Sov. Phys. JETP **12**, 993 (1961)].
[22] V. V. Andreev and A. M. Kosevich, Zh. Éksp. Teor. Fiz. **43**, 1061 (1962) [*sic*].

Translated by Steve Torstveit

QUANTUM EFFECTS IN SEMICONDUCTORS AND DIELECTRICS

Rate of exciton scattering and exciton absorption in crystals with LO-phonon dispersion

N. I. Grigorchuk*

Bogolyubov Institute for Theoretical Physics of the National Academy of Science of Ukraine, 14-b Metrologichna St., Kiev 03143, Ukraine

The Ridley–Babiker relation for the LO-phonon energy is used to obtain an exact formula for the exciton scattering rate in the one-phonon approximation. The effect of LO-phonon dispersion on the frequency and temperature dependence of the exciton attenuation is studied theoretically for models of polar crystals with large and small exciton radii. It is shown that the role of LO-phonon dispersion is essentially different in processes with phonon absorption and phonon emission. For some fixed frequency interval, it is established that the effect of dispersion on exciton scattering changes with temperature. The TlBr and ZnS crystals are used as models for illustrations. © *2003 American Institute of Physics.* [DOI: 10.1063/1.1630720]

1. INTRODUCTION

The exciton–phonon interaction is one of the most important factors affecting device performance through the exciton mobility, intrasubband and intersubband scattering rates,[1] etc. The scattering of excitons by polar optical phonons largely governs a number of properties of semiconductor materials[2,3] and plays a dominant role in energy dissipation processes.[4]

Usually the special case in which the bulk optical modes are dispersionless has been considered, i.e., the longitudinally polarized optical (LO) and transversely polarized optical (TO) waves are assumed to propagate at fixed frequencies ω_{LO} and ω_{TO} regardless of their wavelength (the Einstein approximation).

For a real material, however, due to anisotropy of the macroscopic electric field produced by the polarization, the phonon modes exhibit dispersion, which is associated with the fact that different wave vectors vibrate at different frequencies, i.e., with the dependence of frequency on the both magnitude and direction of the phonon wave vector.

The neglect of dispersion in continuum models leads to the situation where all LO modes are degenerate.[5,6] Without dependence on the wave vector it is impossible to match the frequencies of LO modes across an interface. More fundamentally, without dispersion it is impossible to construct a quantum theory of vibrational fields.[7]

It is well established that the LO-phonon dispersion significantly changes the low-frequency asymptotics of the conductivity[8] and can play the most important role in low-dimensional structures, especially for polaron mobility in 1D conductors.[9] In Ref. 10 it was indicated that dispersion of the phonon energy may wash out the oscillation in the angle-resolved photoemission spectrum for a strongly coupled electron–phonon system.

In spite of these investigations, however, the essential properties of the exciton scattering by phonons are not fully understood yet. Though the microscopic characteristics of the scattering rate for dispersionless optical modes are now well established, the treatment of this quantity taking into consideration the finite width of the bulk LO phonon band, to our knowledge, has not been carried out before for concrete models of dispersion.

The main purpose of this paper is to present the results of calculations of the effect of LO-phonon dispersion on the frequency and temperature dependence of the exciton attenuation in polar crystals, using the Ridley–Babiker relation[7] as the model for the LO-phonon dispersion.

Our final goal is to propose an exact analytical formula for the exciton scattering rate, which is simple enough to be used for calculations of various quantities related to the exciton–LO-phonon scattering in crystals with a large and small exciton radii.

The rest of the paper is organized as follows. The basic formulas for the task are presented in Sec. II. Section III is devoted to discussing the results, and Sec. IV contains the conclusions.

2. BASIC FORMULAS

It is supposed that an exciton, moving coherently in a phonon environment, can be described with a Bloch wave. Then, in the case of weak exciton–phonon coupling, the one-phonon scattering processes play the most important role.

We will use a quadratic approximation for the dependence of the exciton energy on quasimomentum, while for the dispersion of long-wavelength bulk LO modes we adopt the Ridley–Babiker relation[7] in the form:

$$\Omega^2(q) = \Omega_0^2 - \hbar^2 q^2 v_L^2, \tag{1}$$

where Ω_0 is the zone-center phonon energy with momentum $q=0$, $v_L^2 = c_{11}/\rho$, c_{11} is the optical-mode elastic constant, and ρ is the reduced mass density.

We will consider the exciton–polar-LO-phonon interaction within a bulk-phonon model in which the usual Fröhlich interaction with LO phonons of the material is assumed.[11] If

one treats the divergence of the lattice polarization as a source of induced potential, then in the case of independent interaction of an electron and hole with the lattice (as with a continuum), the coupling function for Wannier excitons interacting with LO phonons may be chosen in the following form, similar to these given in Refs. 12 and 13:

$$G_{LO}(q) = \sqrt{\frac{2\pi e^2}{V}\left(\frac{1}{\varepsilon_\infty} - \frac{1}{\varepsilon_0}\right)} \frac{\sqrt{\Omega_{LO}(q)}}{q}[(1$$

$$+ \alpha_e^2 q^2)^{-2} - (1 + \alpha_h^2 q^2)^{-2}]. \tag{2}$$

Here $M = m_e + m_h$, m_e is the electron mass and m_h is the hole mass, $\alpha_i = (r_{ex}/2)(m_i/M)$, $i = e, h$, and r_{ex} is the exciton radius. In other words, expression (2) describes the interaction of an electron–hole dipole with the lattice via its polarizability.

An exciton colliding with phonons is damped with a probability Γ that can be calculated by means of the imaginary part of mass operator.[11] Substituting Eqs. (1), (2) of the present paper into Eq. (2) of Ref. 13 and integrating over all angles and phonon momenta, we obtain in the one-phonon approximation the following exact formula for the exciton scattering rate:

$$\Gamma^\pm(\omega, T) = 2\sqrt{M\Omega_0}\frac{e^2}{\hbar}\left(\frac{1}{\varepsilon_\infty} - \frac{1}{\varepsilon_0}\right)$$

$$\times \frac{1 - d_L\left(\frac{q_\pm}{q_0}\right)^2}{\left|\frac{q_\pm}{q_0}\left(d_L \pm \sqrt{1 - d_L\left(\frac{q_\pm}{q_0}\right)^2}\right)\right|}$$

$$\times \left[\frac{1}{\left[1 + \beta_e^2\left(\frac{q_\pm}{q_0}\right)^2\right]^2} - \frac{1}{\left[1 + \beta_h^2\left(\frac{q_\pm}{q_0}\right)^2\right]^2}\right]^2$$

$$\times \left\{\frac{1}{\exp\left[\frac{\Omega_0}{k_B T}\sqrt{1 - d_L\left(\frac{q_\pm}{q_0}\right)^2}\right] - 1} + \frac{1}{2}\mp\frac{1}{2}\right\}, \tag{3}$$

where Γ^+ describes processes with phonon creation and Γ^- the processes with phonon annihilation ($\Gamma^+ + \Gamma^- = \Gamma$), and

$$\left(\frac{q_\pm}{q_0}\right)^2 = 2\left[\frac{\hbar\omega - E_0}{\Omega_0} - d_L \pm \sqrt{1 + d_L^2 - 2d_L\frac{\hbar\omega - E_0}{\Omega_0}}\right], \tag{4}$$

$$\beta_i = \alpha_i q_0, \quad q_0^2 = M\Omega_0/\hbar^2, \quad d_L = Mv_L^2/\Omega_0, \tag{5}$$

E_0 is the exciton band bottom energy.

The frequencies should satisfy the following conditions:

$$\mp\Omega_0 \leqslant \hbar\omega - E_0 \leqslant \Omega_0\left[\frac{1}{2}\left(\frac{q_{max}}{q_0}\right)^2 \mp \sqrt{1 - d_L\left(\frac{q_{max}}{q_0}\right)^2}\right]. \tag{6}$$

They are due to the inequalities $0 \leqslant q_\pm \leqslant q_{max}$, which, in turn, arise from the energy conservation law. The upper sign in Eq. (6) is for the Γ^+ processes. The value d_L can be

TABLE I. Values of physical parameters for ionic crystals.

	ε_0	ε_∞	$\frac{m_e}{m_0}$	$\frac{m_h}{m_0}$	$\Omega_0,$ cm^{-1}	$r_{ex},$ Å	$a,$ Å	α	$c_{11}\cdot 10^{11},$ dyn/cm^2
TlBr*	35.1	5.4	0.18	0.38	115	152.1	3.97	3.62	3.78
ZnS**	8.6	5.2	0.25	0.59	352	25.9	5.41	1.23	10.5

Comment: *Ref. 16; **Ref. 17. The values of the constant c_{11} are given using the room-temperature data of Ref. 18.

considered as a parameter describing the dispersiveness of the Lth mode of optical lattice vibrations in a polar crystal. Putting $q_{max} = 2q_0$, one finds the limits of variation for the dispersion parameter: $0 \leqslant d_L \leqslant 1/4$. Though for any crystal the value of d_L is quite definite, to show the effect of the phonon dispersion it was assumed to vary. In the case when phonon dispersion is neglected ($d_L = 0$), Eq. (3) can be reduced to the form known from earlier works (see, for example, Ref. 14).

To illustrate the effect of LO-phonon dispersion on the frequency and temperature dependence of the exciton damping, we have chosen TlBr and ZnS crystals as the model. The selected crystals seem to have the most contrasting parameters (see Table I).

3. DISCUSSION OF RESULTS

The frequency dependence of exciton damping for TlBr and ZnS crystals is shown in Figs. 1 and 2. The calculations were performed at room temperature ($T = 300$ K), for which the effect of the dispersion is most pronounced. As is seen from the figures, the frequency dependence of the damping represents a simple two-hump curve (in accordance with the processes involving the absorption and emission of the LO phonons in the crystal), separated from each other by the frequency Ω_0.

The exciton scattering starts at the frequency $(E_0 - \Omega_0)\hbar^{-1}$ and rises with increasing difference in the effective masses of electron and hole. This rise is restrained by the decrease of the exciton–phonon coupling with increasing wave vector $\mathbf{q}$, when the phonon wavelength becomes less than the exciton radius. Competition of these factors results
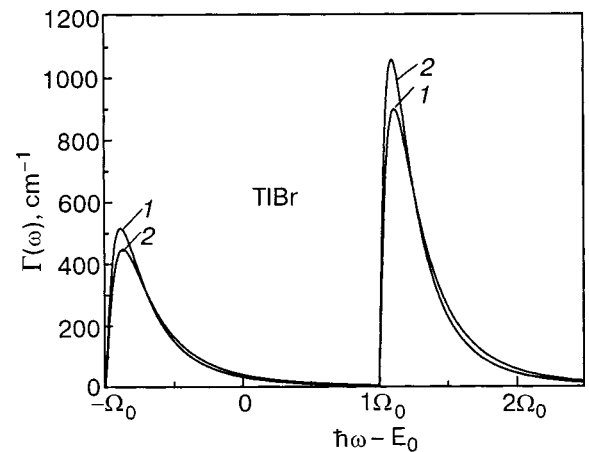
FIG. 1. Frequency dependence of the exciton damping for TlBr crystal at room temperature for different values of the LO-phonon dispersion: $d_L = 0$ (1), $d_L = 1/4$ (2).
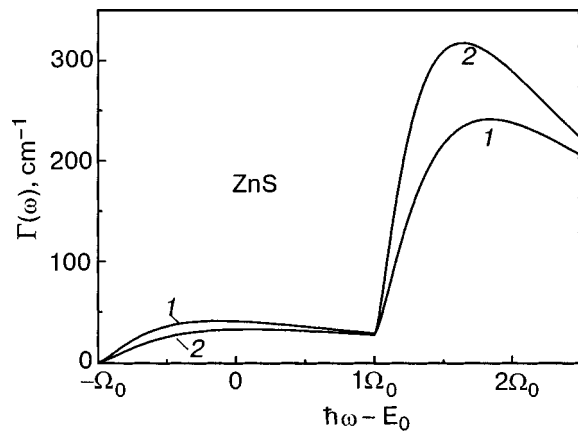
FIG. 2. Frequency dependence of the exciton damping for ZnS crystal at room temperature for different values of the LO-phonon dispersion: $d_L = 0$ (*1*), $d_L = 1/4$ (*2*).

in the appearance of the damping maximum. The weakening of the coupling is especially appreciable for crystals with large exciton radii (such as TlBr) and is poorly manifested for crystals with smaller exciton radii (such as ZnS), for which the maximum of the exciton–phonon coupling is displaced to shorter wavelengths or even may go far outside the frequency limits for one-phonon processes.

Though the free excitons exist only at $\hbar\omega > E_0$, the exciton scattering (as is seen from Figs. 1 and 2) takes place below the exciton band bottom as well. To avoid any misunderstanding, it is necessary here to keep in mind that $\Gamma(\omega)$ describes the attenuation both of really existing free excitons and of excitons with renormalized energy in a mass-operator denominator. Thus at photon energies exceeding the exciton band bottom energy, the scattering occurs on free excitons (which scatter by photon absorption with phonon emission), whereas at lower photon energies, the annihilation of a photon can occur only upon exciton creation with simultaneous phonon absorption to compensate the lacking photon energy.

A more realistic case is realized when the finite width of the bulk LO phonon band is taken into account (curves *2* in Figs. 1 and 2). The effect of LO-phonon dispersion on the exciton scattering differs significantly for processes involving phonon absorption and emission. Whereas in processes with a phonon absorption, an increase of the phonon dispersion results in both a reduction of the exciton scattering rate and a shift of its maximum to the short wavelength side, in processes with phonon emission, on the contrary, a faster rise of exciton attenuation and a shift of its maximum to the long-wavelength side have been established.

The shift of the attenuation maxima is more considerable for crystals with small exciton radii (ZnS; Fig. 2), whereas the change in intensities is more essential for crystals with large exciton radii (such as TlBr). For the former, the maximum is generally poorly pronounced. Such a behavior corresponds to weakening of the exciton–phonon coupling for the frequency interval where the phonon wavelength exceeds the exciton radius.

As a rule, the exciton scattering in the crystal gradually increases with temperature,[15] but the character of this growth depends on various circumstances.

We take into account only the dispersion factor. The results of the calculations of the scattering rate versus tempera-
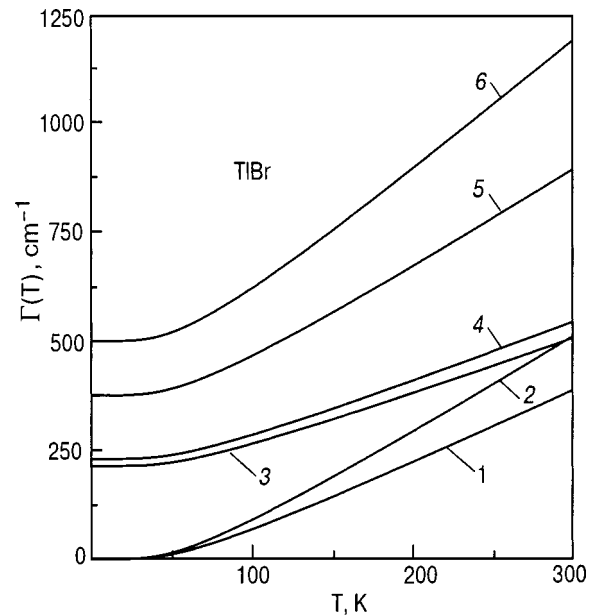

FIG. 3. Temperature dependence of the damping for the TlBr crystal at energies $\hbar\omega - E_0$ equal to: $-0.9\Omega_0$ (*1, 2*); $1.3\Omega_0$ (*3, 4*); $1.1\Omega_0$ (*5, 6*). With a phonon dispersion $d_L = 1/4$ (*1, 3, 6*) and without it (*2, 4, 5*).

ture for the TlBr and ZnS crystals are shown in Figs. 3 and 4. The calculations were carried out for some fixed frequencies with the LO-phonon dispersion taken into account (curves *1, 3, 6*) or without it (curves *2, 4, 5*).

For both crystals, in the frequency region $\omega \lesssim (E_0 + \Omega_0)\hbar^{-1}$ we have found that $\Gamma \to 0$ at $T \to 0$. That corresponds to the usual theoretical predictions.[15] But in the range $\hbar\omega - E_0 \gtrsim \Omega_0$ the damping becomes a finite quantity at zero temperature, owing to the nonvanishing contribution of the processes with phonon emission.

Let us now consider the role of the dispersion factor in the temperature dependence of the exciton scattering in more detail. Comparing to the dispersionless case, one finds that, depending on the frequency, the manifestation of dispersion with temperature behaves in two opposite ways: taking the
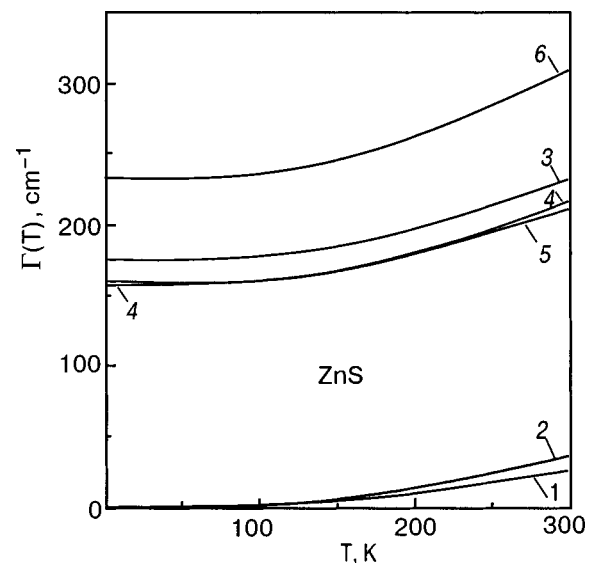

FIG. 4. Temperature dependence of the damping for the ZnS crystal at energies $\hbar\omega - E_0$ equal to: $-0.5\Omega_0$ (*1, 2*); $2.43\Omega_0$ (*3, 4*); $1.5\Omega_0$ (*5, 6*). With a phonon dispersion $d_L = 1/4$ (*1, 3, 6*) and without it (*2, 4, 5*).

LO-phonon dispersion into account stimulates either a decrease or an additional increase of the exciton scattering rate. For example, in the vicinity of the maximum of the LO-phonon absorption, at energies $\hbar\omega - E_0 = -0.9\Omega_0$ for TlBr and at $\hbar\omega = -0.5\Omega_0$ for ZnS, taking the dispersion into account results in a reduction of the attenuation (compare curves *1* and *2*). On the wings of the absorption range, beginning with the energy $\hbar\omega - E_0 \geq -0.7\Omega_0$ for TlBr and $\hbar\omega - E_0 \geq 0.2\Omega_0$ for ZnS, on the contrary, the dispersion enhances the damping.

The opposite tendency (to that described above) is developed in the vicinity of the phonon emission maximum (curves *5* and *6* in Figs. 3 and 4). It is especially appreciable at the energies $\hbar\omega - E_0 = 1.1\Omega_0$ for TlBr and at $\hbar\omega - E_0 = 1.5\Omega_0$ for ZnS, at which the contribution from an LO phonon band is the greatest (Figs. 1 and 2). Simultaneously, on the wings with phonon emission, the finite width of the bulk LO phonon band leads to a reduction of exciton attenuation (curves *3* and *4*). For TlBr crystals this occurs at frequencies $\omega \geq (E_0 + 1.3\Omega_0)\hbar^{-1}$ and for ZnS at $\omega \geq (E_0 + 2.43\Omega_0)\hbar^{-1}$.

The growth of exciton scattering with temperature is approximately uniform for most frequencies from the one-phonon interval, both with and without allowance for the dispersion. Such a tendency is well maintained for crystals with large exciton radii. However, for crystals with the small exciton radii, there was found a frequency interval in which the damping behaves sharply versus temperature when the finite width of the LO phonon band is taken into account. At low temperatures within some frequency interval it results in a phenomenon of increasing attenuation for the dispersionless model and further, beginning with some critical temperature T_{cr}, in an attenuation exceeding that obtained with dispersion taken into account (see curve *3* in Fig. 4). For the ZnS crystal $T_{cr} = 170$ K.

We have previously studied similar problems using a cosine law for the phonon dispersion.[13] Here, we have found the same trends for the temperature dependence of the scattering as well. The difference appears only in the $\Gamma(\omega)$ curves due to the specifics of the edges of the Brillouin zone. It seems that the approach based on the LO phonon dispersion model chosen here is more suitable for ionic crystals with weak and moderate coupling.

4. CONCLUSIONS

Using the Ridley–Babiker relation for the LO-phonon energy, we have obtained in the one-phonon approximation an exact analytical formula for the exciton scattering rate. It allows one to study theoretically the effect of LO-phonon dispersion on the exciton damping for polar crystals with large and small exciton radii.

We have found the role of LO-phonon dispersion to be different in processes with phonon emission and phonon absorption. Namely, with the phonon dispersion taken into account the maximum in the case of LO-phonon emission is shifted towards the direction of the exciton band bottom, which results in an increase of the absolute magnitude of the damping. At the same time, the maximum in the case of LO-phonon absorption is decreased and shifted to shorter wavelengths. Such frequency dependence is more pronounced for crystals with a large exciton radii.

For crystals with small exciton radii, a frequency interval has been found for which the exciton scattering behaves ambiguously with temperature when a phonon band is taken into account. At low temperature it results in a phenomenon wherein the damping without phonon dispersion, which is dominant at first at some frequencies, with increasing temperature becomes equal to or even smaller than the damping with the dispersion taken into account.

*E-mail: ngrigor@bitp.kiev.ua

[1] M. C. Tatham, J. F. Ryan, and C. T. Fozon, Phys. Rev. Lett. **63**, 1637 (1989).
[2] P. A. B. Miller, D. S. Chemla, D. J. Eilenberger *et al.*, Appl. Phys. Lett. **41**, 679 (1982).
[3] T. Hiroshima, Solid State Commun. **68**, 483 (1988).
[4] A. M. Kosevich, *Physical Mechanics for Real Crystals* [in Russian], Nauk. Dumka, Kiev (1981).
[5] K. Huang and B.-F. Zhu, Phys. Rev. B **38**, 13377 (1988).
[6] H. Gerecke and F. Bechstedt, Phys. Rev. B **43**, 7053 (1991).
[7] B. K. Ridley and M. Babiker, Phys. Rev. B **43**, 9096 (1991).
[8] A. A. Gogolin, Zh. Éksp. Teor. Fiz. **92**, 152 (1987).
[9] M. J. Rice and E. J. Mele, Solid State Commun. **35**, 487 (1980).
[10] A. S. Alexandrov and J. Ranninger, Phys. Rev. B **45**, 13109 (1992).
[11] G. D. Mahan, *Many-Particle Physics*, Kluwer Academic/Plenum Publishers, New York, Boston, Dordrecht, London (2000), p. 437.
[12] A. S. Davydov, *Theory of Molecular Excitons*, Plenum Press, New York-London (1971), p. 168.
[13] N. I. Grigorchuk and I. Yu. Goliney, Phys. Rev. B **60**, 5470 (1999).
[14] N. I. Grigorchuk, Phys. Lett. A **231**, 245 (1997).
[15] A. F. Lubchenko, V. M. Nitsovich, and M. V. Tkach, Phys. Status Solidi B **63**, 609 (1974).
[16] G. Iadonisi and F. Bassani, Nuovo Cimento D **2**, 1541 (1983).
[17] E. O. Kane, Phys. Rev. B **18**, 6849 (1978).
[18] M. P. Shaskolskaja (ed.), *Acoustic Crystals* [in Russian], Nauka, Moscow (1982).

LATTICE DYNAMICS

Heat capacity of solid solutions of deuteromethane in krypton. Nuclear spin conversion in CD$_4$ molecules

M. I. Bagatskii,* V. G. Manzhelii, D. A. Mashchenko, and V. V. Dudkin

B. Verkin Institute for Low Temperature Physics and Engineering of the National Academy of Sciences of Ukraine, 47, Lenin Avenue, 61103 Kharkov, Ukraine

A study is made of the heat capacity of the binary solid solutions $(CD_4)_{0.01}Kr_{0.99}$ (in the temperature interval $\Delta T = 0.9$–7 K) and $(CD_4)_{0.05}Kr_{0.95}$ ($\Delta T = 0.7$–20 K) and of the ternary solid solutions $(CD_4)_{0.01}Kr_{0.988}(O_2)_{0.002}$ ($\Delta T = 0.7$–11 K) and $(CD_4)_{0.05}Kr_{0.948}(O_2)_{0.002}$ ($\Delta T = 0.8$–4 K). The contribution of the rotational subsystem to the heat capacity of the solutions is separated out. The influence of temperature, oxygen impurities, and the interaction between the deuteromethane molecules on the effective conversion rate is studied. The energy differences between the lowest-lying levels of the nuclear spin species A and T of deuteromethane is determined, and the effective characteristic conversion times are found. Rapid conversion of isolated CD$_4$ molecules is observed in CD$_4$–Kr solutions. It is shown that in the CD$_4$–Kr solutions, as in CH$_4$–Kr solutions, a hybrid mechanism of conversion is dominant at low temperatures ($T < 1.4$ K), and the "bottleneck" governing the conversion rate is the intermolecular effective octupole–octupole interaction and the related probability of transfer of the conversion energy to phonons. © *2003 American Institute of Physics.*
[DOI: 10.1063/1.1630721]

INTRODUCTION

Studies of the physical properties of solid solutions of methane and deuteromethane in krypton can yield information about quantum effects in the rotational motion of isolated and mutually interacting spherical rotors in a crystal lattice for different rotational quantum parameters of the rotors.[1] The mass difference of the methane and deuteromethane molecules ($M_{CH_4}/M_{CD_4} = 0.8$) is relatively small, while their moments of inertia ($I_{CH_4}/I_{CD_4} = 0.508$), the total nuclear spins of the A, T, and E species of the CH$_4$ ($I = 2, 1, 0$) and CD$_4$ ($I = 4, 2, 0$) molecules, and the magnetic moments of the light atoms ($\mu_D/\mu_H = 0.306$) differ strongly. Therefore, the substitution of the CH$_4$ molecule in CH$_4$–Kr solutions by CD$_4$ molecules has a relatively weak effect on the translational subsystem and a substantial effect on the energy spectrum and physical properties of the rotational subsystem at helium temperatures, where the manifestations of quantum effects are maximal.

Deuteromethane and methane form single-phase solid solutions with krypton at concentrations $n < 70$ mole% deuteromethane and $n < 80$ mole% methane.[2] This permits study not only of the behavior of isolated rotors but also the interaction between rotors.

A clear quantum effect manifested on the macroscopic level is conversion—transitions between the A, T, and E nuclear spin species of the CH$_4$ and CD$_4$ rotors. Conversion establishes a thermodynamic equilibrium between the species. The study of conversion in solid methane and in solid solutions of methane in rare gases has been the subject of a

large number of experimental papers (see Refs. 2–6 and the literature cited therein), and the main regularities of the conversion in methane have been established. There is a single theoretical paper, by Berlinsky and Nijman,[7] in which it is hypothesized that the dominant mechanism of conversion in pure solid methane at low temperatures is a hybrid mechanism. According to Ref. 7, the maximum conversion rate is determined by the simultaneous intramolecular magnetic interaction between protons and the intermolecular octupole–octupole (OO) interaction between nearest-neighbor methane molecules in the lattice. The intramolecular interaction mixes the nuclear spin states and the intermolecular OO interaction brings about transitions between rotational states, with a transfer of the conversion energy to the lattice. Recently the first experimental confirmation of the dominance of the hybrid mechanism of conversion of CH$_4$ molecules at $T < 2.5$ K in Kr–CH$_4$ solutions has been obtained.[3] According to the theory,[7] the conversion rate in clusters of CH$_4$ molecules is significantly higher than the conversion rate of isolated CH$_4$ molecules (singles). This is the prediction that was confirmed in Ref. 3. Since the rotational constant of the CD$_4$ molecule is approximately half as large as that of the CH$_4$ molecule, an influence of conversion on the physical properties of CD$_4$–Kr solid solutions can be expected at lower temperatures than in CH$_4$–Kr solutions.

Up until our previous paper[8] (see below) there was no convincing proof that conversion is observed in solid deuteromethane and solid solutions containing deuteromethane.[2,5,6] There was the idea that because of the relatively small magnetic moment of the deuteron, conversion in CD$_4$ occurs

very slowly and does not show up in real experiments.[2,5,6]

We know of only one paper[9] devoted to measurement of the heat capacity of pure deuteromethane in the region 0.15–4 K in which the authors proposed that at temperatures below 0.25 K the increase in the thermal relaxation time in a sample of solid CD_4 after the heating of the calorimeter was turned off was possibly due to conversion of the CD_4 molecules.

We recently published a brief communication of the results of studies of the heat capacity of a solid solution of 5% CD_4 in Kr and of the same solution doped with 0.2% O_2 in the temperature interval 0.7–1.6 K.[8] In that paper the observation of nuclear spin conversion of CD_4 molecules in a krypton matrix was reported.

In the present study the research mentioned above[8] is extended to solutions with lower concentrations of deuteromethane (1% CD_4 in krypton and a solution of 1% CD_4 in Kr doped with 0.2% O_2) and to temperatures up to 20 K.

The main goal of the studies of Ref. 8 and the present study is the calorimetric investigation of nuclear spin conversion of deuteromethane molecules in CD_4–Kr solid solutions and in the same solutions doped with 0.2% O_2. Also, the information obtained in this study about the heat capacity and low-energy part of the rotational spectrum of the CD_4–Kr solid solution is of independent interest.

We note that the heat capacity of solid solutions of deuteromethane in rare gases has not been measured previously.

EXPERIMENT

In this paper and in Ref. 8 we studied the heat capacity of the binary solid solutions $(CD_4)_{0.01}Kr_{0.99}$ (in the temperature interval $\Delta T = 0.9–7$ K) and $(CD_4)_{0.05}Kr_{0.95}$ ($\Delta T = 0.7–20$ K) and of the ternary solid solutions $(CD_4)_{0.01}Kr_{0.988}(O_2)_{0.002}$ ($\Delta T = 0.7–11$ K) and $(CD_4)_{0.05}Kr_{0.948}(O_2)_{0.002}$ ($\Delta T = 0.8–4$ K). The measurements were made in a vacuum adiabatic calorimeter[10] by the pulsed heating method. A gaseous mixture with a specified impurity concentration was prepared at room temperature. The amount of the substance in the samples (around 0.4 mole) and the concentration of the components of the solutions were determined from PVT data with an error of 0.2%. The gases used had the following composition: CD_4—isotopic purity 99%, chemical purity 99.20% (N_2—0.50%, O_2—0.20%, CO—0.10%, and Ar<0.01%); Kr—purity 99.79% (Xe—0.2%, N_2—0.01%, O_2 and Ar <0.01%); O_2—purity 99.99% (N_2<0.01%). A solid solution was obtained in the calorimeter at $T \approx 85$ K by the condensation of the gaseous mixture to the solid phase. This ensured a uniform composition of the solution and a random distribution of the components of the solution. Before the start of the measurements the calorimeter with the heat switch closed was cooled to a temperature of ~0.5 K. Cooling the calorimeter with the samples from a temperature of 1.3 K required about 1 day (as was the case for $(CH_4)_n Kr_{1-n}$ samples[3,4]), which is many times longer than the cooling time in experiments with pure Kr. This indicates that the cooling of Kr samples containing a deuteromethane or methane impurity is accompanied by strong heat release. After the heat switch was opened, the calorimeter temperature increased for 3 h (at a rate dT/dt that decreased in time) to

~0.7 K. The heat capacity was measured as the temperature changed at a rate of $10^{-3}–10^{-4}$ K/min. The increase of the sample temperature ΔT_i during a single measurement of the heat capacity was around 10% of the initial temperature T_i. The heating time t_h was varied from 2 to 6 min. The effective time t_m of one measurement of the heat capacity, $t_m = t_h + t_e$, where t_e is the time required to achieve a nearly steady rate of change of the calorimeter temperature from the time the heating was turned off, varied from 50 to 10 min at temperatures in the range from 0.7 to 20 K, respectively. After the first series of measurements of the heat capacity in the temperature region 0.7–2.5 K subsequent series of measurements were made several times at temperatures above 1.3 K. A time of 4–5 h was required to achieve the necessary rate of change of the calorimeter temperature for the start of the measurements, $10^{-3}–10^{-4}$ K/min. The results of the measurements (at the times t_m indicated in Table II) were reproducible and did not depend on the temperature prehistory of the sample. The error of measurement of the heat capacity of the solutions was 6% at 0.8 K, 2% at 1 K, 1% at 2 K, and 0.5% above 4 K.

We note that what we call the heat capacity in this paper is the derivative of the heat transferred to the system with respect to temperature, regardless of whether or not the system is in equilibrium.

From the total heat capacity C_{sol} of the Kr–CD_4 binary solutions, under the assumption that the translational and rotational motions of the molecules are independent (as in the case of the Kr–CH_4 solutions[3,4]) we determined the rotational component $C_{rot} = C_{sol} - C_{tr}$, where C_{tr} is the translational component. C_{tr} is written as $C_{tr} = C_{Kr} + \Delta C_{tr}$, where C_{Kr} is the heat capacity of pure krypton and ΔC_{tr} is the change in the translational heat capacity as a result of the introduction of the lighter deuteromethane impurity in the lattice. ΔC_{tr} was calculated by the method proposed by Peresada[11,12] without the change in the force constants taken into account, for a ratio of mass of the impurity particles and matrix $m_{CD_4}/m_{Kr} = 0.25$. We made a preliminary measurement of the heat capacity of pure krypton, C_{Kr}, in the temperature range 0.7–20 K, and the results were in good agreement with the results of Refs. 13 and 14. The limiting value of the Debye temperature for $T \to 0$ K, $\theta_0 = 71.6$ K, agrees within the experimental error limits with the values $\theta_0 = 71.7$ K[13] and $\theta_0 = 71.9$ K.[14] In the case of the ternary solutions the heat capacity C_{rot} is written as $C_{rot} = C_{sol} - (C_{Kr} + \Delta C_{tr}) - C_{rot(O_2)}$, where $C_{rot(O_2)}$ is the heat capacity due to the rotational motion of the oxygen molecules. $C_{rot(O_2)}$ was taken into account with the use of the data of Ref. 15 on the heat capacity of Kr–O_2 solid solutions.

A detailed analysis of the behavior of $C_{rot}(T, n)$ was done in this study in the temperature region below 1.4 K. At $T = 1$ K the $C_{rot}(T, n)$ contribution to C_{sol} amounts to 40% for a molar concentration of CD_4 of $n = 1$%, 97% for $n = 5$%, 54% for $n = 1$% (with 0.2% O_2), and 92% for $n = 5$% (with 0.2% O_2).

TABLE I. Experimental values of the heat capacity C_{sol} at equilibrium vapor pressure for the binary solid solutions $(CD_4)_{0.01}Kr_{0.99}$ and $(CD_4)_{0.05}Kr_{0.95}$ and of the ternary solid solutions $(CD_4)_{0.01}Kr_{0.988}(O_2)_{0.002}$ and $(CD_4)_{0.05}Kr_{0.948}(O_2)_{0.002}$.

T, K	C_{sol}, J/(mole·K)	T, K	C_{sol}, J/(mole·K)	T, K	C_{sol}, J/(mole·K)	T, K	C_{sol}, J/(mole·K)
$(CD_4)_{0.01}Kr_{0.99}$							
0.9351	0.00857	1.6809	0.0654	2.247	0.1456	3.416	0.3719
1.0060	0.0124	1.7977	0.0709	2.263	0.1570	4.428	0.7139
1.1163	0.0182	1.7712	0.0724	2.384	0.1765	4.790	0.9033
1.3799	0.0320	2.003	0.1039	2.501	0.1969	6.766	2.352
1.4208	0.0341	2.054	0.1113	2.720	0.2336		
1.5137	0.0432	2.096	0.1030	2.924	0.2699		
1.6634	0.0544	2.234	0.1436	3.241	0.3368		
$(CD_4)_{0.01}Kr_{0.988}(O_2)_{0.002}$							
0.7347	0.0273	1.3168	0.0813	2.083	0.1520	3.509	0.4116
0.7839	0.0308	1.4514	0.0888	2.157	0.1527	3.877	0.5252
0.8179	0.0324	1.5952	0.1047	2.189	0.1691	4.987	1.035
0.8562	0.0399	1.6581	0.1019	2.225	0.1684	5.469	1.378
0.8627	0.0409	1.7700	0.1102	2.309	0.1822	6.583	2.229
0.9201	0.0475	1.8143	0.1229	2.418	0.2007	8.002	3.629
1.0913	0.0604	1.9332	0.1474	2.423	0.1896	10.22	6.316
1.1612	0.0669	1.9597	0.1332	2.476	0.1979	10.59	6.788
1.2004	0.0676	1.9693	0.1378	2.579	0.2223		
1.2410	0.0727	2.039	0.1481	2.851	0.2706		
1.2942	0.0774	2.047	0.1377	3.170	0.3351		
$(CD_4)_{0.05}Kr_{0.95}$							
0.7365	0.0969	1.7712	0.500	3.093	0.697	9.724	6.068
0.7930	0.125	1.9336	0.542	3.357	0.759	10.66	7.141
0.8450	0.160	1.9569	0.517	3.657	0.831	11.41	7.992
0.9028	0.179	1.9964	0.506	3.976	0.944	11.99	8.701
0.9557	0.221	2.057	0.544	4.341	1.090	13.06	9.887
1.0273	0.268	2.145	0.546	4.826	1.346	13.08	9.909
1.0847	0.278	2.217	0.554	5.373	1.699	13.81	10.54
1.1281	0.316	2.320	0.570	5.971	2.138	14.43	11.04
1.2025	0.356	2.440	0.582	6.614	2.650	15.29	11.82
1.3144	0.409	2.565	0.603	7.311	3.326	15.63	12.18
1.4935	0.459	2.706	0.614	8.081	4.069	19.12	15.67
1.6674	0.505	3.022	0.686	9.659	5.940		
$(CD_4)_{0.05}Kr_{0.948}(O_2)_{0.002}$							
0.8059	0.183	1.1588	0.388	1.8741	0.558	2.911	0.671
0.8416	0.220	1.2228	0.407	2.068	0.575	3.288	0.758
0.9036	0.251	1.3170	0.448	2.267	0.594	3.707	0.862
0.9720	0.282	1.4278	0.493	2.472	0.615		
1.0327	0.316	1.5609	0.503	2.684	0.635		
1.0952	0.327	1.6985	0.503	2.735	0.643		

RESULTS OF THE MEASUREMENTS. DISCUSSION

The experimental values of the heat capacity C_{sol} at equilibrium vapor pressure for the solid solution studied are presented in Table I.

It is most convenient to discuss the experimental data for the heat capacity of the rotational subsystem normalized by the deuteromethane concentration n in the solution and the universal gas constant R: $C_R = C_{rot}/(nR)$. The quantity C_R defined in that way is the reduced heat capacity of a mole of rotors. The temperature curves of C_R are presented in Figs. 1 and 3 in the temperature regions 0.7–20 K and 0.7–2 K, respectively. The values of the rotational heat capacity for
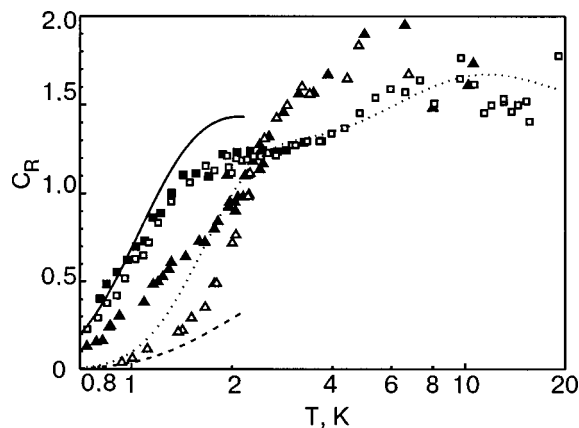
FIG. 1. Normalized rotational heat capacity $C_R = C_{rot}/(Rn)$ (n is the molar concentration of CD_4, and R is the universal gas constant) of the solid solutions $(CD_4)_{0.01}Kr_{0.99}$ ($\triangle$); $(CD_4)_{0.05}Kr_{0.95}$ ($\square$); $(CD_4)_{0.01}Kr_{0.988}(O_2)_{0.002}$ ($\blacktriangle$); $(CD_4)_{0.05}Kr_{0.948}(O_2)_{0.002}$ ($\blacksquare$). The calculated values: (——) and (— — —) are obtained from the spectrum of Ref. 16 (see Fig. 2) for the equilibrium and high-temperature ($x_A : x_T : x_E = 15:54:12$) distributions of the nuclear spin species of CD_4, respectively; ($\cdots\cdots$) is calculated from the spectrum for the free CD_4 molecule[17] with allowance for the energy levels up to rotational quantum number $J = 14$, inclusive.

the equilibrium $C_{R,eq}$ and the high-temperature $C_{R,high}$ distributions of the nuclear spin species of CD_4, calculated from the energy spectrum of CD_4 in the crystalline field of krypton[16] (see Fig. 2), are shown by the solid and dashed curves in Fig. 1. Also shown by the dotted curve in Fig. 1 are the values of $C_{R,eq}$ calculated for free CD_4 molecules with allowance for the energy levels up to rotational quantum number $J = 14$, inclusive.[17] Since the energy spectrum given in Ref. 16 contains only the levels with $J = 1$ and $J = 2$ and partially with $J = 3$ and $J = 4$ (see Fig. 2), comparison of the experimental heat capacities C_R with the calculated values $C_{R,eq}$ and $C_{R,high}$ is correct only for temperatures $T < 2.2$ K. $C_{R,eq}$ was calculated under the assumption of fast conversion, when the characteristic conversion times $\tau \ll t_m$, and over a time t_m a close to equilibrium distribution of species can be established. $C_{R,high}$ was calculated under the assumption that conversion is absent, and the high-

FIG. 2. Energy spectrum of the rotational motion of the free CD_4 molecule[17] and the CD_4 molecule in the crystalline field of krypton for the A, T, and E nuclear spin species.[16] J is the rotational quantum number, ε is the energy (the degeneracies of the levels are shown in parentheses to the right).

temperature equilibrium concentration ratio of the nuclear spin species of free CD_4 molecules ($x_A : x_T : x_E = 15:54:12$) is preserved.

It is seen in Fig. 2 that the energy spectra of the nuclear spin species of the CD_4 rotor are very different. At temperatures below 1.4 K and with rather rapid conversion the dominant contribution to the rotational heat capacity C_R of weak solutions of deuteromethane in krypton comes from transitions between the lowest levels of the A ($\varepsilon_{0A} = 0$ K) and T ($\varepsilon_{0T} = 4.7$ K) species of the molecules, with a change of energy $\varepsilon_{AT} = \varepsilon_{0T} - \varepsilon_{0A}$. In the experiment this contribution to the heat capacity C_R is determined by the number of molecules that have undergone transitions from level A (0 K) to level T (4.7 K) over the time t_m of a single measurement of the heat capacity. In the case of rapid conversion ($\tau \ll t_m$) the experimental values of the heat capacity C_R correspond to the equilibrium state of the system. In the limiting case of complete absence of conversion the concentration ratios of the species correspond to the high-temperature distribution, and $C_R = C_{A,R} + C_{T,R} + C_{E,R}$, where the heat capacities $C_{A,R}$, $C_{T,R}$, and $C_{E,R}$ are determined only by transitions within each species. In the latter case the heat capacity found experimentally is substantially lower than the equilibrium heat capacity.

In Ref. 8 we reported the observation of nuclear spin conversion of CD_4 molecules in a krypton matrix. The conversion in the CD_4–Kr samples (as in the CH_4–Kr samples) is manifested first of all in strong heat release on cooling of the calorimeter with the samples to the minimum temperature of the experiment. This effect cannot be due to decomposition of the solution, since the experimental values of the heat capacities C_R are reproducible (at equal values of t_m) and do not depend on the temperature prehistory of the sample. Analysis of the time dependence of the temperature of the sample after calorimetric heating makes it possible in principle to estimate the characteristic conversion time. However, because of experimental difficulties (primarily the nonideal adiabaticity of the calorimeter) such estimates have a very large error. More-reliable quantitative information about the conversion can be obtained from analysis of the results of the heat-capacity measurements (see below).

From an analysis of the characteristic temperature and concentration behavior of the reduced heat capacities C_R of the solutions with 1% and 5% CD_4 in Kr and of the same solutions doped with 0.2% O_2, one can draw the following qualitative conclusions.

1. There are a number of facts attesting to the influence of conversion on the heat capacity. At $T = 1.4$ K the experimental values of the normalized heat capacity C_R of the rotational subsystem of the solutions $(CD_4)_{0.05}Kr_{0.95}$ and $(CD_4)_{0.01}Kr_{0.99}$ are larger by factors of 16 and 1.6, respectively, than the values $C_{R,high}$ calculated from the spectrum of CD_4 in the crystalline field of krypton[16] for the high-temperature distribution of nuclear spin species of the CD_4 molecules (see Fig. 1). The introduction of 0.2% O_2 into the solution $(CD_4)_{0.05}Kr_{0.95}$ had an insignificant effect on the experimental values of C_R. In the solution $(CD_4)_{0.05}Kr_{0.95}$ the experimental values of C_R are close to the values $C_{R,eq}$ calculated for the equilibrium distribution of the species. This last argument is valid because the rotational energy lev-
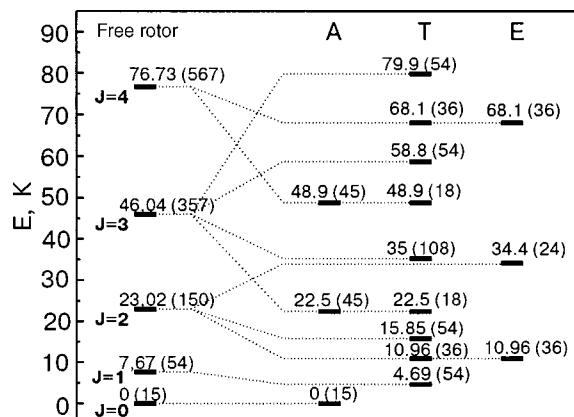
TABLE II. Parameters determining the heat capacity of the rotational sub-system in the binary solid solutions $(CH_4)_n Kr_{1-n}$ (Ref. 4) and $(CD_4)_n Kr_{1-n}$ and ternary solid solutions $(CH_4)_n Kr_{1-n-0.002}(O_2)_{0.002}$ (Refs. 3 and 4), and $(CD_4)_n Kr_{1-n-0.002}(O_2)_{0.002}$ at temperatures $T < 1.4$ K.

	CD$_4$			CH$_4$	
n, %	1 (with O$_2$)	5 (with O$_2$)	5	1 (with O$_2$)	5
ε_{AT}, K	4.8 ± 0.2	4.7 ± 0.2	4.7 ± 0.2	11.7 ± 0.4	11.7 ± 0.7
K', %	55	95	85	72	8
t_m, min	50	44	44	23	11
τ, min	63	15	23	18	132

Note: ε_{AT} is the energy difference between the lowest levels of the A and T species of the methanes (CH$_4$, CD$_4$); t_m is the mean characteristic time for one heat-capacity measurement; τ is the effective characteristic time for conversion of the methane molecules, K' is the ratio of the number of CD$_4$ (CH$_4$) molecules that have undergone a transition from the state ε_{0A} to the state ε_{0T} during the time t_m in the real experiment, to the corresponding number for the equilibrium distribution of the nuclear spin species of CD$_4$ (CH$_4$).

els with $J = 1$ for the solutions with 5% and 1% CD$_4$ coincide within the error limits (see Table II below).

2. In the region of temperatures below 1.4 K the hybrid mechanism of conversion proposed by Berlinsky and Nijman[7] is dominant in the binary solutions Kr–CD$_4$ studied here (as in Kr–CH$_4$ solutions). The evidence for this is: first, the strong concentration dependence of the heat capacity C_R of the binary solutions Kr–CD$_4$, due to the rapid rise in the conversion rate with increasing CD$_4$ concentration (and, accordingly, with increasing number and size of the clusters of CD$_4$ molecules in the solutions), and second, the strong increase in the heat capacity C_R in the binary solution $(CD_4)_{0.01}Kr_{0.99}$ when a 0.2% oxygen impurity is introduced to that solution, due to acceleration of the conversion rate of matrix-isolated CD$_4$ molecules in the lattice of krypton with an oxygen impurity.

3. A comparison of the experimental heat capacities C_R of the Kr–CD$_4$ solutions and these same solutions doped by small concentrations of oxygen allows us to obtain information about the temperature dependence of the conversion rates in the investigated solutions. With increasing temperature above 1.4 K the values of C_R for the solution with 1% CD$_4$ in Kr and this same solution with 0.2% O$_2$ (see Figs. 1 and 3) rapidly come closer together, which attests to an increase in the rate of conversion of CD$_4$ molecules isolated in the krypton lattice with temperature. This is apparently due to the contribution to the conversion made by the CD$_4$ rotational energy levels lying above the level with $J = 1$. An analogous contribution to the conversion has been observed previously in solid methane,[18] in CH$_4$–Kr solid solutions,[3,4,18] and in CH$_3$D–Ar solutions[19] at higher temperatures. For $T \leqslant 1.4$ K in the solid solutions with 5% CD$_4$ and in the solution with 1% CD$_4$ and 0.2% O$_2$ this contribution is small compared to the rapidly occurring conversion brought about by the hybrid mechanism and the oxygen impurities.

4. At $T > 2.5$ K over the effective time t_m of one heat-capacity measurement a close to equilibrium distribution of

the nuclear spin species of deuteromethane is achieved in all the solutions studied. This follows from the fact that for $T > 2.5$ K the heat capacities C_R in the investigated binary and ternary solutions are all the same. The O$_2$ impurities have no effect on the heat capacities C_R of the Kr–CD$_4$ solutions (at an appreciable rate of conversion) only in those cases when an equilibrium distribution of the species is achieved over a time t_m in the absence of oxygen.

Let us now turn to a more detailed analysis of the results obtained at temperatures below 1.4 K, where the experimental heat capacity C_R is determined by the number of CD$_4$ molecules that over the time t_m of one heat-capacity measurement have undergone a transition from the lowest level of the A species (ε_{0A}) to the lowest level of the T species (ε_{0T}) with an energy change $\varepsilon_{AT} = \varepsilon_{0T} - \varepsilon_{0A}$. We recall that before the experiment the samples were held for about a day at the lowest temperature of the measurements in order that the overwhelming majority of the CD$_4$ molecules would be in the ground state of the A species. The changes of the populations of the levels with $J > 1$ (see Fig. 2) can be neglected, since they are relatively high-lying. In the case of rapid conversion, when thermodynamic equilibrium can be established over the time t_m, one has for a mole of rotors

$$C_{R,eq} = (\varepsilon_{AT}/T)^2 (g_1/g_0)\exp(-\varepsilon_{AT}/T)/$$
$$(1 + (g_1/g_0)\exp(-\varepsilon_{AT}/T))^2, \tag{1}$$

where g_0 and g_1 are the degeneracies of the levels of the A and T species, respectively. The ratio

$$K' = C_R / C_{R,eq} \tag{2}$$

is equal to the fraction of CD$_4$ molecules from the case of the equilibrium distribution that in the real experiment have undergone transition from the lowest level of the A species to the lowest level of the T species over the time t_m of a single heat-capacity measurement.

For optimal description of the experimental heat capacities C_R at $T < 1.4$ K we varied two parameters: ε_{AT} and K'. The values which we determined for ε_{AT} and K' are given in Table II together with the values of ε_{AT} and K' for CH$_4$–Kr solutions.[3,4] In Fig. 3 the lines show the heat capacities C_R
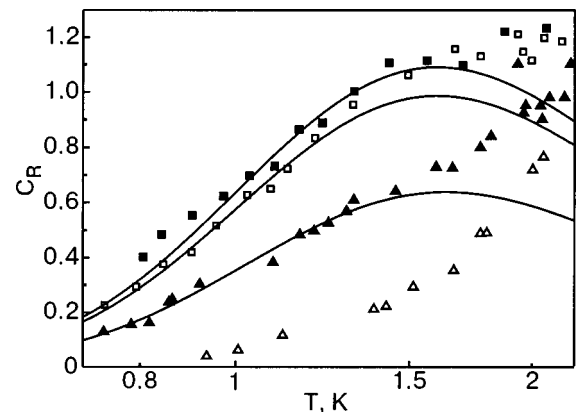

FIG. 3. Normalized rotational heat capacity of the solid solutions $(CD_4)_{0.01}Kr_{0.99}$ ($\triangle$); $(CD_4)_{0.05}Kr_{0.95}$ ($\square$); $(CD_4)_{0.01}Kr_{0.988}(O_2)_{0.002}$ ($\blacktriangle$); $(CD_4)_{0.05}Kr_{0.948}(O_2)_{0.002}$ ($\blacksquare$). The curves show the heat capacities C_R calculated for a two-level system with the use of expressions (1) and (2) and the values of ε_{AT} and K' given in Table II.

which we calculated using expressions (1) and (2) and the values obtained for ε_{AT} and K'. The values of ε_{AT} for the solutions studied are in good agreement with the theoretical value $\varepsilon_{AT} = 4.7$ K (Ref. 16) and the value $\varepsilon_{AT} = 4.75$ K obtained by the method of inelastic neutron scattering in a CD_4–Ar solid solution with a CD_4 concentration of less than 1% at $T = 2$ K.[20] The value $\varepsilon_{AT} = 4.8$ K for the solution with 1% CD_4 and 0.2% O_2 in Kr is 37% smaller than the value $\varepsilon_{AT,\text{free}} = 7.67$ K for the free CD_4 rotor.[17] In the case of CH_4 molecules in a Kr matrix $\varepsilon_{AT} = 11.7$ K[3,4] and is 23% lower than the value $\varepsilon_{AT,\text{free}} = 15.12$ K for the free CH_4 rotor. The difference of the ratios $(\varepsilon_{AT,\text{free}} - \varepsilon_{AT})/\varepsilon_{AT,\text{free}}$ for CH_4 (23%) and CD_4 (37%) is due to the larger value of the rotational quantum parameter of the CH_4 rotor.[1] The larger the rotational quantum parameter of the rotor, the less influence the crystalline field has on its spectrum.

In the case of a solution with 1% CD_4 at temperatures below 1.4 K we could not satisfactorily describe the experiment with the use of equations (1) and (2) with a constant value of K'. At temperatures near 1 K for $\varepsilon_{AT} = 4.8$ K (the value obtained for the solution with 1% CD_4 and 0.2% O_2), we have $K' = 0.1$. With increasing temperature the value obtained for K' increases monotonically, approaching the value $K' = 1$. As we have said, this is due to the increase in the conversion rate with increasing temperature.

A comparison of the heat capacities at temperatures below 1.4 K for solutions containing 1% CD_4 with and without impurity oxygen permits estimation of the influence of the oxygen impurity on the effective conversion rate of CD_4 molecules. We recall that at such temperatures C_R is proportional to the number of molecules that have converted over the time t_m. Thus the increase of C_R for the solution with 1% CD_4 upon the admixture to that solution of an oxygen impurity is due solely to the contribution of the CD_4 molecules in which conversion was stimulated by the magnetic field of the O_2 molecules. The probability of conversion of a CD_4 molecule decreases with increasing distance from it to the nearest oxygen molecule. We shall assume that over the measurement time t_m those CD_4 molecules found at a distance $r \leq r_{\text{eff},O_2}$ from the nearest oxygen molecule will have undergone conversion. We denote by N_{eff,O_2} the number of lattice sites within a sphere of radius r_{eff,O_2}. For a random distribution of oxygen molecules, the fraction of lattice sites around which there is not a single O_2 molecule in a volume containing N_{eff,O_2} sites is given by $(1 - n_{O_2})^{N_{\text{eff},O_2}}$. Then the fraction of CD_4 molecules from the case of the equilibrium distribution which convert over a time t_m as a consequence of the influence of oxygen will be

$$K_{O_2} = 1 - (1 - n_{O_2})^{N_{\text{eff},O_2}} \approx 1 - \exp(-n_{O_2} N_{\text{eff},O_2}), \qquad (3)$$

at low concentrations ($n_{O_2} \ll 1$) of the O_2 impurity. Hence

$$N_{\text{eff},O_2} = -\ln(1 - K_{O_2})/n_{O_2}. \qquad (4)$$

We note that if the conversion is brought about only as a consequence of the influence of the O_2 impurity, then $K' = K_{O_2}$. In cases when the conversion is due to some independent mechanisms, e.g., the hybrid (K_{hyb}) and impurity (K_{O_2}), then

$$K' = K_{\text{hyb}} + (1 - K_{\text{hyb}}) K_{O_2}. \qquad (5)$$

We recall that for the solution with 1% CD_4 at $T \sim 1$ K a value $K' = K_{\text{hyb}} \cong 0.1$ was found. For the solution with 1% CD_4 and 0.2% O_2 ($K' = 0.55$) we obtain with the use of expressions (4) and (5) the values $K_{O_2} \cong (0.55 - 0.1)/(1 - 0.1) = 0.5$ and $N_{\text{eff},O_2} \approx 350$. For an fcc lattice with lattice parameter $a = 3.6 \times 10^{-10}$ m this corresponds to a value $r_{\text{eff},O_2} = (3N_{\text{eff},O_2}/16\pi)^{1/3} a = 2.75a \sim 10^{-9}$ m. For $n_{O_2} \ll 1$ the value of N_{eff,O_2} depends weakly on n_{O_2}, and one can use the value obtained for N_{eff,O_2} to estimate K_{O_2} for different small concentrations of oxygen.

For the solution with 5% CD_4 a fraction $K' = 0.85$ of the CD_4 molecules from the case of the equilibrium distribution convert over a time $t_m = 44$ min (see Table II). The introduction of 0.2% O_2 to that solution leads to an increase in K' to 0.95, in satisfactory agreement with the estimate for this solution, $K' = 0.93$ (if it is assumed that $K_{O_2} = 0.503$ and $N_{\text{eff},O_2} = 350$).

The closeness of the experimental values of C_R to $C_{R,\text{eq}}$ in the solution with 5% CD_4 at $T < 1.4$ K is unexpected. According to the hybrid mechanism of conversion the rate of conversion of CD_4 molecules in clusters is substantially higher than for isolated molecules. For a random spatial distribution of impurities in the lattice the relative number of rapidly converting CD_4 molecules in the clusters is 46%. The contribution of these molecules to the heat capacity is substantially less than the values of $C_{R,\text{eq}}$. Let us mention some possible reasons for this discrepancy.

1. An appreciable contribution to the heat capacity C_R can be made by clusters formed by impurity molecules found a distance apart greater than the distance between nearest-neighbor CD_4 molecules, $a/2^{1/2}$, where a is the lattice constant.

2. It can be assumed that because of the energy benefit of forming small clusters, their concentration in the solution with 5% CD_4 may be substantial higher than for a random distribution of impurities. We note that because of the larger amplitude of the zero-point orientational vibrations of the CH_4 molecules the energy of interaction of impurity molecules and the energy benefit of forming cluster in methane–krypton solutions should be less.

Following Ref. 4, with the use of the K' values obtained (for the characteristics times of the experiment, t_m) we estimate the characteristic times τ for conversion between the lowest states of the A and T species of the CD_4 molecule in the investigated solutions for $T < 1.4$ K. The following expression was obtained in Ref. 4:

$$\tau = -t_m / \ln(1 - K'). \qquad (6)$$

The conversion rate depends on the mutual position of the CD_4 molecules and the distribution of the paramagnetic O_2 impurity molecules. Therefore, τ in expression (6) is a unified average conversion time.

As we have said, for a solution with 1% CD_4 in Kr without an O_2 impurity at $T > 1$ K the value of K' is strongly temperature dependent. This means that the conversion of matrix-isolated CD_4 molecules (the fraction of which is 89%) is due to a new mechanism and depends strongly on
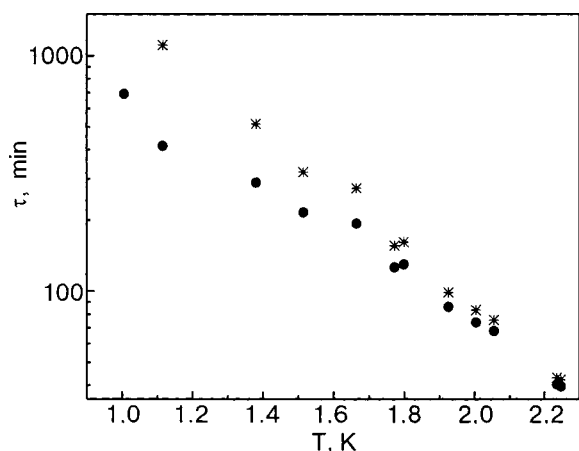
FIG. 4. Temperature dependence of the effective characteristic conversion times τ ($\bullet$) and τ_T (*) for the solution $(CD_4)_{0.01}Kr_{0.99}$.

temperature. The characteristic of the temperature dependence of τ for this solution in the interval $T=1-2$ K can be determined (formally) with the use of Eq. (6). Such an estimate is possible because for $T \leqslant 2$ K the contribution to the heat capacity C_R from energy levels lying above the level with $J=1$ is less than 10%. If we assume that all the conversion mechanisms are independent, then $K' = K_c + (1 - K_c)K_T$, where K_c is determined by the contributions to the conversion from all temperature-independent mechanisms and K_T is the contribution to the conversion from the mechanism causing the temperature dependence of the conversion rate. Since $K_c = K_{hyb} = 0.1$ for the solution with 1% CD_4 in Kr, one has $K'_1 = C_{R_1}/C_{R,eq} = 0.1 + 0.9K_T$, where C_{R_1} are the normalized experimental values of the rotational heat capacity of this solution. For the solution with 1% CD_4 and 0.2% O_2 in Kr, we have $K_c = K_{hyb} + (1 - K_{hyb})K_{O_2} = 0.55$ and $K'_2 = C_{R_2}/C_{R,eq} = 0.55 + 0.45K_T$, where C_{R_2} are the normalized experimental values of the rotational heat capacity of the solution with 1% CD_4 and 0.2% O_2. By equating $C_{R,eq}$ from the expressions for K'_1 and K'_2, we determined $K'_T = (0.55C_{R_1} - 0.1C_{R_2})/(0.9C_{R_2} - 0.45C_{R_1})$. The temperature dependence of τ and τ_T calculated with the use of K' and K'_T for the times t_m according to Eq. (6) is shown in Fig. 4. It is seen that in the case of the solution with 1% CD_4 in Kr the effective characteristic conversion time τ_T decreases rapidly with increasing temperature in the interval 1–2 K. At temperatures of around 1 K the hybrid mechanism of conversion is dominant, and the rate of conversion of isolated CD_4 molecules is substantially lower than the rate of conversion in clusters of CD_4 molecules ($\tau < \tau_T$). For $T > 2$ K ($\tau \approx \tau_T$) a new mechanism of conversion, causing its temperature dependence, becomes dominant.

The values of τ calculated according to Eq. (6) in the temperature region below 1.4 K for the other solutions studied are given in Table II along with the data of Ref. 4 for solutions with different concentrations of methane and of methane and oxygen in krypton.

In the solutions with 5% CD_4 and CH_4 in Kr the average conversion rate of the CD_4 molecules is 6 times higher than for the CH_4 molecule (see Table II). This is an important and unexpected result.

We have shown above that in CD_4–Kr solutions at T

<1.4 K the hybrid mechanism of conversion is dominant.[7] According to the theory,[7] the conversion rate is governed by the intramolecular magnetic interaction between nuclei of the light atoms of the molecules and the intermolecular effective octupole–octupole interaction between rotors in the lattice. The intramolecular magnetic interaction between deuterons is significantly smaller than that between protons, since the magnetic moment of the deuteron $\mu_D = 0.306\mu_H$. We note that in CD_4–Kr solutions conversion can also be brought about as a consequence of the relatively small magnetic quadrupole–quadrupole interaction between deuterons.[21,22] On the whole, the intramolecular magnetic interaction between deuterons is smaller than that between protons. This should lead to a decrease of the conversion rate. However, the role of factors which accelerate the conversion of deuteromethane molecules must also be taken into account. Because of the smaller amplitude of the zero-point orientational vibrations and the larger effective electric octupole moment in the ground state, the noncentral interaction of the CD_4 molecules with rare gas atoms and other CD_4 impurity molecules is larger than the analogous interaction of the more quantum molecules CH_4. This, in particular, should enhance the effective octupole–octupole interaction of the CD_4 molecules in the clusters and increase the probability of transfer of the conversion energy to the crystal lattice. Thus the higher conversion rate of the CD_4 molecules as compared to CH_4 molecules in dilute solid solutions of deuteromethane and methane in krypton at low temperatures means that the "bottleneck" governing the conversion rate is the intermolecular octupole–octupole interaction and the related probability of transfer of the conversion energy to the phonons.

In solutions with 1% CD_4 and CH_4 doped with 0.2% O_2 the effective conversion rate of the CD_4 molecules is smaller by a factor of 3.5 than for the CH_4 molecule (see Table II). At the same time, it was shown above that in solutions with 5% CD_4 or CH_4 the conversion rate of the CD_4 molecules, due to the hybrid mechanism, is noticeably larger than the conversion rate of CH_4 molecules. The conversion rate of isolated rotors in these solutions with an added oxygen impurity is determined by the intermolecular magnetic interaction between the deuterons of the CD_4 molecules (or the protons of the CH_4 molecules) and the electronic magnetic moment of the O_2 molecules. Since the magnetic moment of the deuteron is smaller by a factor of three than that of the proton, the magnetic interaction between CD_4 and O_2 molecules is substantially smaller than that between CH_4 and O_2, and the influence of the oxygen molecules on the conversion of CH_4 molecules is stronger.

We have mentioned above that in the ground state the noncentral interaction of the CD_4 molecules with the rare gas atoms and other CD_4 impurity molecules is larger than the analogous interaction of the more quantum CH_4 molecules. This, in particular, should lead to a larger dilatation of the lattice near the CD_4 molecules and larger changes in the energy spectra of rotors in clusters of CD_4 molecules. Therefore, orientational octupole glasses should form at lower concentrations of CD_4 molecules and higher temperatures in the CD_4–Kr solutions than in the analogous case of solutions containing CH_4. We are planning to do low-temperature calorimetric studies of $(CD_4)_nKr_{1-n}$ solid solutions with

larger deuteromethane concentrations in the future, with the goal of finding and investigating octupole glasses.

CONCLUSION

Solid solutions of methane isotopes (CH_4 and CD_4) in krypton are convenient for studying the low-temperature dynamics of an ensemble of spherical rotors with different rotational quantum parameters[1] in the crystalline field. Quantum effects in the behavior of the subsystem of rotors are dominant at temperatures below 2 K, when as a consequence of conversion the physical properties of the rotational subsystem are determined mainly by transitions between the lowest levels of the nuclear spin A and T species of the rotors with different energies ε_{AT}. The main goal of the present study was to conduct a calorimetric investigation of the nuclear spin conversion of deuteromethane molecules in $CD_4 - Kr$ solid solutions. The information obtained in these studies about the heat capacity and the low-energy part of the rotational spectrum of $CD_4 - Kr$ solutions is of independent interest.

In the present paper and in our previous paper[8] we have measured the heat capacity of solid solutions with 1% and 5% CD_4 and of these same solutions doped with 0.2% O_2, in the temperature region 0.7–20 K. The contribution C_R of the rotational subsystem to the heat capacity of the solutions was separated out. We have investigated the influence of temperature and of oxygen impurities and clusters of deuteromethane molecules on the effective conversion rate.

The main results of this study are as follows.

1. Strong heat release is observed as the solid solutions of CD_4 in Kr are cooled at low temperatures, attesting to nuclear spin conversion of the CD_4 molecules.

2. The heat capacity C_R of the rotational subsystem in solutions with 5% CD_4 in Kr at $T < 1.5$ K is close to equilibrium and is more than an order of magnitude greater than the heat capacity calculated under the assumption that conversion is absent. This is also an argument in favor of a manifestation of the conversion of CD_4 molecules.

3. At low temperatures (~ 1 K) in the binary solutions Kr–CD_4, as in the Kr–CH_4 solutions,[3,4] the hybrid mechanism of conversion is dominant.[7] This is indicated by the strong concentration dependence of the heat capacity C_R in the binary solutions Kr–CD_4.

4. It has been found that the rate of conversion of CD_4 molecules in solid Kr is larger than for CH_4 molecules. This effect is explained by the larger noncentral interaction of the CD_4 molecules in the ground state with other CD_4 molecules and with Kr atoms and, accordingly, the higher probability of transfer of the conversion energy to phonons.

5. We have estimated the effective characteristic conversion time τ of CD_4 molecules isolated in the Kr lattice for conversion stimulated by the paramagnetic impurity oxygen.

The rate of such conversion of CD_4 molecules is noticeably smaller than for CH_4 molecules, since the magnetic moment of the deuteron is less than the magnetic moment of the proton.

6. We have determined the energy differences ε_{AT} of the lowest levels of the nuclear spin A and T species of deuteromethane.

*E-mail: bagatskii@ilt.kharkov.ua

[1] V. G. Manzhelii and Yu. A. Freiman (eds.), *Physics of Cryocrystals*, AIP, Woodbury, New York (1997).

[2] V. G. Manzhelii, A. I. Prokhvatilov, I. Ya. Minchina, and L. D. Yantsevich, *Handbook of Binary Solutions of Cryocrystals*, Begell House, New York, Wallingford, U.K. (1996).

[3] I. Ya. Minchina, V. G. Manzhelii, M. I. Bagatskii, O. V. Sklyar, D. A. Mashchenko, and M. A. Pokhodenko, Fiz. Nizk. Temp. **27**, 773 (2001) [Low Temp. Phys. **27**, 568 (2001)].

[4] M. I. Bagatskii, V. G. Manzhelii, I. Ya. Minchina, D. A. Mashchenko, and I. A. Gospodarev, J. Low Temp. Phys. **130**, 459 (2003).

[5] W. Press, *Single-Particle Rotations in Molecular Crystals*, Vol. 92 of Springer Tracts in Modern Physics, Springer-Verlag, Berlin, Heidelberg, New York (1981).

[6] V. G. Manzhelii, A. I. Prokhvatilov, V. G. Gavrilko, and A. P. Isakina, *Structure and Thermodynamic Properties of Cryocrystals*, Handbook, Begell House, New York, Wallingford, U.K. (1998).

[7] A. J. Nijman and A. J. Berlinsky, Can. J. Phys. **58**, 1049 (1980).

[8] M. I. Bagatskii, V. G. Manzhelii, D. A. Mashchenko, and V. V. Dudkin, Fiz. Nizk. Temp. **29**, 216 (2003) [Low Temp. Phys. **29**, 159 (2003)].

[9] M. A. White and J. A. Morrison, J. Chem. Phys. **72**, 5927 (1980).

[10] M. I. Bagatskii, I. Ya. Minchina, and V. G. Manzhelii, Fiz. Nizk. Temp. **10**, 1039 (1984) [Low Temp. Phys. **10**, 542 (1984)].

[11] V. I. Peresada, Zh. Éksp. Teor. Fiz. **53**, 605 (1967) [Sov. Phys. JETP **26**, 389 (1968)].

[12] V. I. Peresada and V. P. Tolstoluzhskii, Fiz. Nizk. Temp. **3** 378 (1977) [Low Temp. Phys. **3**, 383 (1977)].

[13] R. H. Beaumont, H. Chihara, and J. A. Morrison, Proc. Phys. Soc. London **78**, 1462 (1961).

[14] L. Finegold and N. E. Phillips, Phys. Rev. **177**, 1383 (1969).

[15] P. I. Muromtsev, M. I. Bagatskii, V. G. Manzhelii, and I. Ya. Minchina, Fiz. Nizk. Temp. **20**, 247 (1994) [Low Temp. Phys. **20**, 195 (1994)].

[16] K. Nishiyama, J. Chem. Phys. **56**, 5096 (1972).

[17] E. B. Wilson, J. Chem. Phys. **3**, 276 (1935).

[18] S. Grieger, H. Friedrich, B. Asmussen, K. Guckelsberger, D. Nettling, W. Press, and R. Scherm, Z. Phys. Condens. Matter B **89**, 203 (1992).

[19] P. Hopkins, P. Z. Donoho, and K. S. Pitzer, J. Chem. Phys. **47**, 864 (1967).

[20] B. Asmussen, D. Balszunat, W. Press, M. Prager, C. J. Carlile, and H. Buttner, Physica B **202**, 224 (1994).

[21] M. A. Strzhemechnyĭ and O. I. Tokar', Fiz. Nizk. Temp. **11**, 813 (1985) [Sov. J. Low Temp. Phys. **11**, 446 (1985)].

[22] K. Motizuki, J. Phys. Soc. Jpn. **12**, 163 (1957).

Translated by Steve Torstveit

SHORT NOTES

Influence of a boron oxide admixture on the magnetic and electrical properties of the high-T_c superconductor Bi$_{1.7}$Pb$_{0.3}$Sr$_2$Ca$_2$Cu$_4$O$_y$

V. V. Jgamadze, R. G. Kokhreidze, N. G. Margiani, A. N. Mestvirishvili, S. V. Odenov, N. A. Papunashvili, G. A. Tsintsadze,[†] and G. A. Shurgaia

*Institute of Cybernetics of the Academy of Sciences of Georgia, ul. S. Éuli 5, 380086 Tbilisi, Georgia**

The influence of an admixture of boron oxide B$_2$O$_3$ on the magnetic and electrical properties of a high-T_c superconducting ceramic with the nominal composition Bi$_{1.7}$Pb$_{0.3}$Sr$_2$Ca$_2$Cu$_4$O$_y$ is investigated. A nonmonotonic dependence of the critical temperature T_c ($\rho = 0$) and magnetic susceptibility on the boron concentration is found. © *2003 American Institute of Physics.*
[DOI: 10.1063/1.1630722]

The influence of admixtures and substitutions of different elements on the magnetic and electrical properties of bismuth-containing high-T_c superconductors (HTSCs) has long been a subject of research.[1,2] Nevertheless, no systematic study of the influence of a boron oxide admixture on the phase formation processes and superconducting properties of HTSC materials of the system Bi–Pb–Sr–Ca–Cu–O has yet been done. An element with a small ionic radius, such as boron, can be introduced into a HTSC of the Bi system in the form of an admixture and not at as an element substituting for a structure component.

Below we present some preliminary results of a study of the magnetic and electrical properties of boron-oxide doped ceramic samples with the nominal composition Bi$_{1.7}$Pb$_{0.3}$Sr$_2$Ca$_2$Cu$_4$B$_x$O$_y$, where $x = 0, 0.1, 0.3, 0.5, 0.7$, and 1.0. The samples were synthesized in a medium of air by the standard solid-phase technology from oxides and carbonates of the corresponding elements. The powder was heat treated for 30 hours at 850 °C. The tabletized samples were heat treated for 10 hours at 840 °C. Boron oxide was added not only to the initial stock but to the superconductor powders obtained in the course of the solid-phase reaction. The results of the study were quite similar for both variants, and so we shall present the results of the measurements only for the first.

The temperature dependence of the magnetic susceptibility $\chi(T)$ of the synthesized samples was studied in a field-cooling regime (in a magnetic field $H = 10$ Oe), and the temperature of the start of the superconducting transition T_{cm} was determined from the magnetic measurements. The temperature dependence of the resistivity $\rho(T)$ was measured by a four-contact method. The dependence of the magnetic susceptibility on the field and on the amount of boron in the samples was measured at 77 K in magnetic fields from 0 to 3 kOe. An x-ray phase analysis (XPA) of the samples was done on a DRON-1.5 diffractometer (CuK_α radiation).

Figure 1 shows the temperature dependence of $\chi(T)$ for samples of the concentration series Bi$_{1.7}$Pb$_{0.3}$Sr$_2$Ca$_2$Cu$_4$B$_x$O$_y$ ($x = 0–1$). On all the curves except that for the sample with $x = 1$ a two-step transition is observed, indicating the presence of two superconducting phases in the samples: 2223 ($T_c = 110$ K) and 2212 ($T_c = 80$ K). It is seen in Fig. 1 that the relative contribution of the 2223 phase decreases with increasing boron content, and that of the 2212 phase increases in the region $x = 0.1–0.7$. The start of the high-temperature superconducting transition with $T_{cm1} = 107$ K, corresponding to the 2223 phase, remains unchanged over the entire range of boron concentrations in the samples ($x = 0–1$). The temperature of the start of the low-temperature superconducting transition T_{cm2}, determined as the point of the kink, is due to the 2212 phase. The dependence of T_{cm1} and T_{cm2} on the boron concentration in the samples is described by curves *1* and *2*, respectively, in Fig. 2. It is seen that T_{cm2} depends on the boron concentration in a nonmonotonic way and has a plateau in the interval $x = 0.3–0.7$. For the sample with boron concentration $x = 1$ the fall of the magnetic susceptibility due to the presence of the 2212 phase is not observed.

The $\rho(T)$ curves of the samples correspond to a metallic type of conductivity. Here the resistivity in the normal state $\rho(300$ K) is practically independent of the boron concentration in the samples and corresponds to a value 3–4 mΩ·cm.

The dependence of the temperature of the end of the superconducting transition $T_c(\rho = 0)$ on the boron concentration is given by curve *3* in Fig. 2. It is seen that a B$_2$O$_3$ admixture lowers $T_c(\rho = 0)$ in a nonmonotonic way. A weak maximum of $T_c(\rho = 0)$ of the doped samples is observed at $x = 0.5$, and as the boron concentration is increased further to $x = 1$ the value of $T_c(\rho = 0)$ falls sharply to 75 K. From the dependence on the boron concentration of the low-frequency susceptibility χ measured in a static magnetic field $H = 2.5$ kOe (curve *4* in Fig. 2), we see that it initially declines slightly (at $x = 0.1$) and then even increases to a maximum at $x = 0.5$. A sharp decrease of χ is observed when the the boron concentration is increased to $x = 1$. A comparative x-ray phase analysis of the Bi$_{1.7}$Pb$_{0.3}$Sr$_2$Ca$_2$Cu$_4$B$_x$O$_y$ samples with $x = 0, 0.5$, and 1.0 confirmed the presence of two superconducting phases in the samples: 2223 and 2212. As a result of
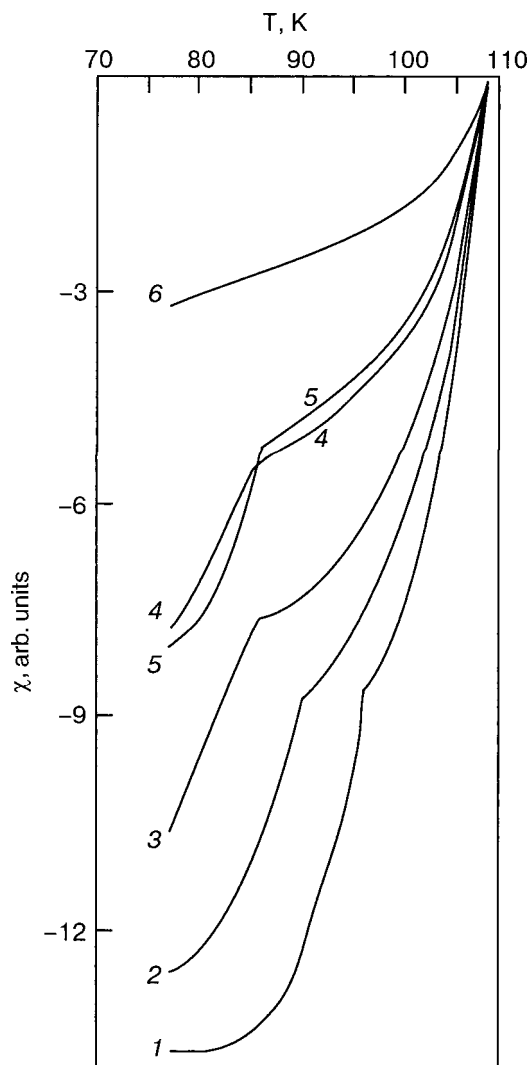
FIG. 1. Temperature dependence of the magnetic susceptibility χ for $Bi_{1.7}Pb_{0.3}Sr_2Ca_2Cu_4B_xO_y$ samples with different x: 0 (*1*), 0.1 (*2*), 0.3 (*3*), 0.5 (*4*), 0.7 (*5*), 1.0 (*6*).

FIG. 2. Concentration dependence of the superconducting properties of $Bi_{1.7}Pb_{0.3}Sr_2Ca_2Cu_4B_xO_y$ samples: the start of the superconducting transition T_{cm1}, corresponding to the phase 2223 (*1*); the start of the superconducting transition T_{cm2} corresponding to the 2212 phase (*2*); the end of the superconducting transition $T_c(\rho=0)$ (*3*); the magnetic susceptibility at $H=2.5$ kOe (*4*).

the admixture of B_2O_3 to the initial stock at the $x=0.5$ level, the relative contribution of the 2223 phase decreases and that of the 2212 phase increases. The XPA was unable to reveal any auxiliary phases associated with the boron.

Thus the preliminary data presented in this paper on the influence of a B_2O_3 admixture on the magnetic and electrical properties of HTSC ceramics attest to nonmonotonic dependence on the boron concentration for the zero-resistance temperature $T_c(\rho=0)$, for the temperature of the start of the superconducting transition from the magnetic measurements, T_{cm2}, which is associated with the 2212 phase, and for the magnetic susceptibility χ. In the concentration series of samples in the interval of boron concentrations $x=0.3-0.7$ one observes growth of $T_c(\rho=0)$ and χ and a constant value of T_{cm2}. Further increase in the boron concentration to $x=1$ leads to a sharp decrease in the superconducting volume fraction in the sample and a decrease in $T_c(\rho=0)$ and χ. Here the transition corresponding to the 2212 phase is not manifested in the magnetic measurements. The start of the superconducting transition associated with the 2223 phase and the resistivity of the samples in the normal state are independent of the boron concentration. The data presented
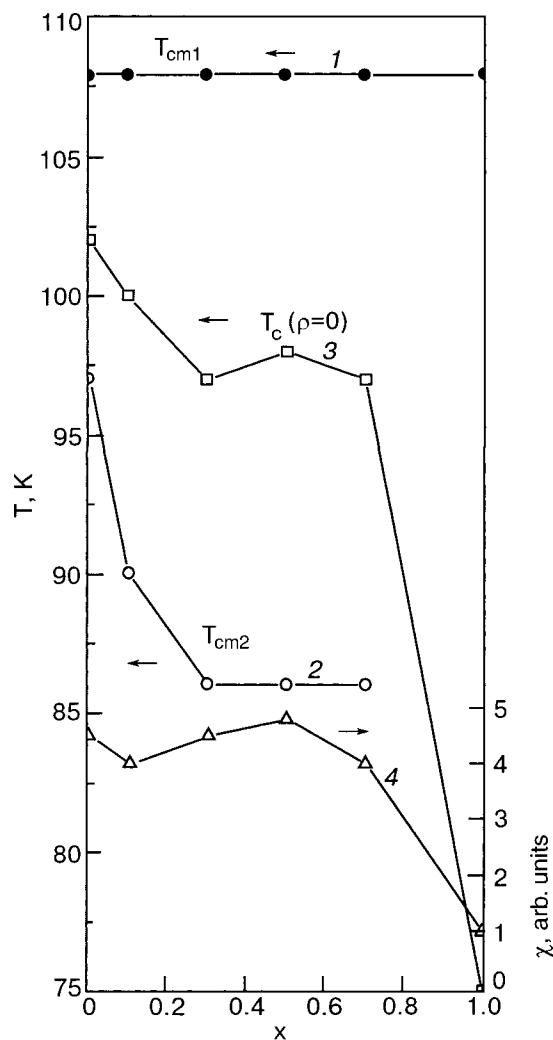
here do not yet permit drawing definitive conclusions about the structural role of boron in the synthesized samples. Because of their small ionic radius, boron ions can enter interstitial sites of the lattice, where they primarily affect the concentration of carriers (holes). On the other hand, boron in an auxiliary phase can alter the microstructure of Bi-containing ceramics, and that could influence the character of the intergrain contacts and the critical current. The question of the structural role of boron in a Bi-containing superconducting system is a subject for further research.

†Deceased.
*E-mail: vakhtang7@rambler.ru

[1] D. M. Ginzberg (ed.), *Physical Properties of High-Temperature Superconductors* [in Russian], Mir, Moscow (1990).
[2] Yu. D. Tret'yakov and E. A. Gudilin, Usp. Khim. **69**, 3 (2000).
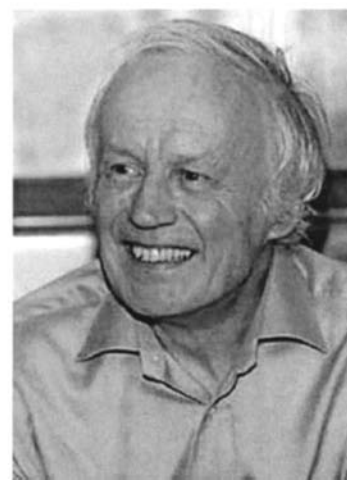
Translated by Steve Torstveit

Nobel Prize of 2003 awarded for "Pioneering contributions to the theory of superconductors and superfluids"

V. L. Ginzburg

A. A. Abrikosov

A. J. Leggett

The fact that the Nobel Prize has again been awarded for work in low-temperature physics should lend authority to low-temperature research in the physics of today. The Nobel Laureates in physics for 2003 are the Russian Academicians Alexei A. Abrikosov and Vitaly L. Ginzburg and the Englishman Anthony J. Leggett. The announcement by the Nobel Committee stated that the prize was awarded to three scientists who had made an outstanding contribution to our understanding of two phenomena of quantum physics—superconductivity and superfluidity. All three winners worked fruitfully on the problems of superconductivity and superfluidity over a period of several decades. In addition to extremely important original work, each is the author of a number of monographs and review articles that are used in thousands of research studies. Abrikosov, Ginzburg, and Leggett are members of academies of sciences and prominent physical societies of a number of countries, and each has repeatedly won prestigeous awards. The fact that this year's Nobel Prize was awarded for "pioneering" work is a confirmation of the fundamental character of their discoveries, each of which led to new fields of physics research and to a multitude of technical applications. It gives us pleasure to point out that one of the laureates, Academician V. L. Ginzburg, served as a member of the Editorial Board of the journal *Low Temperature Physics* from 1975 to 1991. The staff of *Low Temperature Physics* congratulates the new Nobel Laureates and warmly wishes them good health and continued creativity.

A BRIEF CHRONOLOGICAL ACCOUNT OF THEIR PIONEERING WORK

In 1950 Ginzburg and L. D. Landau created a phenomenological theory of superconductivity. They wrote the famous Ginzburg–Landau equations for the order parameter on the basis of the theory of second-order phase transitions with allowance for inhomogeneities created by magnetic fields. The theory made a number of important predictions, later confirmed experimentally, about the critical values of the magnetic fields and current in thin-film superconductors. The Ginzburg–Landau theory has since proved to be of significant value in many fields of physics, including particle physics. This theory is widely used today for describing the properties of superconductors in practical applications, e.g., at high magnetic fields or when fluctuations of the order parameter in time are taken into account.

In 1953, on the basis of Ginzburg–Landau theory with anisotropy taken into account, Abrikosov put forth the idea of type-II superconductors. He constructed a theory of the magnetic properties of superconducting alloys, introduced the concept of two critical fields and a "mixed" state with a vortical structure of the currents—"Abrikosov vortices." Without Abrikosov vortices the modern physics of superconductivity, including the applied side, would be inconceivable. Later Abrikosov and L. P. Gor'kov developed a theory of superconductors containing magnetic impurities and predicted the phenomenon of gapless superconductivity. After the discovery of high-T_c superconductors, which have a pronounced type-II superconductivity, Abrikosov's theory has

been widely used in research on these materials and in the development of new technologies.

In 1972 Leggett constructed a theory of an anisotropic superfluid which has sharply different properties from those of isotropic superfluid systems—superfluid ^{4}He and ordinary superconductors. Leggett's general theory of spin dynamics of an anisotropic superfluid Fermi liquid has played a dominant role in the identification of the phases of superfluid ^{3}He. It has explained the unexpected results of NMR experiments in superfluid ^{3}He and has made it possible to determine the quantum states of the A and B phases and the structure of the order parameter of these phases. Leggett showed that the appearance of anomalous low-temperature phases of liquid ^{3}He is due to the breaking of spin–orbit symmetry. His discovery that in the condensed state, several forms of symmetry can be broken simultaneously is very important for understanding the complex phases in other systems as well, e.g., in liquid crystals, particle physics, and cosmology.

Editorial Board

SUPERCONDUCTIVITY, INCLUDING HIGH-TEMPERATURE SUPERCONDUCTIVITY

Fluctuation conductivity and critical currents in YBCO films

A. L. Solovjov,* V. N. Svetlov, and V. B. Stepanov

B. Verkin Institute for Low Temperature Physics and Engineering, National Academy of Sciences of Ukraine, pr. Lenina 47, 61103 Kharkov, Ukraine

V. M. Dmitriev

B. Verkin Institute for Low Temperature Physics and Engineering, National Academy of Sciences of Ukraine, pr. Lenina 47, 61103 Kharkov, Ukraine; International Laboratory of High Magnetic Fields and Low Temperatures, 53-421 Wroclaw, Poland

A comparative analysis of the results obtained in measurements of the fluctuation conductivity and of the critical current density $j_c(T)$ in $YBa_2Cu_3O_{7-y}$ films containing various numbers of defects is carried out for the first time. It is found that the value and temperature dependence of the fluctuation conductivity are interrelated with the values and temperature dependences of the critical current and resistivity of the samples. It follows from measurements of the fluctuation conductivity that the variation of these temperature dependences is directly related to the variation of the number of defects and, hence, the number of pinning centers in the films studied. It is shown that in films containing practically no defects the $j_c(T)$ curve completely follows a model giving $j_c(T)$ in high-T_c superconductors with low-angle grain boundaries between crystallization blocks. On the other hand, if the sample has a specific defect structure that is formed under certain conditions in c-oriented epitaxial high-T_c superconducting films, one observes a sharp increase in j_c and in the slope of the $j_c(T)$ curve. © *2003 American Institute of Physics.* [DOI: 10.1063/1.1630712]

INTRODUCTION

The mechanism for the scattering of normal carriers in high-T_c superconductors (HTSCs), like the mechanism for superconducting pairing in them, is still not completely clear. Moreover, the minimum of the differential conductance dI/dV at zero bias observed in tunnel experiments, which is due to the decrease in the density of states in the superconductor at $T < T_c$, is also observed in HTSCs at $T \gg T_c$ (Ref. 1), where T_c is the temperature of the superconducting transition of the sample. From this result it has been conjectured in a number of papers that with increasing temperature the superconducting gap $\Delta(T)$ does not decrease to zero at $T = T_c$ but retains a finite value even at $T \gg T_c$ (Ref. 1). This effect, which has come to be called the pseudogap, has been observed by all the known experimental methods in many HTSC systems.[1] A review of the existing theories of the pseudogap is given in Ref. 1; the conclusions of the theories, like the experimental results, are extremely contradictory. However, the idea that the pseudogap arises as a result of the formation of fluctuating Cooper pairs at $T \gg T_c$ has gradually come to prevail.[1–5] At present the possibility of fluctuation pairing in HTSCs at temperatures much higher than T_c is widely discussed in the literature.[4–10] At the same time, the dynamics of quasiparticles in HTSCs at $T \ll T_c$ is also extremely peculiar.[11,12] To elucidate the possible connection between the pseudogap and the quasiparticle dynamics in HTSCs, one must study the various properties of the same sample both in the pseudogap regime and below T_c. With this goal we have studied the fluctuation conductivity and critical currents of c-oriented epitaxial films of $YBa_2Cu_3O_{7-y}$ (YBCO).

One of the manifestations of the pseudogap in HTSCs is anomalous temperature dependence of the longitudinal resistivity $\rho_{xx}(T)$. It is well known[13–15] that $\rho_{xx}(T)$ in YBCO systems at $T \gg T_c$ is proportional to T over a wide range of temperatures. However, when the temperature is lowered, $\rho_{xx}(T)$ ultimately deviates downward from a linear dependence at a certain characteristic temperature $T_{*0} \gg T_c$, giving rise to an excess conductivity

$$\sigma'(T) = \sigma(T) - \sigma_N(T), \text{ or}$$

$$\sigma'(T) = [\rho_N(T) - \rho(T)]/[\rho_N(T)\rho(T)]. \tag{1}$$

Here $\rho(T) = \rho_{xx}(T)$ is the measured resistivity, and $\rho_N(T) = \alpha T + b$ is the normal-state resistivity of the sample extrapolated to the low-temperature region. The linear temperature dependence of the resistivity of HTSCs can be explained in the "nearly antiferromagnetic Fermi liquid" (NAFL) model,[15] which also explains the anomalous temperature dependence of the Hall coefficient, $R_H \sim 1/T$. According to the NAFL model, the linear dependence of $\rho_{xx}(T)$ at high temperatures can be considered to be a reliable sign of the normal state of the system, which is characterized by stability of the Fermi surface and, consequently, stability of the normal-carrier scattering intensity.

Usually the excess conductivity is interpreted as the fluctuation conductivity (FC)[17] predicted by the Aslamazov–Larkin theory,[16] and it is standard practice to use Eq. (1) to calculate $\sigma'(T)$ from experiment.[17–23] It has been shown[17,23] that such a practice is justified for an optimally doped YBCO system, at least in the temperature interval $T_c < T < T_{c0} = 105 \pm 5$ K, where T_{c0} is the maximum temperature to which the data follow fluctuation theory. Studying the FC yields information about the scattering and superconducting pairing mechanisms as the temperature approaches T_c. The question of whether the excess conductivity in HTSCs at $T > T_{c0}$ can be interpreted entirely as fluctuation conductivity is the subject of further research by the authors and is beyond the scope of the present paper.

An important characteristic of HTSCs in the superconducting state is the current-carrying capacity or critical current density j_c. It has been shown in a number of papers[1,24–29] that this property is largely determined by the presence of various structural distortions in the sample which act as effective pinning centers[26] because of the exceptionally short coherence length $\xi(0)$ in HTSCs.[24] The presence of defects and the nature of the contacts between them will determine both the value and the temperature dependence of j_c (Refs. 25–29). While there have been quite a few studies devoted to the investigation of the critical currents in HTSCs (see, e.g., the reviews[28,29]), the number of theoretical models that have been considered in detail (e.g., in Ref. 27) is relatively small. According to those models, the experimentally measured temperature dependence of the critical current density of a HTSC can be written in the form $j_c(T) = j_c(0)(1 - T/T_c)^s$, where $j_c(0)$ is the maximum value of the critical current density obtained by extrapolation of the experimental data to $T = 0$, and the exponent s is determined by the type of disorder responsible for the pinning of isolated Abrikosov vortices on structural defects in the sample. For example, at temperatures sufficiently close to T_c, for pinning due to spatial variations of T_c (δT pinning) the theory gives $s = 7/6$, while for pinning due to variations of the mean free path of the charge carriers (δl pinning), $s = 5/2$.[28]

Depinning of Abrikosov vortices in HTSC films[28] is one of the factors decreasing j_c in comparison with its maximum possible value, which corresponds to a pair-breaking current density $j_0 = c\varphi_0/(12\sqrt{3}\pi^2\lambda_L^2\xi)$, where $\varphi_0 = hc/2e$ is the magnetic flux quantum, λ_L is the London penetration depth of the magnetic field, and ξ is the coherence length in the superconductor. At the same time, the critical currents in YBCO films are at least an order of magnitude higher than in the analogous single crystals[26] and much higher than in polycrystalline HTSCs. This is most likely due to the specifics of the structural defects of the crystal lattice in films as compared to single crystals,[26,30] whereas in polycrystalline HTSCs $j_c(T)$ is limited by the presence of intergrain Josephson contacts of various types. In the latter case the value of j_c is exceptionally low,[24–29] and the temperature dependence of $j_c(T)$ is governed by that of the Josephson current $j_m(T)$ flowing through the contacts. For example, dependences of the form $j_m(T) \propto j_c(0)(1 - T/T_c)$ and $j_m(T) \propto j_c(0) \times (1 - T/T_c)^2$ are calculated in the framework of Ginzburg–Landau theory for contacts of the superconductor–insulator–superconductor (SIS) and superconductor–normal metal–

superconductor (SNS) types, respectively.[25,31,32] For a complex contact of the superconductor–normal metal–insulator–superconductor (SNIS) type a dependence $j_m(T) \propto j_c(0)(1 - T/T_c)^{3/2}$ was obtained,[32] which is analogous to the temperature dependence of the pair-breaking current j_0. However, despite the considerable number of papers devoted to the study of j_c in HTSCs, it remains difficult to answer the question of how $j_c(T)$ should behave in modern YBCO epitaxial films prepared by pulsed laser deposition,[33] in which defects form in a very specific manner.[3,26] In addition, in our view there is a clear lack of systematic research on the simultaneous influence of defects on j_c and on the properties of the sample for $T > T_c$.

1. SAMPLES AND EXPERIMENTAL RESULTS

The films were prepared by pulsed laser deposition on $SrTiO_3(100)$ substrates.[34] This method[33] ensures a reproducible growth of c-oriented epitaxial films of YBCO, as was monitored from the x-ray spectra. It is known[26,33] that the defects arising in pulsed-laser-deposited YBCO films are formed mainly as a result of a possible deviation of the plane of the substrate from the crystallographic direction $SrTiO_3(001)$ during the film growth. Obviously, the larger the angle of deviation ϑ, the greater the number of defects. As was shown in Ref. 26, the deposition of films on $SrTiO_3$ substrates specially cut with a deviation $\vartheta = 10°$ in the [010] direction (we shall call these "films with defects") leads to the appearance of numerous defects of various types, which penetrate through the entire thickness of the film. These are primarily translational boundaries, multiple disruptions of the order of alternation of the CuO_2 conducting layers, which lead to distortion of the dimensions of the unit cell, and so-called extended defects with a structure 20–30 Å wide. All defects, especially translational boundaries, are effective pinning centers. It has been found that a large fraction of the defects in such films are aligned along a direction parallel to one of the boundaries of the film. Such a one-dimensional structure of the defects is responsible for the strong anisotropy of the resistivity, critical current, magnetic flux penetration,[26] and FC[3] observed in such films, depending on whether the measurements are made along the defects or perpendicular to them. In particular, the FC measured in the direction perpendicular to the defects has an extremely peculiar temperature dependence.[3]

Figure 1 shows the temperature dependence of the resistivity ρ_{xx} of samples W136 ($T_c \approx 86.1$ K) and W154 ($T_c \approx 88.2$ K). The resistive measurements were made by the standard 4-probe scheme. The parameters of the samples are given in Table I, where d_0 is the film thickness. We note that in the analysis of the FC the value of T_c was determined by extrapolation of the resistive transition to its intercept with the temperature axis. This approach gives higher values of T_c than extrapolation of $j_c(T)$ to zero; this circumstance is reflected in the Table I. Both films are close to optimally doped (OD) YBCO systems, as is confirmed by the high values of T_c, but they contain different numbers of defects. As can be seen in Fig. 1, W136 exhibits resistive behavior similar to that observed in well-structured OD YBCO films, namely: the dependence of $\rho_{xx}(T)$ is linear above $T_{*0} = 160 \pm 2$ K and is described well in the temperature region 160–300 K
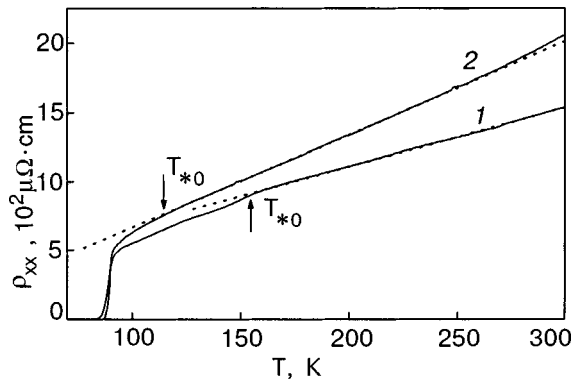
FIG. 1. Temperature dependence of the resistivity of samples W136 (*1*) and W154 (*2*); the dashed line shows the extrapolation of the resistivity in the normal states to the low-temperature region; the arrows indicate the temperatures T_{*0} for each sample.
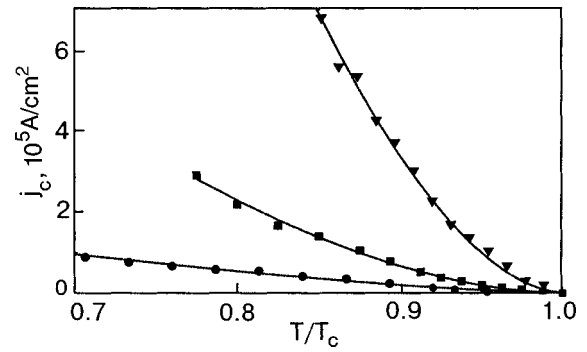

FIG. 2. Temperature dependence of the critical current densities for samples W62 (●), W136 (■), and W154 (▲); the solid curves show the calculation according to the equation $j_c(T) = j_c(0)(1 - T/T_c)^s$ with the parameters $j_c(0)$ and s designated in the text.

by an expression of the form $\rho_N(T) = \alpha T + b$ (dashed line in Fig. 1). In accordance with the ideas of the NAFL theory, this field dependence, extrapolated into the low-temperature region, gives the values of $\rho_N(T)$ used for calculating $\sigma'(T)$ from Eq. (1). It should be stressed, however, that both $\rho_{xx}(100 \text{ K})$ and $d\rho/dT$ measured in experiment are considerably larger than the values $\rho_{xx}(100 \text{ K}) \approx 150 \ \mu\Omega \cdot \text{cm}$ and $d\rho/dT \approx 0.5 \ \mu\Omega \cdot \text{cm/K}$ typical for YBCO films not containing defects.[17,20–22] This result, together with the extremely high critical current density and certain features of the temperature dependence of the FC, considered below, is an indication that the sample does contain some defects. This means that the angle of deviation ϑ of the substrate from the direction SrTiO₃(001), although small, is not zero.

In contrast to the film W136, the film W154 exhibits resistive behavior typical for OD films with a large number of defects.[3] As can be seen in Fig. 1, the resistivity of this sample is much higher. Above 280 K the $\rho_{xx}(T)$ curve deviates upward from the linear dependence (dashed line in Fig. 1) because of the enhancement of the electron–electron interaction in HTSC systems of this kind at high temperatures.[15] At the same time, the linear dependence of $\rho_{xx}(T)$ is shifted appreciably to lower temperatures, and the value of T_{*0}, indicated by an arrow in Fig. 1, is of the order of 120±1 K in this case. Such a decrease of the pseudogap region can be explained by the fact that defects prevent the formation of fluctuating Cooper pairs, thus lengthening the region of linear behavior of $\rho_{xx}(T)$.[3] The strong influence of defects and, as a consequence, the presence of a large number of effective pinning centers, is confirmed by the still larger values of the critical current density in comparison with the sample W136 (Fig. 2) and, as will be shown below,

by the different temperature dependences of the FC. Since all the films were grown under identical conditions, we assume that the angle of deviation ϑ of the substrate from the SrTiO₃(001) direction in this case is larger than for the sample W136. On the other hand, this angle is still less than 10°, since for "films with defects" a value $T_{*0} \approx 107 \pm 2$ K is obtained,[3] which indicates a much stronger influence of structural distortions in samples of that kind.

Figure 2 shows the $j_c(T)$ curves for the samples studied. The critical current was determined from the current–voltage (I–V) characteristics as the value of the current at which the voltage reaches 1 μV. We also studied the temperature dependence $j_c(T)$ for a sample W62 which contained practically no defects, as was confirmed by the minimal values of the resistivity (see Table I) and critical current measured in this case. As a consequence, it was possible to investigate $j_c(T)$ practically to helium temperatures. We note that the value $\rho_{xx}(100 \text{ K}) \approx 150 \ \mu\Omega \cdot \text{cm}$ measured for sample W62 is typical for YBCO films without defects.[17,20–22]

In accordance with the theory, the experimental data can be approximated by the expression $j_c(T) = j_c(0)(1 - T/T_c)^s$ (the solid curves in Fig. 2), where the adjustable parameters $j_c(0)$ and s were optimized according to a least-squares fit. A careful analysis shows that $j_c(0) = (0.0029 \pm 0.0003) \times 10^7$ A/cm² and $s = 1.43 \pm 0.02$ for sample W62, $j_c(0) = (0.4 \pm 0.02) \times 10^7$ A/cm² and $s = 1.78 \pm 0.01$ for sample W136, and $j_c(0) = (1.97 \pm 0.03) \times 10^7$ A/cm² and $s = 1.77 \pm 0.01$ for sample W154. Figure 2 shows the following general tendency in the behavior of the critical currents in YBCO films: the larger the resistivity of the film, the larger is j_c. We attribute this behavior to an increase in the number of defects and, hence, pinning centers in the film.[26] Importantly, the value of s increases also. It must be admit-

TABLE I. Parameters of the samples.

Sample	d_0, Å	T_c, K	T_c^{mf}, K	$\rho(100 \text{ K})$, $\mu\Omega \cdot \text{cm}$	$\rho(300 \text{ K})$, $\mu\Omega \cdot \text{cm}$	$d\rho/dT$, $\mu\Omega \cdot \text{cm/K}$	T_{*0}, K	$j_c(0)$, 10^7 A/cm²	s
W154	2500	88.2 (87)	89.76	629	2053	6.73	120	1.97	1.77
W136	2300	86.1 (80)	88.85	239	988	2.67	160	0.4	1.78
W62	1500	84.8 (75)		150				0.0029	1.43

ted that without having data from a structural analysis of the samples, which generally requires special equipment that is expensive and complex, one cannot with complete certainty attribute the observed differences in the behavior of $j_c(T)$ and $\rho_{xx}(T)$ to defects alone unless there are data from some other studies that shed light on this question. In our case this other study was a measurement of the temperature dependence of the fluctuation conductivity, the interrelationship of which with structural defects of YBCO films has been analyzed comprehensively in Ref. 3. Unfortunately, the $\rho_{xx}(T)$ curve of the sample W62 was measured only in the interval $T_c < T < 100$ K, which did not permit us to determine $\rho_N(T)$ and to obtain the dependence $\sigma'(T)$ in that case.

2. THEORY

It is known[35,36] that the effective dimensionality of the electron subsystem of layered superconductors is determined by the relationship between the coherence length along the c axis, $\xi_c(T) = \xi_c(0)(1 - T/T_c)^{-1/2}$, and the distance d between conducting layers. Far from T_c one has $\xi_c(T) \ll d$, and two-particle tunneling between layers cannot occur. In this case the fluctuating pairs (superconducting Cooper pairs below T_c), like the normal carriers, are located in the CuO_2 planes, forming a two-dimensional (2D) electronic state. Near T_c one has $\xi_c(T) > d$, and the Josephson interaction between pairs is realized throughout the volume of the superconductor (3D region). The change in the electron dimensionality (2D–3D crossover) occurs at the temperature T_0 for which $\xi_c(\varepsilon_0) \approx d$,[17] or

$$\xi_c(0) \approx d\varepsilon_0^{1/2}, \tag{2}$$

and should lead to a change in the temperature dependence of both the fluctuation conductivity and the critical current. Here $\varepsilon = \ln(T/T_c^{mf}) \approx (T - T_c^{mf})/T_c^{mf}$ is the reduced temperature, T_c^{mf} is the critical temperature in the mean field approximation,[18] and $d \approx 11.7$ Å is the distance between the CuO_2 conducting layers in YBCO.

There are two fluctuation contributions to $\sigma'(T)$. The direct contribution, which was given a theoretical foundation by Aslamazov and Larkin (AL),[16] arises as a result of the spontaneous formation of Cooper pairs created by fluctuations above T_c, and is dominant in the 3D fluctuation conductivity region near T_c.[35] An additional contribution, introduced by Maki and Thompson (MT)[36] in a development of the AL theory, is interpreted as being the result of an interaction of preformed fluctuating pairs with normal charge carriers and is governed by the pair-breaking processes in a particular sample. The MT contribution depends on the lifetime τ_φ of fluctuating pairs and is dominant in the region of 2D fluctuations, especially in the case of well-structured samples, i.e., in the case of weak pair-breaking.[36]

As was shown in Refs. 3, 6, and 17, in all HTSC systems, independently of the presence or absence of defects, the FC for $T < T_0$ is always described by the equation of AL theory:

$$\sigma'_{AL} = \{e^2/[32\hbar\xi_c(0)]\}\varepsilon^{-1/2}, \tag{3}$$

which determines the FC in any three-dimensional system. In the 2D region, on the contrary, the temperature dependence of the FC depends substantially on the structural inhomoge-

neities of the sample. As was shown in Ref. 17, in the absence of magnetic field the $\sigma'(T)$ curves of YBCO films with good structure are always described in the region $T_0 < T < T_{c0}$ by the MT contribution of Hikami–Larkin (HL) theory[35]

$$\sigma'_{MT} = \frac{e^2}{8\hbar d(1 - \alpha/\delta)} \ln\left[\frac{\delta}{\alpha}\frac{1 + \alpha + (1 + 2\alpha)^{1/2}}{1 + \delta + (1 + 2\delta)^{1/2}}\right]\varepsilon^{-1}. \tag{4}$$

In the presence of structural inhomogeneities in the film[6] the temperature dependence $\sigma'(T)$ is determined by the Lawrence–Doniach (LD) model[37]

$$\sigma'_{LD} = [e^2/(16\hbar d)](1 + 2\alpha)^{-1/2}\varepsilon^{-1}, \tag{5}$$

which is a particular case of the general HL theory. In the presence of strong structural distortions in the sample, in particular, in "films with defects," $\sigma'(T)$ is determined by Eq. (5) but with $d \approx 35$ Å, a fact which we believe is a consequence of a more intense scattering of fluctuating pairs on defects.[3] In Eqs. (4) and (5) the coupling parameter $\alpha = 2\xi_c^2(T)/d^2 = 2[\xi_c(0)/d]^2\varepsilon^{-1}$, and the pair-breaking parameter

$$\delta = 1.203(l/\xi_{ab}(0))(16/\pi\hbar)[\xi_c(0)/d]^2 k_B T \tau_\varphi. \tag{6}$$

The factor $1.203(l/\xi_{ab})$, where l is the mean free path and ξ_{ab} is the coherence length in the ab plane, takes into account the clean-limit approximation introduced in the theory by Bieri, Maki, and Thompson (BMT)[38] under the condition that nonlocal effects can be neglected. In the case for investigating the FC a scale factor C was introduced to take into account the random distribution of the current in the sample in the presence of structural distortions.[18–23] As was shown in Refs. 3, 6, and 17, in YBCO films the C factor has different values in the regions of 3D and 2D fluctuations, and for any films the ratio $C^* = C_{3D}/C_{2D} \approx 1.8$, which reflects the fact that the effective volume of the sample in the region of 2D fluctuations is smaller by approximately a factor of two.[17] In addition, the better the structure of the sample, the closer is C_{3D} to unity.[3,17]

Thus the 2D–3D crossover leads to a change in the character of the interaction of fluctuating pairs (MT–AL crossover) and, as a consequence, to a change in the temperature dependence of the FC, allowing us to determine ε_0 to sufficient accuracy and, with the use of Eq. (2), to obtain reliable values for $\xi_c(0)$. According to theory,[35] MT–AL crossover occurs at the temperature where $\delta \approx \alpha$, which gives

$$\varepsilon_0 = (\pi\hbar)/[1.203(l/\xi_{ab}(0))(8k_B T \tau_\varphi)] \tag{7}$$

and allows one to determine τ_φ if all the remaining parameters of the sample are known. Unfortunately, neither l nor $\xi_{ab}(0)$ has been measured in a fluctuation conductivity experiment. To solve the problem, we introduce the notation $[1.203(l/\xi_{ab})] = \beta$.[17] We assume as before that $\tau_\varphi(T) \sim 1/T$ (Refs. 20–23), and we estimate $\tau_\varphi(100$ K) under the assumption that $\tau_\varphi T = \text{const}$. When these assumptions are taken into account, Eq. (7) can be written as

$$\tau_\varphi \beta T = (\pi\hbar)/(8k_B \varepsilon_0) = A\varepsilon_0^{-1}, \tag{8}$$

where $A = (\pi\hbar)/(8k_B) = 2.988 \times 10^{-12}$ s. Now the parameter $\tau_\varphi(100$ K$)\beta$ is also determined from the measured val-

ue of T_0 and can be used for analysis of the FC. Thus in this case the only remaining adjustable parameter for fitting the theory to the experiment is the C factor.

By virtue of the smallness of j_c near T_c the change in the temperature dependence of the critical currents at the 2D–3D transition has either been attributed to measurement error or has gone unnoticed.[27,30] In the overwhelming majority of papers the main attention is devoted to a comparison of $j_c(T)$ with the expression $j_c(T)=j_c(0)(1-T/T_c)^s$ for $T \ll T_c$ and a comparison of s with the theory.[28,29] A quadratic dependence of $j_c(T)$ is characteristic for polycrystalline samples and the first thin films, which probably had a granular structure also.[25,29] A dependence $j_c(T) \propto (1-T/T_c)^{3/2}$ is observed in epitaxial YBCO thin films with good structure.[39] The quadratic dependence of $j_c(T)$ in polycrystalline samples can be explained by the formation of intergranular contacts mainly of the SNS type.[24–27] In the case of modern YBCO films, attempts to link the observed $j_c(T)$ curves to the formation of the corresponding type of Josephson contacts have led to poor agreement with the high critical current density observed in such films.[26,27,39] As a result, it has long been impossible to obtain a complete picture of the behavior of $j_c(T)$ in high-quality epitaxial HTSC films. The situation was clarified considerably with the appearance of a model for the temperature dependence of the critical currents in HTSCs with low-angle grain boundaries (LGBs) between the crystalline blocks.[27,30]

According to the LGB model, an epitaxial film is divided over its whole thickness into a system of crystalline blocks which are slightly disoriented in the ab plane. The LGBs between these blocks form periodic chains of edge dislocations, the distance between which depends on the mutual misorientation angle θ of the blocks and is determined by the well-known Frank formula $d(\theta)=|\mathbf{B}|/2\sin(\theta/2) \approx |\mathbf{B}|/\theta$, where $|\mathbf{B}|$ is the modulus of the Burgers vector, which is equal in order of magnitude to the lattice constant. It is taken into account in the theory that, because of the short coherence length in HTSCs, the inequality $d(\theta) \gg \xi_{ab}(T)$ holds for the LGBs over a wide temperature interval. Near a periodic chain of parallel edge dislocations (a dislocation wall), within a region with a width of several coherence lengths $\xi_{ab}(T)$, a local suppression of the superconducting order parameter ψ occurs by virtue of the proximity effect, and, as a result, the critical current density through the grain boundaries is lowered substantially as compared to j_0, even at misorientation angles θ for which the nonsuperconducting region around the cores of the edge dislocations do not yet overlap and do not form a continuous insulating or normal (metallic) barrier. On the other hand, the plastically deformed insulating cores of linear edge dislocations lying along a LGB, as was noted above, can act as effective pinning centers for Abrikosov vortices and thereby promote an increase in j_c, especially in the case of parallel orientation of the vortices and dislocations. In this case the temperature dependence of the critical current through the LGB has the form

$$j_c(t,\theta) = (j_0(t)/2)[\Gamma_1^2(t,\theta)+4]^{-1/2}. \tag{9}$$

Here $t=(1-T/T_c)$, and Γ_1 is the transparency of the grain boundary, which depends substantially on the critical
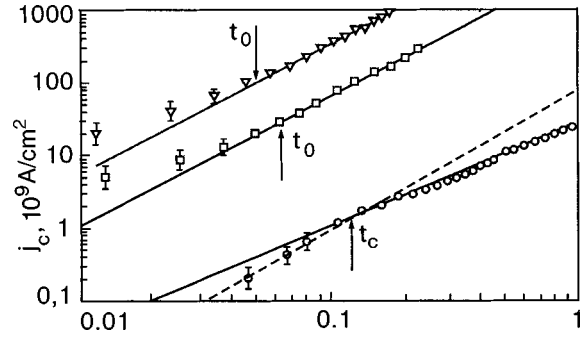

FIG. 3. Temperature dependence of the critical current densities for samples W62 ($\bigcirc$), W136 ($\square$), and W154 ($\triangledown$) in double logarithmic coordinates; the straight lines are plots of the equations $j_c(T)=j_c(0)(1-T/T_c)^s$ for each sample with the same values of the parameters $j_c(0)$ and s as in Fig. 2; the dashed line is a plot of $j_c(T) \sim t^2$. The arrows indicate the temperatures t_0 for samples W154 and W136 and t_c for sample W62.

misorientation angle θ_c above which the averaged potential across the grain boundary begins to exhibit angular and temperature dependence:

$$\theta_c(t) = (2\gamma/\pi)(|\mathbf{B}|\sqrt{t}/\xi_{ab}), \tag{10}$$

where γ is a dimensionless coefficient determined by the spatial distribution of the inhomogeneous order parameter around the edge dislocation: $\gamma = \pi/4$ under the condition $d(\theta)=2\xi_{ab}(T)$; in general one has $\gamma \sim 1$.

According to Ref. 27, for $\theta < \theta_c(t)$, i.e., far from T_c, the parameter Γ_1 is independent of t and θ, so that the temperature dependence of the critical current (9) coincides with the temperature dependence of the pair-breaking current $j_c(t) \sim j_0(t) \sim t^{3/2}$. For $\theta > \theta_c(t)$ the parameter $\Gamma_1 \sim t^{-1/2}$. In this case under the condition $\Gamma_1 > 2$ relation (9) implies that the critical current has a quadratic dependence on t: $j_c(t) \sim t^2$. It should be noted that now $\Gamma_1 \sim \theta$, so that the critical current j_c should fall off with increasing misorientation angle as θ^{-1}. Thus the theory[27] predicts a transition from a dependence $j_c(t) \sim t^{3/2}$ to a dependence $j_c(t) \sim t^2$ in the region of small t, where the critical angle $\theta_c(t)$ becomes smaller than the misorientation angle θ. If this does not occur (if θ is small) then the dependence $j_c(t) \sim t^{3/2}$ will be maintained at all temperatures.

With increasing θ the width of the superconducting channels between the insulating cores of the edge dislocations decreases, vanishing at $\theta \approx 30°$ (Ref. 27). Then a continuous insulating barrier arises along the grain boundary, and that corresponds to a transition to the regime of a Josephson SIS contact, with a linear dependence $j_c(t) \sim t$, which, as far as we know, has never been observed in HTSC films. However, if for some reasons $\Gamma_1 \gg 1$ as before, then the theory[29] for $\theta < \theta_c(t)$ gives a dependence $j_c(t) \sim t^{5/4}$, whereas for $\theta > \theta_c(t)$, i.e., near T_c, a dependence $j_c(t) \sim t^2$, analogous to the dependence of the critical current through a contact of the SNS type, should be realized in that case also.

3. ANALYSIS OF THE RESULTS

A log–log plot of $j_c(t)$ is shown in Fig. 3. The solid lines are the equation $j_c(T)=j_c(0)(1-T/T_c)^s$ plotted for each sample with the same values of the parameters $j_c(0)$

and s as in Fig. 2. It follows from Fig. 3 that with increasing critical current density through the sample the slope of the $j_c(T)$ curves (here equal to s) in the region $T < T_0$, where T_0 was determined from the FC measurements, increases from $s \approx 1.43$ for sample W62 to $s \approx 1.78$ for samples W136 and W154 but remains less than the value $s = 2$ predicted in Ref. 25 for contacts of the SNS type. As the temperature approaches T_c there is a change in slope, which, significantly, occurs in different directions: the slope decreases for the films with large values of j_c (samples W136 and W154) and increases for the film with the small value of j_c (sample W62).

Such a temperature dependence of the critical current density in sample W62 is in complete agreement with the LGB model[27] for small angles θ. It follows from the plot that in the low-temperature region $j_c(T) \sim t^{1.43 \pm 0.02}$ (the lower solid line in Fig. 3), which is close to the theoretically predicted dependence $j_c(T) \sim t^{3/2}$. As T_c is approached, the dependence $j_c(T)$ deviates to larger values of s and, within experimental error, approaches a quadratic law $j_c(T) \sim t^2$ (the dashed line in Fig. 3). These error limits are shown in the figure and are mainly due to inaccuracy in the determination of j_c near T_c. The measurement error for T_c does not exceed the size of the symbols denoting the experimental data points in Fig. 3 and are therefore not shown separately.

According to Ref. 27, at the temperature t_c where the slope of the experimental curves changes from $s = 3/2$ to $s = 2$, the critical angle $\theta_c(T)$ is equal to the maximum grain-boundary angle on the percolation paths of the supercurrent; this makes it possible to estimate the value of the characteristic misorientation angles of the single-crystal blocks in a film. In the present case $t_c \approx 0.133$ (see Fig. 3). Assuming, in analogy with Ref. 27, that $|\mathbf{B}| \approx a \approx 4$ Å, $\xi_{ab}(0) \approx 12$ Å, and $\gamma \approx \pi/4$ and using Eq. (10), we find $\theta \lesssim \theta_c(t_c) \approx 3.7°$, which corresponds to a distance between edge dislocations $d(\theta_c) \approx 66$ Å $\gg \xi_{ab}(0)$. This value of θ is only slightly higher than the value $\theta = 2.5°$ from Ref. 27, whereas $j_c(0)$ is almost a factor of 5×10^2 smaller. The reason for such a large disparity is probably the difference in the transparencies of the grain boundaries, which can be estimated for $t > t_c$ by comparing $j_c(t) = 0.0027 \times 10^7 t^{3/2}$ A/cm² with the pair-breaking current density, which for $\lambda_L(0) = 1500$ Å is equal to $j_0(t) = 3.6 \times 10^8 t^{3/2}$ A/cm² (Ref. 27). Using Eq. (9) for $\theta \lesssim \theta_c(t)$, we obtain $\Gamma_1 \approx 6000$, which, as expected, is 500 times larger than the value $\Gamma_1 = 12$ found in Ref. 27.

Proceeding in a similar way for the samples W136 and W154, we obtain $\Gamma_1 \approx 45$ [$j_c(0) = 0.399 \times 10^7$ A/cm²] and $\Gamma_1 \approx 10$ [$j_c(0) = 1.97 \times 10^7$ A/cm²], respectively. Thus at first glance the decrease of the transparency of the grain boundaries in these films is accompanied by an appreciable increase in the critical current density. However, such behavior does not fit in with the LGB theory. As noted above, the increase in the critical current density is accompanied by a simultaneous increase in the slope of the $j_c(t)$ curves (Fig. 3), which, on the contrary, according to Ref. 27, should decrease with decreasing Γ_1 to a value $s = 5/4$ far from T_c and increase to $s = 2$ on approach to T_c. In our case everything works exactly the opposite: $s \approx 1.78$ far from T_c and decreases to $s \approx 1.5$ near T_c. In addition, the theory[27] attributes the change in slope of the $j_c(t)$ curves to an increase in the

angle θ. As is seen in Fig. 3, for samples W136 and W154 this angle, which is determined by the deviation of $j_c(t)$ from a linear dependence, has a value $\theta \lesssim 2°$, i.e., it is smaller by almost a factor of two than for the sample W62. According to Ref. 27, for such misorientation angles one should observe a dependence $j_c(t) \sim t^{1.5}$ and not $j_c(t) \sim t^{1.78}$, the value that follows from the experiment. In addition, we assume that for films W136 and W154 the estimate for the coefficient Γ_1 suggested in the LGB model does not correspond to the real situation, since, in our view, it is hard to explain how $j_c(0)$ can increase by more than 2.5 orders of magnitude in comparison with sample W62 for the same decrease in the grain-boundary transparency.

Summarizing the results, we can state that the observed increase in the critical current density in samples W136 and W154, as we have said, is due to an increase in the number of pinning centers in the films.[26] We note that such a possibility is not excluded by the theory.[27] However, in our case we attribute this increase not to an increase of θ but to the formation of the above-described specific structural defects of the crystal lattice in films W136 and W154, which arise as a result of an increase in the angle of deviation ϑ of the plane of the substrate from the $SrTiO_3(001)$ direction.[3] It should be noted that, in spite of the fact that the films W136 and W154 actually show the same dependence $j_c(t)$, the value of j_c is 5 times larger for sample W154. It is logical to suppose that this difference is due to different numbers of defects in the films. This hypothesis is confirmed by both the appreciable increase in the resistivity of sample W154 in comparison with W136 and by the decrease in the resistive region of pseudogap behavior (Fig. 1) and also by the results presented below from a study of the fluctuation conductivity in these samples.

For analysis of the FC it is extremely important to determine T_c^{mf} correctly, since outside the critical fluctuation region $\sigma'(T)$ is a function only of $\varepsilon(T - T_c^{mf})/T_c^{mf}$ (Ref. 35). We determine T_c^{mf} by extrapolation of the linear part of the $\sigma'^{-2}(T)$ curve to its intercept with the temperature axis.[18] In this case $T_c^{mf} > T_c$ and is just the temperature at which the FC region separates from the region of critical fluctuations.[17] The data points in Fig. 4 show $\sigma'^{-2}(T)$ for samples W136 and W154. In each figure one can clearly see the 3D region, described by a straight line, the extrapolation of which to the temperature intercept gives $T_c^{mf} \approx 88.85$ K (W136) and ≈ 89.76 K (W154). The 2D–3D crossover temperature T_0 is indicated in Fig. 4 by the arrows. Above T_0, where the 2D fluctuation regime is realized, the points deviate to the right of the straight line for sample W136, indicating the presence of an MT contribution to $\sigma'(T)$.[17] However, in comparison with OD films not containing defects,[17] this deviation is considerably less. For sample W154 above T_0 the experimental points deviate to the left of the straight line, which is characteristic for the LD model and is directly related to the presence of structural distortions in the sample.[3,6]

Figure 5 shows $\sigma'(T)$ for the samples W136. The MT–AL (2D–3D) crossover is clearly seen at $\ln \varepsilon_0 \approx -2.67$, from which we can determine the values $\varepsilon_0 \approx 0.06925$ and $T_0 \approx 95.0$ K. Knowing ε_0 and assuming that $d = 11.7$ Å, it is easily found from Eqs. (2) and (8) that $\xi_c(0) = 3.08 \pm 0.01$ Å and $\tau_\varphi(100$ K$)\beta \approx 4.329 \times 10^{-13}$ s.
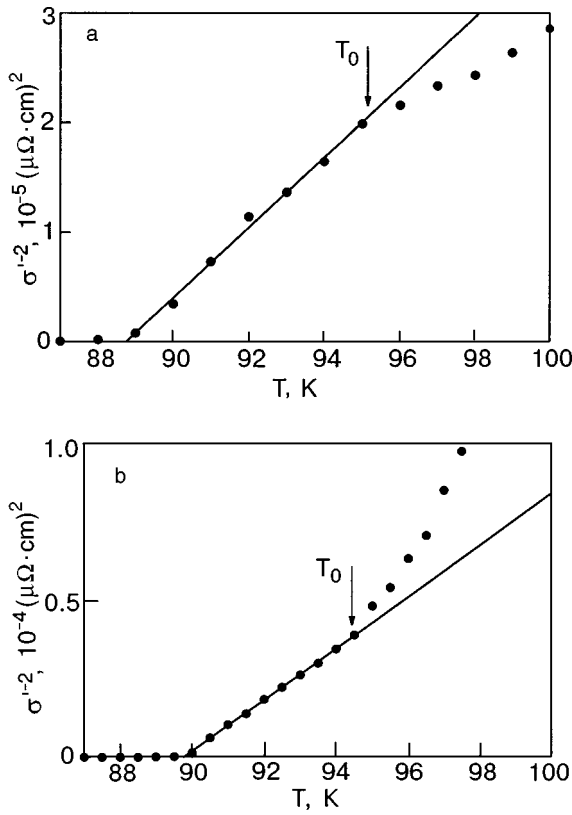
FIG. 4. Temperature dependence of σ'^{-2} for samples W136 (a) and W154 (b); the straight lines show the extrapolations of the 3D region, the intercepts of which with the T axis determine T_c^{mf}; the arrows denote the 2D–3D crossover temperature T_0.

Using the parameters found, we can compare the experimental data with the theory both below and above T_0. As expected, near T_c the temperature dependence of $\sigma'(T)$ is determined by the 3D contribution of AL theory [Eq. (3)] (curve *2* in Fig. 5) with $C_{3D}=0.52$. Above T_0, up to $\ln \varepsilon_{c0} \approx -1.84$ ($T_{c0} \approx 103$ K) the dependence $\sigma'(T)$ is described well by a fluctuation contribution of the MT type [Eq. (3)] (curve *1*) with $C_{2D}=0.292$. In the framework of the approach we have developed to the analysis of the FC in HTSCs,[3,6,17] the presence of a fluctuation contribution of the MT type is an indication that the number of defects directly in the CuO$_2$ planes is relatively small.[3,6] This accords with
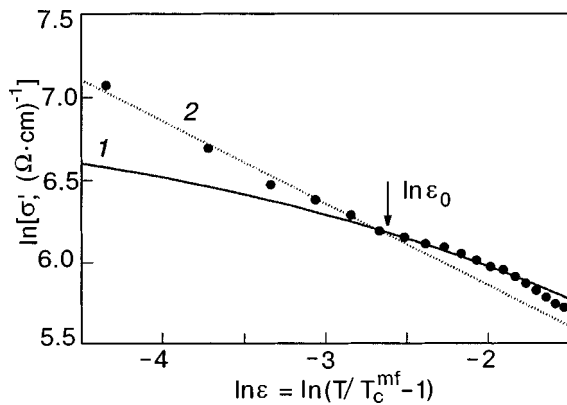

FIG. 5. Comparison of a plot of $\ln \sigma'$ versus $\ln \varepsilon$ (points) for sample W136 ($T_c^{mf}=88.85$ K) with the fluctuation theories: *1*—the MT contribution ($C_{2D}=0.262$, $d=11.7$ Å), *2*—the AL (3D) contribution ($C_{3D}=0.52$).
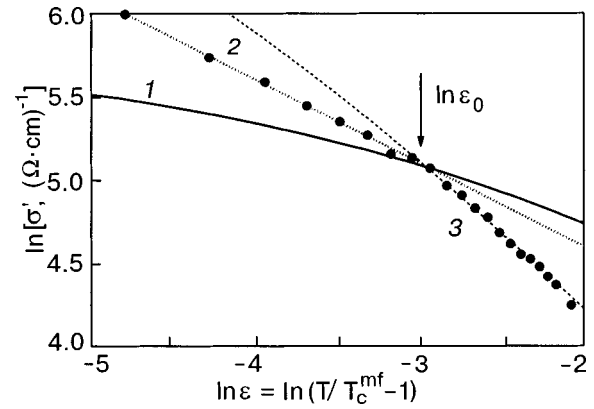

FIG. 6. Comparison of a plot of $\ln \sigma'$ versus $\ln \varepsilon$ (points) for the sample W154 ($T_c^{mf}=89.76$ K) with the fluctuation theories: *1*—the MT contribution ($C_{2D}=0.071$, $d=11.7$ Å), *2*—the AL (3D) contribution ($C_{3D}=0.128$), *3*—the LD contribution ($C=0.225$, $d=35$ Å).

the ideas that defects primarily destroy the conduction in the CuO chains.[26,27,30] As a result, the temperature dependence of the FC (Fig. 5) is, on the whole, the same as it should be in OD YBCO films,[17] and the temperature region in which $\sigma'(T)$ follows fluctuation theory is rather large: $T_{c0}-T_c \approx 14$ K. The influence of defects in this case is manifested in a considerably smaller absolute value of $\sigma'(T)$, as a result of which the factor C_{3D} decreases in magnitude to 0.52. We recall that in OD YBCO films not containing defects one has $C_{3D} \equiv 1$.[17] Nevertheless, $C^* = C_{3D}/C_{2D} \approx 1.80$ as before, confirming the universality of this ratio for HTSCs.[3,6,17] Thus analysis of the FC clearly reveals the presence of defects in the film, the influence of which on the properties of the sample in the present case is much greater than in W62 but, at the same time, considerably less than in W154.

As expected, for sample W154 the $\sigma'(T)$ curve is typical for "films with defects" (see Fig. 6). The 2D–3D crossover, indicated by the arrow, is clearly seen in the figure at $\ln \varepsilon_0 \approx -2.97$, from which we find $\varepsilon_0 \approx 0.0513$ and $T_0 \approx 94.4$ K. Knowing ε_0 and assuming $d=11.7$ Å, it is easily found from Eqs. (2) and (8) that $\xi_c(0)=2.65 \pm 0.01$ Å and $\tau_\varphi(100$ K$)\beta \approx 5.843 \times 10^{-13}$ s. Using the parameters found, we can compare the experimental data with the theory both below and above T_0. As before, near T_c the excess conductivity $\sigma'(T)$ is determined by the 3D contribution of AL theory [Eq. (3)] (curve *2* in Fig. 6), but the absolute value of σ' is practically a factor of 4 smaller than for W136, and, as a consequence, $C_{3D}=0.128$. Above T_0, however, up to $\ln \varepsilon_{c0} \approx -2.17$ ($T_{c0} \approx 100$ K), $\sigma'(T)$ is described by the LD model [Eq. (5)] (curve *3* in Fig. 6), but with $d=35$ Å. According to Ref. 3, such a temperature dependence of the FC arises as a result of strong structural distortions in the sample, and the formal increase of d to 35 Å reflects the fact that the intensity of scattering of fluctuating pairs in the 2D region in this case is three times higher because of the effect of defects. As a result, the temperature region in which $\sigma'(T)$ follows fluctuation theory, $T_{c0}-T_c \approx 10$ K, in this case is 4 K smaller than in the sample W136 and, as was mentioned above, the region of pseudogap behavior on the $\rho_{xx}(T)$ curve is also diminished strongly, and T_{*0} approaches T_c.

Nevertheless, the MT contribution [Eq. (3)] calculated

using the values of $\xi_c(0)$ and $\tau_\varphi(100\ \text{K})\beta$ determined above with very small $C_{2D} \approx 0.071$ intersects the experimental data precisely at the crossover temperature T_0 (curve *1* in Fig. 6). Here, as expected, the ratio $C^* = C_{3D}/C_{2D} \approx 1.80$. In accordance with the conclusions of Refs. 3 and 17, this result confirms the correctness of the FC analysis. However, as can be seen in Fig. 6, above T_0 the experimental points lie far below curve *1*, indicating the presence of defects directly in the CuO$_2$ planes[3] in this case. It should be stressed that the observed temperature dependence of σ' arises only in the case when the defects in the HTSC film are formed as a result of an increase of the angle of deviation ϑ of the substrate plane from the SrTiO$_3$(001) direction.[3] Thus analysis of the FC indicates rather convincingly that defects have a strong influence on the properties of the W154 film and, in our view, confirms the hypotheses made above as to the decisive influence of defects and the related pinning centers on the increase in the critical current density in such films.

The values of the 2D–3D crossover temperature T_0 obtained from the FC analysis for samples W136 and W154 are indicated by arrows in Fig. 3 (in units of $T_0/T_c = t_0$). With allowance for the experimental error, these temperatures correlate rather well with the temperatures corresponding to the deviation of $j_c(T)$ from the linear dependence. In our view, this result confirms the hypothesis made above that the decrease in slope of $j_c(T)$ in such films is due to the realization of a 3D electronic state of the HTSC system near T_c. In this temperature region the coherence length in the film, both along the c axis and, especially, in the ab plane, becomes very large and ceases to be sensitive to defects. In a smooth flow of the vortices (the "ρ flow" regime) the distribution of the current over the cross section of the sample becomes uniform, and, as a result, a dependence $j_c(T) \propto t^{3/2}$ is realized, as in narrow channels.[40] Unfortunately, the small number of experimental points near T_c does not permit a convincing confirmation of this conclusion. A definitive answer to this question will no doubt require more careful measurements, especially in this temperature interval.

With the results obtained we can now return to a discussion of certain aspects of the pseudogap behavior in HTSCs.[1–5] As we have said, it is assumed in a number of papers[1,12] that $\Delta(T_c)/\Delta(0) \approx 0.6$ (see, e.g., Fig. 5 of Ref. 12), and the minimum of the density of states is also observed for $T \gg T_c$. This raises the question: why, then, does the critical current always decrease to zero as T approaches T_c (Fig. 2) and vanish in the pseudogap region while the fluctuating Cooper pairs, which are presumably responsible for the appearance of the pseudogap at $T > T_c$, follow fluctuation theory[6,17] to at least $T \approx 105$ K, which is at minimum 15 K above T_c? Moreover, in a temperature interval of the order of 5 K above T_c a 3D electronic state, in which fluctuating pairs interact throughout the volume of the superconductor, is realized in the films. In the framework of the pseudogap approach it would be logical to hope that the critical current might be detected at least in this temperature region. In reality, however, this does not happen. One of the possible reasons for such behavior, in our view, is critical fluctuations, which destroy the phase coherence of the pairs at the transition through T_c. In all probability, by virtue of the smallness of both $\xi(T)$ and the total number of carriers in HTSCs,[1] the

phase coherence above T_c^{mf} is no longer completely restored, despite the relatively long lifetime of the fluctuating pairs.[6,17] Nevertheless, the nonlinearity of the current–voltage characteristics of the films studied arises for $T \lesssim T_{*0}$ and increases monotonically as T decreases to T_c; this, we believe, can be adjudged to be additional evidence of the existence of preformed pairs in the pseudogap regime. In this connection we should also note Ref. 8, which reported the observation of a coherent current of bosons with charge $2e$ in YBCO films at temperatures at least 30 K above T_c. The authors note that this current is carried by a very small number of coherent bosons (fluctuating pairs) against the background of a large number of incoherent states. If this is true, then the critical fluctuations near T_c can completely destroy the coherent states, and above T_c^{mf} the sensitivity of the usual methods of measurement may be insufficient for detection of the critical currents. This question will undoubtedly require a more careful study.

CONCLUSION

We have for the first time carried out a comparative analysis of the results obtained in measurements of the fluctuation conductivity and of the critical currents in YBa$_2$Cu$_3$O$_{7-y}$ films containing different amounts of defects. An interrelation between the value and temperature dependence of the FC and the values and temperature dependences of the critical current and resistivity of the samples is revealed and established. It follows from measurements of the FC that the change in these values and dependences is directly linked to a change in the number of defects and, hence, of pinning centers in the films studied; these defects arise predominantly as a result of a deviation of the plane of the substrate from the SrTiO$_3$(001) crystallographic direction. Thus analysis of the FC is a relatively simple and extremely effective method of obtaining reliable information about the presence of defects and their influence on the properties of HTSC films, especially in the case when for some reason it is not possible to carry out a structural analysis. In this approach one can also understand the results of measurements of $j_c(T)$ in the samples studied.

We have shown that in practically defect-free films (sample W62) the dependence $j_c(T)$ completely follows the LGB model,[27] exhibiting a slope $s \approx 3/2$ far from T_c and $s \approx 2$ near T_c. From the temperature t_c at which the change in slope occurs we determined the angle of mutual misorientation of the blocks, $\theta \lesssim \theta_c(t_c) \approx 3.7°$, which corresponds to distances between edge dislocations $d(\theta_c) \approx 66$ Å $\gg \xi_{ab}(0)$ and a grain-boundary transparency of $\Gamma_1 \approx 6 \times 10^3$. As expected, the angle of mismatch in the given case is small, and accordingly the transparency is extremely large.

At the same time, the increase of the slope of the $j_c(T)$ curve and the sharp increase of the critical current density observed in samples W136 and W154 cannot be explained in the LGB model. The slope of $j_c(T)$ predicted by the theory, $s = 5/4$, does not correspond to experiment, and the small values of the grain-boundary transparency cannot account for the high values of $j_c(0)$ observed in the experiment. It is shown that in that case the observed behavioral relationships in HTSC films is explained by the different numbers of defects in the samples. It should be noted that as the number of

defects in the film increases, the value and slope of $j_c(T)$ increase rapidly, and the maximum value $j_c(0) = 1.97 \times 10^7$ A/cm^2 with a slope $s \approx 1.78$ observed in sample W154, for which the influence of defects was most pronounced. We assume on the basis of the data obtained that the physics of the processes which determine the value and temperature dependence of j_c in such samples is completely different from that in well-structured films and, as FC analysis shows, is due to the specifics of the structure of the defects formed in c-oriented epitaxial HTSC films.[26]

In closing the authors thank A. I. Akimenko for valuable comments in a discussion of the results of tunneling experiments in HTSCs.

*E-mail: solovjov@ilt.kharkov.ua

[1] T. Timusk and B. Statt, Rep. Prog. Phys. **62**, 61 (1999).

[2] C. Carballeira, S. R. Curras, J. Vina, and J. A. Veira, Phys. Rev. B **63**, 144515-1 (2001).

[3] A. L. Solovjov, Fiz. Nizk. Temp. **28**, 1138 (2002) [Low Temp. Phys. **28**, 812 (2002)].

[4] K. Maki and H. Won, J. Magn. Magn. Mater. **226−230**, 350 (2001).

[5] A. A. Abrikosov, Phys. Rev. B **64**, 104521 (2001).

[6] A. L. Solovjov, H.-U. Habermeier, and T. Haage, Fiz. Nizk. Temp. **28**, 144 (2002) [Low Temp. Phys. **28**, 99 (2002)].

[7] V. J. Emery and S. A. Kivelson, Nature (London) **354**, 434 (1995).

[8] K. Kawabata, S. Tsukui, Y. Shono, O. Mishikami, H. Sasakura, K. Yoshiara, Y. Kakehi, and T. Yotsuya, Phys. Rev. B **58**, 2458 (1998).

[9] J. R. Engelbrecht, A. Nazarenko, M. Randeria, and E. Dagotto, Phys. Rev. B **57**, 13406 (1998) and references therein.

[10] C. Carballeira, S. R. Curras, J. Vina, and J. A. Veira, Phys. Rev. B **63**, 144515-1 (2001).

[11] V. M. Dmitriev, A. L. Solov'ev (Solovjov), and A. I. Dmitrenko, Fiz. Nizk. Temp. **15**, 200 (1989) [Sov. J. Low Temp. Phys. **15**, 356 (1989)].

[12] M. Suzuki, T. Watanabe, and A. Matsuda, Phys. Rev. Lett. **82**, 5361 (1999).

[13] Y. Iye, in *Physical Properties of High Temperature Superconductors III*, D. M. Ginsberg (ed.), World Scientific, Singapore (1992), p. 285.

[14] C. P. Slichter, in *Strongly Correlated Electronic Systems*, K. S. Bedell (ed.), Addison-Wesley, New York (1994).

[15] B. P. Stojkovic and D. Pines, Phys. Rev. B **55**, 8576 (1997) and references therein.

[16] L. G. Aslamazov and A. I. Larkin, Phys. Lett. A **26**, 238 (1968).

[17] A. L. Solovjov, H.-U. Habermeier, and T. Haage, Fiz. Nizk. Temp. **28**, 24 (2002) [Low Temp. Phys. **28**, 17 (2002)].

[18] B. Oh, K. Char, A. D. Kent, M. Naito, M. R. Beasley, T. H. Geballe, R. H. Hammond, A. Kapitulnik, and J. M. Graybeal, Phys. Rev. B **37**, 7861 (1988).

[19] T. A. Friedmann, J. P. Rice, John Giapintzakis, and D. M. Ginsberg, Phys. Rev. B **39**, 4258 (1989).

[20] K. Winzer and G. Kumm, Z. Phys. B: Cond. Matter **82**, 317 (1991).

[21] A. Gauzzi and D. Pavuna, Phys. Rev. B **51**, 15420 (1995).

[22] W. Lang, G. Heine, P. Schwab, X. Z. Wang, and D. Bauerle, Phys. Rev. B **49**, 4209 (1995).

[23] A. L. Solovjov, V. M. Dmitriev, H.-U. Habermeier, and I. E. Trofimov, Phys. Rev. B **55**, 8551 (1997) and references therein.

[24] G. Deutscher, IBM J. Develop. **33**, 293 (1989).

[25] L. G. Raffo and T. O. Woodruff, Nuovo Cimento D **13**, 247 (1991).

[26] T. Haage, J. Q. Li, B. Leibold, M. Cardona, J. Zegenhagen, and H.-U. Habermeier, Solid State Commun. **99**, 553 (1996).

[27] É. A. Pashitskiǐ, V. I. Vakaryuk, S. M. Ryabchenko, and Yu. V. Fedotov, Fiz. Nizk. Temp. **27**, 131 (2001) [Low Temp. Phys. **27**, 96 (2001)].

[28] G. Blatter, M. V. Feigelman, V. G. Geshkenbein, A. I. Larkin, and V. M. Vinokur, Rev. Mod. Phys. **66**, 1125 (1994).

[29] V. M. Pan, Usp. Fiz. Met. **1**, 49 (2000).

[30] É. A. Pashitskiǐ and V. I. Vakaryuk, Fiz. Nizk. Temp. **28**, 16 (2002) [Low Temp. Phys. **28**, 11 (2002)].

[31] P. G. de Gennes, Rev. Mod. Phys. **36**, 225 (1964).

[32] N. L. Rowell and H. J. Smith, Can. J. Phys. **54**, 223 (1976).

[33] H.-U. Habermeier, Appl. Surf. Sci. **69**, 204 (1993).

[34] V. M. Dmitriev, E. L. Kravchenko, M. N. Ofitserov, N. N. Prentslau, V. N. Svetlov, and V. B. Stepanov, Fiz. Nizk. Temp. **19**, 453 (1993) [Low Temp. Phys. **19**, 318 (1993)].

[35] W. E. Lawrence and S. Doniach, in *Proceedings of the Twelfth International Conference on Low Temperature Physics*, Kyoto (1971), p. 361.

[36] S. Hikami and A. I. Larkin, Mod. Phys. Lett. B **2**, 693 (1988).

[37] K. Maki, Prog. Theor. Phys. **39**, 897 (1968); R. S. Tompson, Phys. Rev. B **1**, 327 (1970).

[38] J. B. Bieri, K. Maki, and R. S. Thompson, Phys. Rev. B **44**, 4709 (1991).

[39] Yu. V. Fedotov, S. M. Ryabchenko, and A. P. Shakhov, Fiz. Nizk. Temp. **26**, 638 (2000) [Low Temp. Phys. **26**, 464 (2000)].

[40] J. B. Kim, C. F. Hempsteed, and A. R. Strinad, Phys. Rev. A **139**, 1163 (1965).

Translated by Steve Torstveit

Antiferromagnetic correlations in superconducting YBa$_2$Cu$_3$O$_{6+x}$ samples from optical absorption data; comparison with the results of neutron and muon experiments

V. N. Samovarov,* V. L. Vakula, and M. Yu. Libin

B. Verkin Institute for Low Temperature Physics and Engineering, National Academy of Sciences of Ukraine, pr. Lenina 47, 61103 Kharkov, Ukraine

Narrow-band spectral features demonstrating a high sensitivity to the development of the pseudogap state are detected in metallic films of YBa$_2$Cu$_3$O$_{6+x}$ with $T_c \approx 51$ and 74 K. Attention is focused on the temperature behavior of the exciton–bimagnon band $A+3J$ (≈ 2.15 eV) and the exciton–two-magnon band $A+4J$ (≈ 2.28 eV); these bands arise as a result of phase separation into insulating and metallic regions. By comparing the optical results with published data on the temperature behavior of the muon depolarization rate and the integrated intensity of the (π,π) magnetic resonance it is shown for the first time that all three independent techniques give the same observed temperature dependence $f(T/T_c)$ of measured quantities both in the normal and superconducting states. The established correlation of the optical, neutron, and muon data is analyzed from the standpoint of the formation of stripe ordering and the compatibility of antiferromagnetic order and superconductivity. © *2003 American Institute of Physics.* [DOI: 10.1063/1.1630713]

1. INTRODUCTION

The antiferromagnetic (AF) correlations and stripe ordering in copper oxides are the subject of lively discussions in the physics of high-temperature superconductivity. In the stripe ordering picture a phase separation into insulating and metallic regions (stripes) occurs in metallic YBCO samples, and the insulating stripes are responsible for the development of the AF correlations. The most fruitful approach to studying the question of the interrelationship of superconductivity and AF correlations consists in a comparison of the data of the independent experimental techniques. In this paper we analyze published data from neutron[1] and muon[2] spectroscopy and the data of our measurements of the absorption spectra of thin films of YBCO with different doping levels. A comparison of the results is carried out for both the normal and superconducting states.

The main motivation for such a comparative analysis is as follows. First, none of the techniques mentioned above can be said to be completely self-sufficient for constructing the complex picture of the development of AF correlations and stripe ordering in cuprate HTSCs. For example, for the normal and superconducting states of YBCO the interpretation of the muon spectroscopy data and their relation to the neutron results are not completely clear (see the discussion in Refs. 2 and 3). Second, in the studies known to us, the comparative analysis with the neutron spectroscopy data has been done using the temperature behavior of only the peak intensity of the (π,π) resonance (see, e.g., Ref. 4, where a comparison was made with the temperature behavior of the low-frequency conductivity in YBCO). Detailed and very complex neutron measurements of the temperature dependence of the integrated intensity of the (π,π) resonance have been done only in Ref. 1 (the authors used the results in a description of the temperature behavior of the heat capacity)

and, in our view, have not yet been fully utilized in the analysis of the results of other experiments. It should also be noted that the very nature of the (π,π) resonance has been considered in the framework of various models.[5] Third, although the sensitivity of the interband transitions to the formation of the pseudogap and superconducting states of YBCO was shown in Refs. 6 and 7, direct evidence of the interrelationship of interband transitions and the AF fluctuations and stripe ordering is needed, which will come primarily from a comparison with the data of neutron spectroscopy—a technique widely used in the study of AF fluctuations.

Based on what we have said, it is not clear whether there is a single consistent temperature dependence of the results of the three techniques listed above in the normal and superconducting states of cuprate HTSCs, including YBCO. In this regard a comparative analysis of the optical, neutron, and muon data is undoubtedly of interest and will allow one to track the development of AF coherence of the short-range order upon cooling of metallic YBCO samples, including the regions of stripe ordering and the superconducting state, by three independent techniques.

In the present study we have investigated the interband transitions at energies $\hbar\omega > E_g$. The existence of an optical gap $E_g \approx 1.4$–1.9 eV, separating the pd-hybridized valence band and the upper Hubbard band with a large relative contribution of the d orbitals of copper, is one of the fundamental features of the electronic structure of copper-oxide HTSCs.[8] In these compounds the gap creates conditions for interband transitions with charge transfer from the oxygen to the copper: $Cu^{2+}O^{2-} \rightarrow Cu^+O^-$. In doped copper-oxide HTSCs the gap in the metallic phase is preserved upon the appearance of holes in the valence band all the way to the optimal doping level with the maximum value of T_c (≈ 0.15 holes per CuO$_2$ plane).

In connection with what we have said, we note that in

982

nonmagnetic superconductors, e.g., those based on Ba–K–Bi–O, the optical gap (≈ 2 eV) exists only in the insulator phase and is of the nature of a charge-density wave, and upon doping it is rapidly destroyed in an insulator–metal transition.[9]

The preservation of the optical gap over a wide doping range makes it possible to pose interesting problems in the spectroscopy of charge and spin correlations in copper-oxide HTSCs. Thus it has turned out that most of the research on the optical properties of cuprate HTSCs has been done for the intraband transitions with $\hbar\omega < E_g$, especially in the region ≈ 0.01–0.1 eV, which corresponds to the energy scale of both the spin pseudogap of the normal phase and the superconducting gap. At the same time, at the interband transitions, where the photon energy is considerably larger than the superconducting pairing energy, a nontrivial effect wherein the optical spectra are sensitive to superconductivity has been observed[10] (various theoretical models have been proposed[11] to explain this effect).

There are two main methods that have been most actively developed in recent years for the region of interband transitions: absorption spectroscopy, and resonance Raman scattering. In both cases the samples are investigated using the absorption of light with energy near and above E_g. Both methods make it possible to distinguish the spectral features due to the excitation of magnons (bimagnons) either in the process of optical absorption or in Raman scattering. In the Raman scattering case in YBCO the bimagnon band due to the creation of two interacting magnons lies at $\hbar\omega_{2m} \approx 3000$ cm^{-1} (Refs. 12 and 13) (which corresponds to an energy of $2.7J$, where J is the exchange coupling for the spins of Cu^{2+} in the CuO_2 plane), which will be denoted below as the $3J$ band of Raman scattering. In the absorption case a band has been detected at an energy $E_g + \hbar\omega_{2m} \approx 2.15$ eV; this band, denoted below as the $A + 3J$ band, has been attributed to an electron–bimagnon transition.[6] It has been shown that these bimagnon features in the absorption and scattering spectra weaken rather rapidly with doping at room temperatures. At the same time, it has been established[7] that in metallic YBCO films the $A + 3J$ absorption band and the new "magnon" features appear as the temperature is lowered.

In this paper we establish with a high degree of reliability a correlation between the optical absorption data at interband transitions with the participation of the magnon subsystem, the behavior of the integrated intensity of the magnetic (π, π) resonance, and the muon relaxation rate in the entire existence region of the pseudogap state and superconducting phase. Such a correlation reveals features of the development of AF ordering of the short-range order both in the normal phase of stripe ordering and in the superconducting phase. It is shown that in regard to its sensitivity to AF correlations, interband optical spectroscopy is comparable to neutron and muon spectroscopy. We analyze the appearance of stripe ordering in the pseudogap state, the preservation of this ordering in the superconducting phase, and the coexistence of the AF and superconducting gaps. The main findings of this paper are briefly stated in the Conclusion.

2. SAMPLES AND MEASUREMENT TECHNIQUES

In this study we have measured the optical absorption spectra of thin $YBa_2Cu_3O_{6+x}$ films with doping indices corresponding to both the insulating phase, $x \approx 0.3$–0.35, and the metallic phase, $x \approx 0.8$ and $x \approx 0.5$.[1)] The YBCO films of thickness $l \approx 2300$ Å had the c orientation with respect to the $SrTiO_3$ substrates. We measured the absolute absorption spectra (optical density αl, where α is the absorption coefficient) at 300 K and also the temperature variations of the spectra on cooling of the films from 300 to 20 K. The difference spectra $\Delta(\alpha l) = \alpha l(T) - \alpha l(T_0)$ were measured in a temperature scan, where T_0 is the initial temperature of the measurements. The difference spectra made it possible to reliably reveal very small temperature variations of the absorption coefficient, $\Delta(\alpha l) = 0.005$, at the level of absolute values ≈ 2.5. The absorption spectra were reconstructed from the transmission spectral data on the assumption that the variations of the reflection coefficient upon variation of the temperature are small, $\Delta R \ll \Delta\alpha$. In the interval 1.4–3 eV, where such an approximation is well fulfilled,[14] the spectra were taken with a step $\approx 3 \times 10^{-3}$ eV. Measurements of the temperature difference spectra make it possible to reveal fine spectral anomalies in the absorption, including those due to the formation of a superconducting phase both in the Y- and Bi-type samples.[6,10]

We also note the following. In the interband transition region, in addition to the equilibrium spectra we also investigated various sorts of photoinduced (nonequilibrium) effects, e.g., reflecting the accumulation of nonequilibrium holes[15] and the suppression of two-magnon scattering by photodoping.[16] The light doses for the appearance of photoinduced phenomena in cuprate HTSCs are approximately 10^{15}–10^{16} photons/cm^2. In this paper the absorption spectroscopy is done with small light doses not causing photoinduced changes.

3. INSULATING PHASE

Let us first consider the absolute absorption spectrum $\alpha l(\omega)$ of an insulating film with $x \approx 0.3$ and compare it with the excitation spectrum $R_{2m}(\omega)$ of the bimagnon band in the Raman scattering experiments. The behavior of $R_{2m}(\omega)$ describes the dependence of the intensity of the maximum of the bimagnon $3J$ band on the incident light energy $\hbar\omega_i$. According to theoretical calculations,[17] the maximum of the bimagnon band lies a distance $\Delta\hbar\omega \approx 2.71J \approx 0.33$ eV (or $3.14J$ if the Oguchi quantum correction is taken into account) from the excited photon energy $\hbar\omega_i$, where $J \approx 0.12$ eV is the exchange energy of the copper spins in the CuO_2 planes. In a rough approximation the energy of the bimagnon for a square lattice with spins $s = 1/2$ can be assumed equal to $3J$. This quantity is obtained as the difference of the total energy of two noninteracting magnons at the Brillouin zone edge, $2\hbar\omega_m = 2zJs = 4J$ ($z = 4$ is the number of nearest neighbors) and the bimagnon binding energy J. We note that the value $\Delta\hbar\omega \approx 0.33$ eV is typical for copper-oxide HTSCs.

Figure 1a shows the absorption spectrum $\alpha l(\omega)$ obtained here and the spectrum $R_{2m}(\omega)$ from Ref. 12. The data are presented for 300 K, which corresponds to the region
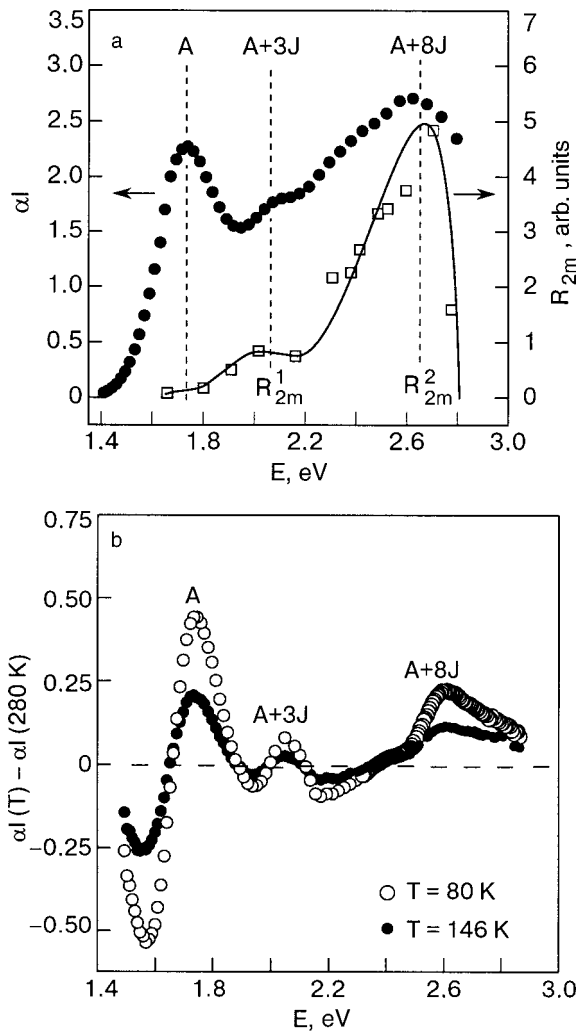
FIG. 1. Optical absorption spectrum $\alpha l(\omega)$ of an insulating film $YBa_2Cu_3O_{6+x}$ ($x \approx 0.3$) and the excitation spectrum of the two-magnon scattering band $R_{2m}(\omega)$ (Ref. 12) of an insulating sample of $YBa_2Cu_3O_6$ at 300 K (a); temperature variations of the absorption spectra on cooling of an insulating film $YBa_2Cu_3O_{6+x}$ ($x \approx 0.3$) from 280 K. For visual clarity the spectra for 80 and 146 K have been shifted upward by 0.14 and 0.1, respectively (b).

near the Néel temperature T_N. It is seen that the absorption spectra have three maxima, which we denote as A (1.75 eV), $A+3J$ (2.06 eV), and $A+8J$ (2.65 eV). We also observed these bands at a temperature of 400 K, i.e., in the region of short-range AF order. According to the analysis of Ref. 7, the maximum A is an edge lying at an energy close to the gap E_g, and is shifted slightly on doping because of the change in E_g. It is seen in Fig. 1a that the absorption peaks $A+3J$ and $A+8J$ correlate well with the maxima R_{2m}^1 and R_{2m}^2 in the excitation spectrum of the Raman scattering. In the low-temperature Raman scattering experiments of Blumberg (see the discussion in Ref. 18) a weak feature at energy E_g was observed in addition to the peaks $R_{2m}^{1,2}$ shown in the figure.

Thus there is a direct correlation between the spectral features of $\alpha l(\omega)$ and $R_{2m}(\omega)$, indicating that the interband transitions with charge transfer are due to the AF subsystem of the insulator. In particular, based on the theoretical analysis,[18] it can be said that the $A+3J$ peak in the absorption spectra corresponds to the threshold energy of the inter-

band transition with the formation of an electron–hole pair and the additional excitation of a bimagnon. The fact that the distance between the A and $A+3J$ bands agrees rather well within the experimental error limits with the bimagnon energy attests to the fact that the influence of the exchange interaction of an optically excited ion with the environment, the finite width of the exciton band, and the noncollinearity of the AF sublattices at the position of the $A+3J$ band can be neglected. To isolate these contributions requires special studies, as has been shown in papers with classical antiferromagnets.[19] As is seen in Fig. 1a, the bimagnon Raman scattering band is excited most efficiently at the peak $A+8J$ in the region 2.7 eV, when the fermions are found above the bottom of their bands. This is justified theoretically in Ref. 18 as a manifestation of the so-called triple resonance in the Raman scattering spectra.

Let us now track the behavior of the peaks in the $\alpha l(\omega)$ spectra as the sample is cooled. We observed enhancement of the A, $A+3J$, and $A+8J$ bands as the temperature was lowered from 400 to 300 K, i.e., in the region of the short-range AF order. Data for the temperature region of the long-range AF order are given in Fig. 1b in a plot of the difference spectrum $\Delta(\alpha l) = \alpha l(T) - \alpha l(280 \text{ K})$. It is clearly seen that the three spectral features indicated, A, $A+3J$, and $A+8J$, are affected most strongly by the temperature variations.

As the temperature is lowered, the A band narrows, so that a minimum appears on the difference spectra (described in Refs. 6 and 7 by the temperature difference of two Gaussians) near 1.6 eV. On the short-wavelength side of the A band this minimum is expressed very weakly. That is possible if the A band has a long non-Gaussian short-wavelength wing, e.g., because of the opening of a magnon band of width $\approx 2J$ in the absorption process. In this case the difference spectra will not have a deep short-wavelength minimum.

The width of the electron–bimagnon band $A+3J$ in the phase of long-range AF order varies weakly with temperature, but its intensity increases noticeably, as does the intensity of the $A+8J$ component. On cooling below a characteristic temperature $T_g = 60-70$ K the variations cease, as was mentioned previously.[6,7] For illustration of what we have said, Fig. 2 gives the temperature behavior of the absorption near 1.6 eV on the long-wavelength wing of the A band. The transition to the temperature-independent part below T_g occurs extremely sharply. Let us point out immediately that such a sharp kink on the temperature dependence of the exciton–magnon absorption is a characteristic property of low-dimensional AF insulators and occurs when $k_B T_g \approx \Delta_{AF}$, where Δ_{AF} is the value of the AF gap.[20] This question will be discussed in more detail below.

For a film with a somewhat larger doping index ($x \approx 0.35$) the A band lies at 1.77 eV, while the $A+3J$ band is at 2.12 eV. For this film all the main traits of the picture discussed above are retained. Both films, which are found near the boundary of the insulator–metal transition, have localized hole carriers. According to the data of Ref. 21, the activation energy for the mobility in these films is $E_a \approx 0.18$ ($x \approx 0.3$) and 0.03 eV ($x \approx 0.4$).
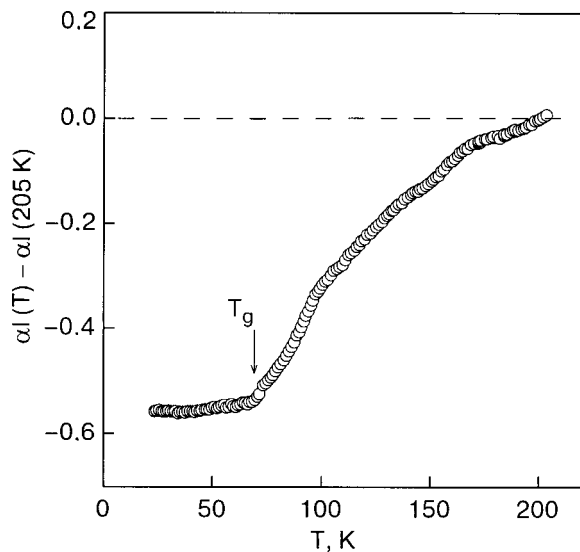
FIG. 2. Temperature variations of the intensity of the long-wavelength wing of the exciton A absorption band, measured at 1.6 eV for an antiferromagnetic film YBa$_2$Cu$_3$O$_{6+x}$ ($x \approx 0.3$).

FIG. 3. Difference spectrum of the absorption of metallic films YBa$_2$Cu$_3$O$_{6+x}$ on cooling from 170–200 K to the region $T < T_c$. The main figure is for the sample with $T_c \approx 74$ K, the inset for the sample with $T_c \approx 51$ K.

4. METALLIC PHASE

Let us now consider the temperature variations of the absorption spectrum in the same spectral interval for metal films with $T_c \approx 74$ and 88 K (ortho-I phase) and with $T_c \approx 51$ K (ortho-II phase) in the normal and superconducting states. For 300 K the absorption spectra of metallic films in the region of interband transitions were analyzed in Ref. 6, including their change with doping.[6] This analysis showed that upon doping, i.e., with decreasing correlation length of the AF fluctuations, the A and $A + 3J$ components rapidly weaken (especially the $A + 3J$ component), and for films with $T_c \gtrsim 70$ K one can say that the bands are absent. In the Raman spectra the bimagnon band in YBCO also begins to weaken rapidly with doping, and it is not seen for samples with $T_c \approx 70$ and 88 K.[13]

Before presenting the data on the temperature evolution of the spectra with a small temperature step, let us consider the difference spectrum over a wide temperature range $\Delta(\alpha l) = \alpha l(70 \text{ K}) - \alpha l(200 \text{ K})$, which demonstrates the unusual physical picture that is central to our discussion. This spectrum for the film with $T_c \approx 74$ K is shown in Fig. 3. The wideband (continuous) weakening of the absorption, $\Delta(\alpha l) < 0$, over the whole spectral interval 1.6–3.0 eV, with a maximum value $\Delta(\alpha l) \approx -0.17$, was discussed in Ref. 6 and will not be considered here.

More interesting is the fact that, appearing against the background of the wideband temperature variation are components which are characteristic for the insulating phase: the A band (1.8 eV), the $A + 3J$ band (2.15 eV), and the $A + 8J$ band (2.8 eV). Besides these bands, which appear and grow stronger as the temperature is lowered, a new component, $A + 4J$, which is absent in the spectra of the insulator at both room and low temperatures, is observed at 2.28 eV. Its appearance in the metallic ortho-I phase of YBCO was first detected earlier in this cycle of measurements.[22] There, however, detailed temperature measurements over a wide energy interval were not made, and the behavior of this component on doping was not investigated. We first observed the appear-
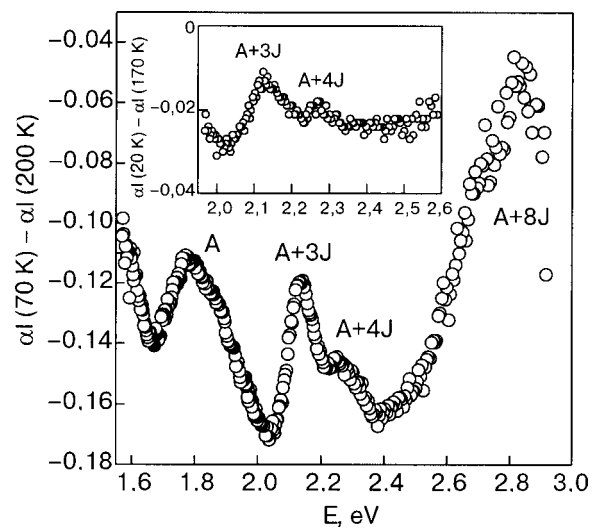
ance of the $A + 3J$ and $A + 4J$ bands on cooling of films of the ortho-II phase with $T_c \sim 50$ K, as is illustrated in the inset in Fig. 3. The amplitudes of these components in the case of the ortho-II phase are smaller by a factor of 1.5–2 than for the ortho-I phase.

The spectrum in Fig. 3 is formed in the normal state. This is illustrated by measurements of the temperature difference spectra at fixed frequencies of 2.03 and 2.21 for the film with $T_c \approx 74$ K (see Fig. 4). The signal at a frequency of 2.03 eV, as is seen in Fig. 3, follows the variations of the continuous (background) component, but the signal at the frequency 2.21 eV sums the variations of the background component and the $A + 3J$ and $A + 4J$ peaks, which overlap at that frequency. We see that the curves diverge on cooling,
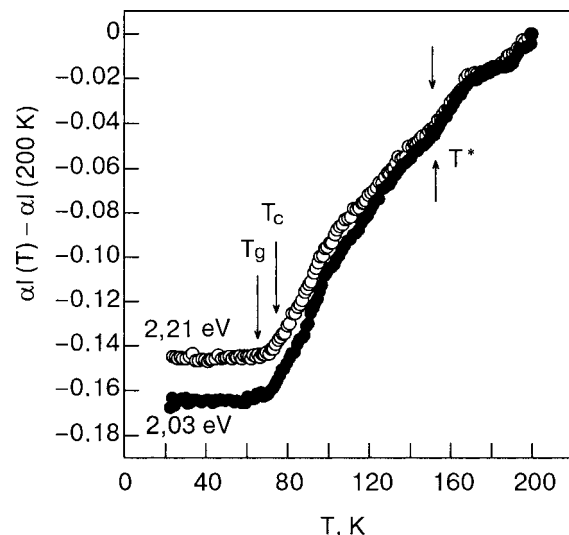

FIG. 4. Temperature variations of the absorption intensity for a metallic film of YBa$_2$Cu$_3$O$_{6+x}$ with $T_c \approx 74$ K at fixed frequencies of 2.03 eV ($\bullet$) and 2.21 eV ($\bigcirc$). The energy 2.03 eV corresponds to the background component of the spectrum, while 2.21 eV is the region of the $A + 3J$ and $A + 4J$ resonances. The divergence of the curves demonstrates the appearance of these resonances.
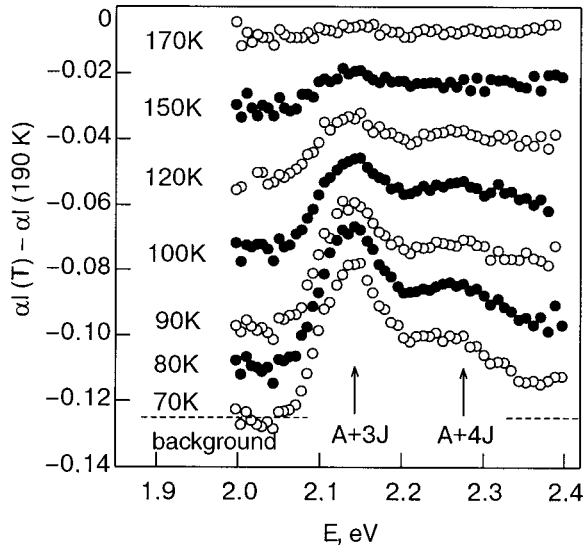
FIG. 5. Difference spectra of absorption, demonstrating the appearance of the $A+3J$ and $A+4J$ resonances on cooling of a $YBa_2Cu_3O_{6+x}$ film with $T_c \approx 74$ K.

the curve for the frequency 2.21 eV lying higher, indicating a strong increase of the $A+3J$ and $A+4J$ components. The curves begin to diverge near $T^* \approx 150$ K, which corresponds to the temperature of formation of the pseudogap state in the spectrum of AF excitations (see the neutron spectroscopy data[1]), and this divergence increases with further decrease in temperature. At $T_g = 65$–70 K, somewhat below the superconducting transition ($T_c \approx 74$ K), the temperature variations stop rather abruptly.

Figure 5 shows the temperature evolution of the whole spectral pattern $\Delta(\alpha l) = \alpha l(T) - \alpha l(190 \text{ K})$ in the region 2.0–2.4 eV for the film with $T_c \approx 74$ K. It is clearly seen that the $A+3J$ resonance, which is characteristic for an AF insulator, and a new resonance, $A+4J$, appear near 160 K. Analogous curves were obtained for the film with $T_c \approx 88$ K, where these resonances arise at a lower temperature, $T^* \approx 120$ K. Importantly, the film with $T_c \approx 88$ K also has a temperature-independent part of the absorption curve at $T < T_g = 65$–70 K. The existence of an approximately equal characteristic temperature T_g for the AF film and for the films with $T_c \approx 74$ and 88 K is evidence of the coexistence of AF and superconducting gaps.

Thus metallic films of YBCO on cooling are "shifted" toward AF ordering, and the AF spectral features arising in the pseudogap state are preserved in the superconducting phase.

5. DISCUSSION OF THE RESULTS

5.1. Features in the optical spectra

Insulating phase. The components A, $A+3J$, and $A+8J$ are characteristic of the insulating phase with short-range and long-range AF ordering. The low-energy A component lies near the edge of the optical gap and can be classed as an excitonlike feature. Analysis of the Raman scattering data showed that in a number of cuprates the scattering bands near E_g can be attributed to the existence of Zhang–Rice excitons (Ref. 23).[2] The absorption spectrum of

such an exciton[24] is most intense in the AF phase, when the Cu–O–Cu atomic configuration is close to 180°, and it can move, weakly perturbing the AF ordering.

Recently there has been heightened interest in the study of copper monoxide CuO, which is an antiferromagnet ($T_N \sim 230$ K) with strong interband transitions involving charge transfer. It has been shown[25] that these transitions are also coupled to the magnon spectrum. In CuO, as in cuprate HTSCs, a strong excitonlike band is observed at 1.8 eV at the edge of the optical gap.[25] As in our case, the continuous component of the interband transitions in CuO in the Néel phase weakens with decreasing temperature.

By virtue of momentum conservation, the excitons forming the A band, which are found at the bottom of the exciton band, interact most strongly with (are scattered by) long-wavelength magnons, which are thermally populated for $k_B T > \Delta_{AF}$. Therefore the A band is very sensitive to a change in temperature.

For classical antiferromagnets with dd transitions in the magnetic ions the existence of an exciton band has long been established, and exciton–magnon and exciton–bimagnon satellites are also observed.[19,26] For example, in classical antiferromagnets with Mn^{2+} ions (d^5 shell, $s = 5/2$) the purely exciton bands (single-ion dd transitions) are sometimes extremely weak because they are parity- or spin-forbidden, while the exciton–magnon and exciton–bimagnon satellites are well expressed. In cuprates (d^9 shell, $s = 1/2$) for electron dipole pd transitions the A band becomes dominant against the background of the pronounced exciton–bimagnon $A+3J$ band.

In Ref. 18 a microscopic picture was given for the creation of magnons at interband transitions in cuprates. According to those calculations, at the R_{2m}^2 excitation peak of the Raman spectra at energies $E_g + 8J$ the creation of an electron–hole pair occurs wherein the electron and hole in their conduction bands have approximately equal energies, $\approx 4J$ (Ref. 18). In that transition there is a large probability of creation not only of an electron and hole but also of the simultaneous appearance of two magnons at the edge of the magnetic Brillouin zone (each with energy $2J$), which are bound into a bimagnon. It can be said that the $A+8J$ absorption band is formed through the relaxation of band fermions with the emission of magnons. If the energy of the incident light lies in the region of the R_{2m}^1 peak, which coincides with the $A+3J$ resonance, then an electron and a hole will appear with zero kinetic energies, and, in addition, the creation of a bimagnon will occur.

A bimagnon is also observed in the absorption spectra in the infrared (IR) region for $E < E_g$. Here the direct optical excitation of a bimagnon (bimagnon+phonon) occurs. For example, according to the data on the IR optical conductivity and absorption spectra of the insulating phase, the bimagnon band in a number of cuprates ($YBa_2Cu_3O_6$, La_2CuO_4, and $Sr_2CuO_2Cl_2$) is located at an energy of $\approx 3J$.[27,28]

Phonons can make a certain contribution to the formation of the A, $A+3J$, and $A+8J$ absorption bands. It is known from the Raman scattering data that the transfer of charge along the Cu–O–Cu direction in the CuO_2 plane (scattering geometry B_{1g}) is strongly coupled with the magnetic excitations, but the efficiency of charge transfer in the

diagonal direction (scattering geometry B_{2g}) is determined not only by the magnetic contribution but also to a significant degree by the interaction of the interband transition with phonons.[29] The bimagnon scattering spectrum is most intense in the B_{1g} geometry.

As the temperature is lowered in the AF insulating phase the intensity at the maxima of the A, $A+3J$, and $A+8J$ absorption bands increases in both the short-range and long-range AF ordering phases. For $T>T_N$ ($T_N\approx250–300$ K) their observation can be linked to the existence of magnetic correlations of the short-range order with correlation lengths ξ. For magnetic excitations with wavelengths $\lambda<\xi$ and energies $\hbar\omega$ larger than a certain boundary energy $\Gamma=hc/\xi$ $=1.16\sqrt{2}Ja/\xi$, where a is the distance between copper spins and c is the spin-wave velocity, the spin-wave picture remains valid for $T>T_N$, and the damping of the spin excitations is insignificant.[30] For YBCO with $x\approx0.3$ (Ref. 31) the width of the neutron scattering peak $\Delta q\approx0.032$ (in units of $2\pi/a$) can be used to estimate the correlation length, which is $\leqslant15a\approx60$ Å at 200 K. The result is $\Gamma\gtrsim10$ meV, and so the thermal magnons with energies near $k_BT_N\sim30$ meV and wavelengths $\lambda_T=hc/k_BT\approx25$ Å are rather good for the spin-wave approximation. The quantity Γ can be regarded as an effective AF gap for short-range order. Since light absorption takes place over a time $\sim10^{-15}$ s, while the lifetime of the magnetic fluctuations ξ/c is much longer ($\sim10^{-13}$ s), the experiment diagnoses a quasistatic picture of the short-range AF ordering.

In the Néel phase the further enhancement of the A, $A+3J$, and $A+8J$ components occurs, with a simultaneous weakening of the long-wavelength wing of the A component on account of its narrowing; see Fig. 2. The behavior of the excitonic A absorption band is dictated by the interaction of the exciton with magnons near the real spin gap Δ_{AF}. For classical two-dimensional AF crystals it was long ago shown experimentally and theoretically that the width of the exciton bands is shaped by the factor $T\exp(-\Delta_{AF}/k_BT)$, which reflects the number of magnons near the gap Δ_{AF} (Ref. 20). As a result, the exciton band in magnetically ordered crystals narrows with decreasing temperature, and its intensity at the maximum increases. However, for $k_BT\leqslant\Delta_{AF}$ the broadening of the bands (in the general case the behavior of the integrated intensity) is blocked by the exponential factor, which leads to an almost threshold character of the transition of the absorption intensity to the temperature-independent part. Such a temperature behavior of the exciton bands has been observed, for example, in the quasi-two-dimensional AF crystal $[NH_3(CH_2)_2NH_3]MnCl_4$ and the quasi-one-dimensional AF crystal $CsMnCl_3\cdot2H_2O$. For the A band in YBCO the above-indicated temperature dependence has been verified for the region $T<T_N$ (Ref. 7) on the assumption that this band is described by a Gaussian contour. As is seen in Fig. 2, such behavior of the intensity of the long-wavelength wing of the A band, with a sharp transition to the temperature-independent part, occurs at $T_g=\Delta_{AF}/k_B$ $\approx60–70$ K. This makes it possible to estimate the value of the spin gap $\Delta_{AF}\approx6$ meV in a YBCO sample with $x\approx0.3$, which agrees with the results of other studies. For example, for the acoustic magnon mode $\Delta_{AF}\approx2.32J\sqrt{2\alpha_{xy}}$ (Ref. 32), where $\alpha_{xy}=1.5\times10^{-4}$ is the anisotropy parameter for

YBCO,[33] which gives $\Delta_{AF}\approx55$ K for $J=0.12$ eV. A close value for Δ_{AF} in YBCO is obtained, for example, from the data of Ref. 34. Below T_g there occurs a "freezing" not only of the exciton bands but also of the exciton–bimagnon A $+3J$ band, which is genetically related to it. In other words, at temperatures below the gap temperature Δ_{AF}/k_B the thermal magnetic excitations do not destroy the sublattice magnetizations, and the A and $A+3J$ bands no longer change with temperature.

In the region 60 K$<T<T_N$ in the AF phase with long-range order the amplitude of the $A+3J$ band increases with decreasing temperature at a rate $\Delta(\alpha l)/\alpha l\Delta T\approx0.8$ $\times10^{-3}$ K^{-1} (in the interval 60–200 K), although the half-width 0.06 eV remains practically unchanged. Consequently, a growth of its integrated intensity occurs, like that observed for the electron–magnon absorption in classical antiferromagnets, e.g., in $FeCO_3$ (Ref. 26). The integrated Raman scattering intensity for the $3J$ two-magnon band in the B_{1g} geometry in cuprates behaves in the opposite way: it decreases with decreasing temperature. A fall of the integrated intensity of the two-magnon Raman scattering band is also observed in classical antiferromagnets.[26] The decrease in the intensity in Raman scattering experiments in $EuBa_2Cu_3O_6$, La_2CuO_4, and $PrBa_2Cu_3O_7$, for example, occurs primarily on account of a severalfold narrowing of the band as a result of a decrease of the magnon damping.[29,35,36] Such a comparison suggests that the $3J$ bimagnon Raman scattering band is significantly more sensitive to the magnon damping than is the exciton–bimagnon $A+3J$ absorption band, the area of which is proportional to the oscillator strength of the transition. It can be assumed that the $A+3J$ band follows the temperature behavior of the mean magnetization, i.e., the AF order parameter, unlike the Raman scattering, which primarily follows decay processes involving magnons.

Metallic phase. With increasing doping index x and the transition to the metallic phase at 300 K, the A and $A+3J$ bands begin to weaken rapidly; this can be attributed to a decrease in the correlation length $\xi\sim1/\sqrt{x}$ and a decrease of the mean fluctuation magnetization $\langle M\rangle$. Since mobile carriers increase the degree of noncollinearity of the AF sublattices, the decrease of the exciton–bimagnon band can also be considered to be a consequence of an increase in the noncollinearity of the lattices over the correlation length.[19] A peak-shaped A band is detected in samples with $T_c\leqslant50$ K (x $\leqslant0.5$). According to the neutron data,[37] in samples with T_c ≈50 K the correlation length $\xi\approx10$ Å at 300 K. In samples with large x, when $\xi_c<\xi_T$ and the "instantaneous" magnetization can be assumed zero, the A and $A+3J$ bands are absent at room temperatures.[6] In the Raman scattering spectra the bimagnon band weakens rapidly with doping;[13] this may be attributed to an increase in the damping of the magnons as as result of their interaction with free carriers. In the room-temperature absorption spectra the band near 2.8 eV, due to interband transitions, is nevertheless present, since the optical gap is preserved.

An important point for our further discussion is the fact that, as can be seen in Figs. 3 and 5, when the metallized samples are cooled below T^* the A and $A+3J$ bands and an additional $A+4J$ band appear clearly, and the temperature dependence of the $A+8J$ band is even stronger than in the
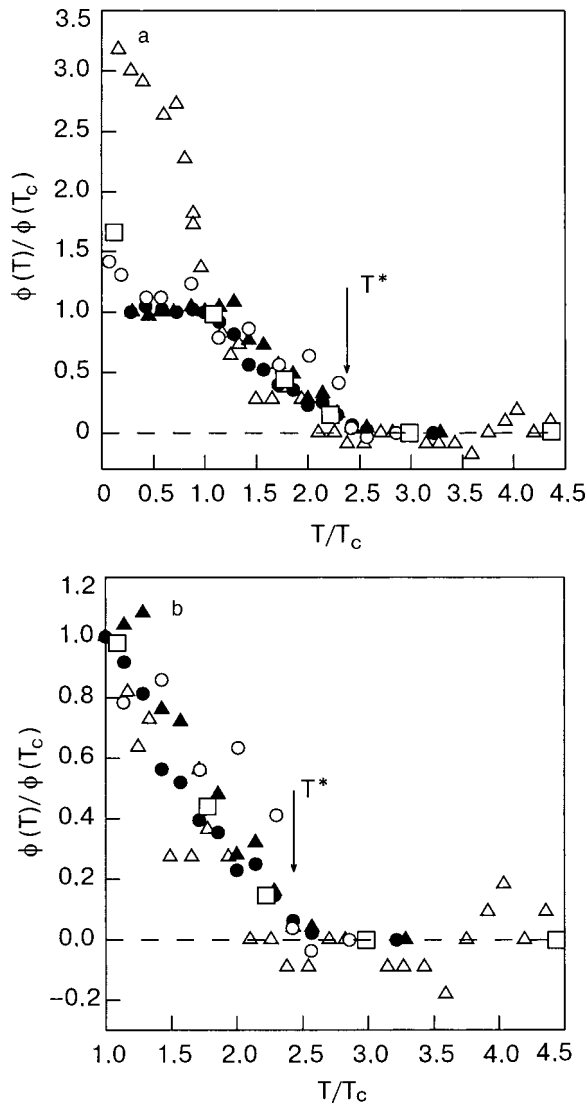
FIG. 7. Correlation of the optical and neutron data for superconducting samples of YBa$_2$Cu$_3$O$_{6+x}$ with $T_c = 81$–88 K. The intensity of $A + 3J$ and $A + 4J$ resonances according to the data of the present study (●, ▲); the peak intensity of the magnetic (π,π) resonance at 39 meV according to the inelastic neutron scattering data[1] (△).

FIG. 6. Correlation of optical, neutron, and muon data for superconducting samples of YBa$_2$Cu$_3$O$_{6+x}$ with $T_c = 68$–74 K. The intensity of the $A + 3J$ and $A + 4J$ resonances: data of the present study (●, ▲); the integrated (□) and peak (△) intensities of the magnetic (π,π) resonance at 34 meV from the inelastic neutron scattering data;[1] the behavior of the muon spin relaxation rate (○) according to the data of Ref. 2. The temperature variations in the region $T < T^*$, which includes the pseudogap and superconducting states (a), and in the region $T_c < T < T^*$ (b).

insulating phase. A result, we are compelled to attribute the onset of these bands to the appearance of a fluctuational AF order parameter.

5.2. Comparison with the neutron and muon spectroscopy data. Pseudogap and superconducting states

The temperature data of optical, neutron, and muon experiments for YBCO samples with different T_c is discussed below. To establish the correlation between the data of these three independent experiments we have presented them in Figs. 6a and 6b and 7 in the reduced coordinates $\phi(T)/\phi(T_c)$. Plotted along the abscissa is the temperature in units of T_c, and along the ordinate—the results of temperature measurements normalized to their value at T_c.

These figures show the following data: 1) the intensities I_{3J} and I_{4J} of the $A + 3J$ and $A + 4J$ absorption components (we are actually discussing the temperature dependence of
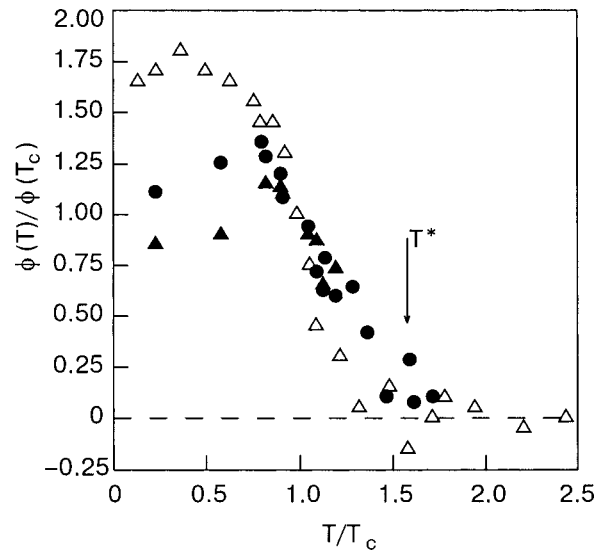
the integrated intensities, since the half-width of the bands is slowly varying); 2) the peak intensity I_{res} of the magnetic (π,π) resonance near 40 meV, measured in the neutron experiments,[1] and also the mean square fluctuational magnetic moment $\langle m_{res}^2 \rangle$ associated with this resonance; 3) the rates λ of muon-spin relaxation[2] due to the magnetic field around the muon (the dynamic Kubo–Toyabe factor).

Figure 6a and 6b shows the results for YBCO samples in the ortho-II phase with the following values of the superconducting transition temperature: $T_c \approx 74$ K (absorption data), $T_c \approx 68$ K ($x = 0.6$; neutron data), and $T_c \approx 70$ K ($x = 0.67$; muon data). Figure 6a shows the data for a wide temperature interval, from ≈ 250 to ≈ 10 K, including both the pseudogap state ($T_c < T < T^*$) and the superconducting state ($T < T_c$), and Fig. 6b shows the region from ≈ 250 K to T_c on an expanded scale.

Figure 7 shows the results for the ortho-I phase with $T_c \approx 88$ K (absorption data) and $T_c \approx 82$ K ($x = 0.8$; neutron data). The temperature interval corresponds to ≈ 200–10 K. (In Refs. 2 and 3 the data from muon measurements of $\lambda(T)$ are given only for the ortho-II phase with $x \approx 0.67$ and the overdoped compound $x \approx 0.95$).

Before discussing the figures, let us briefly remark on the essentials of the neutron and muon measurements. The observation in the neutron experiments of a narrow magnetic (π,π) resonance, which reflects the development of commensurate AF fluctuations, is an important result in the physics of HTSCs. This resonance has been registered in YBa$_2$Cu$_3$O$_{6+x}$, with two CuO$_2$ planes per unit cell,[1] and also recently in Tl$_2$Ba$_2$CuO$_{6+\delta}$ (Ref. 5), with one plane per cell. This suggests that the given magnetic resonance may be a general feature of cuprate HTSCs. On cooling the resonance arises for an acoustic mode at energies somewhat higher than the energy of the spin pseudogap. For example, for YBCO with $T_c \approx 74$ K the value of the spin pseudogap is ≈ 26 meV in the superconducting phase, while the resonance is at 37 meV; for the sample with $T_c \approx 82$ K the pseudogap is

30 meV and the resonance is at 39 meV.[38] The intensity $I_{res}(\omega)$ of the resonance is directly related to the imaginary part of the magnetic susceptibility $\chi''(\omega) \sim I_{res}(\omega)$. Using the fluctuation dissipation theorem, one can obtain the mean square fluctuational magnetic moment by integrating over the resonance contour:

$$\langle m_{res}^2 \rangle = 3/(2\pi) \int d(h\omega) \chi''_{res}(\omega)/[1 - \exp(-h\omega/kT)],$$

as was done in Ref. 1. Figure 6a shows the temperature dependence of both $I_{res}(T)/I_{res}(T_c)$ (unfilled triangles) and $\langle m_{res}^2 \rangle (T)/\langle m_{res}^2 \rangle (T_c)$ (unfilled squares) for $x \approx 0.6$. At 35 K the absolute values are $\langle m_{res}^2 \rangle = (0.06 \pm 0.04)\mu_B^2$ per cell.[1] It was difficult to measure the temperature dependence $\langle m_{res}^2 \rangle \times (T)$ for the sample with index $x \approx 0.8$ (Fig. 7), since the magnetic resonance above T_c at these indices is rather weak, and therefore only the behavior of the peak intensity is shown in Fig. 7.

In the muon experiments,[2] polarized muons were embedded in YBCO samples and the relaxation of their spin polarization, $P(t) = G_{KT}(t)\exp[-\lambda(T)t]$, was measured in zero magnetic field. The Kubo–Toyabe relaxation function $G_{KT}(t)$ reflects the existence of randomly oriented static magnetic fields from the nuclear dipoles and depends weakly on temperature, while the exponential factor describes relaxation due to the additional magnetic field from the electron spins around the muon. The normalized temperature dependence $\lambda(T)/\lambda(T_c)$ in Figs. 6 and 7 is shown by the unfilled circles; here the absolute value of λ for $T < T_c$ was ≈ 0.012 μs.

We can now turn to a more detailed analysis of the data in Figs. 6 and 7. Let us first point out that as the temperature is lowered, the rise of the $A + 3J$ and $A + 4J$ resonances at $T = T^*$, the increase in the parameter λ, and the growth of both the integrated and peak magnetic resonance intensities are well correlated with one another. The observed agreement at temperatures below $T/T_c \approx 2.3$ (ortho-II phase) and $T/T_c \approx 1.5$ (ortho-I phase)[3] suggests an interpretation as the development of AF correlations in the pseudogap region. In that case the short-range AF order should be characterized by rather large correlation lengths and a slight noncollinearity of the lattice, since the A, $A + 3J$, and $A + 4J$ components are manifested, in the same way as the A and $A + 3J$ components exist in the insulating phase at $T > T_N$. It should also be noted that the half-widths of the $A + 3J$ and $A + 4J$ bands in the metal, equal to approximately 0.06 eV, are practically equal to the half-width of the $A + 3J$ band in the AF insulator phase. It is also seen in Figs. 6 and 7 that in the superconducting state the optical, muon, and integrated neutron data demonstrate a sharp decrease in the rate of growth of the signals I_{3J}, I_{4J}, λ, and $\langle m_{res}^2 \rangle$ with temperature, with a clear tendency toward saturation. Thus the AF fluctuations are preserved in the superconducting phase, where they coexist with the superconducting condensate.

Figure 6 shows rather unambiguously that in the entire temperature region $T < T^*$, including in the superconducting state, the results analyzed here satisfy the scaling relation

$$\frac{I_{3J,4J}}{I_{3J,4J}(T_c)} \approx \frac{\langle m_{res}^2 \rangle}{\langle m_{res}^2 \rangle (T_c)} \approx \frac{\lambda(T)}{\lambda(T_c)} = f\left(\frac{T}{T_c}\right), \tag{1}$$

where for $T < T_c$ the function $f(T/T_c) \approx$ const within the error limits of the three techniques.

Since the AF fluctuations can be attributed to stripe ordering,[39] let us consider the optical data from that point of view. That the development of AF fluctuations occurs in the regime of phase separation into insulating and metallic regions is evidence of the simultaneous appearance of the $A + 3J$ resonance for interacting magnons (a bimagnon) and the $A + 4J$ resonance, which can be attributed to magnons that do not interact with each other. The resonance $A + 4J$ arises in a natural way if the AF region is divided by metallic regions (which are antiphase charged domain walls in the framework of the stripe model; see, e.g., Ref. 40). As was shown theoretically in Ref. 40, the value of the exchange energy through such a wall is only $\sim 0.1J$, which sharply curtails the interaction of magnons created in neighboring insulating AF stripes (the $A + 4J$ resonance). If the AF regions are long "vertical" quasi-one-dimensional stripes, then the spin-wave velocity (exchange energy) along the stripes will be the same as in the ordered AF phase (this situation is apparently realized in cuprates[40]). In this case bimagnons with energy $3J$ can be excited within the same insulating region. Then the correlation length along these stripes, $\xi_\parallel$ (for $T < T^*, T_c$), must be rather large (several tens of angstroms) in order to give the same picture of the optical A and $A + 3J$ signals as in the phase of long-range AF ordering or in the fluctuation phase of short-range order above T_N. In addition, even in the superconducting state the transition of the optical signals to a temperature-independent part occurs just as abruptly and at approximately the same temperature T_g as in the AF insulator phase. This circumstance can be interpreted as evidence of the existence of an AF gap in the AF stripes, this gap coexisting with the superconducting gap in the sample. The transverse AF correlation length can be small, $\xi_\perp \ll \xi_\parallel$, spanning only a few lattice constants. From the width of the (π,π) resonance peak, which evidently tracks the shorter correlation length, one can estimate $\xi_\perp$. Such an analysis[40] shows that the distance between interphase boundaries is 4–5 lattice constants in the copper subsystem.

It is possible that the formation of the $A + 4J$ band contains contributions from multimagnon processes and from magnetic quantum fluctuations, the manifestation of which in Raman scattering experiments and in IR experiments on the study of bimagnon resonances in cuprate HTSCs was considered in Refs. 27 and 28. For interband absorption the role of these contributions requires a special theoretical treatment, especially for stripe ordering.

In the neutron experiments an important piece of evidence for the stripe structure is the appearance of inelastic peaks corresponding to neutron scattering on the AF fluctuations incommensurate with the lattice period.[41]

As to the interpretation of the behavior of $\lambda(T)$ and its connection with the development of the stripe structure, this question has not yet been definitively answered. In the general case, by analogy with the nuclear magnetic resonance, the dynamic relaxation time is usually written as $\lambda(T) = \gamma_\mu^2 \langle B^2 \rangle \tau/[1 + (\omega\tau)^2]$, where γ_μ is the gyromagnetic constant for the muon, $\langle B^2 \rangle$ is the mean square value of the fluctuating transverse components of the magnetic field, and

τ is their mean correlation time, which is strongly temperature dependent.[42] As the temperature is varied, one can observe a maximum of $\lambda(T)$ when $\omega\tau\approx1$, e.g., in $La_{2-x}Sr_xCuO_4$, which has been interpreted as the appearance of a spin glass state.[42] As is seen in Fig. 6, no such maximum is observed. Behavior of $\lambda(T)$ analogous to that shown in Fig. 6 has also been observed in studies of antiferromagnetism in borides,[43] small AF clusters in the heavy-fermion system URu_2Si_2 (Ref. 44), and the dynamics of the stripe structure in $La_{2-x}Sr_xCu_{1-y}Zn_yO_4$ (Ref. 45). Such an analogy indicates that $\lambda(T)$ is sensitive to the development of antiferromagnetism and stripe structure. In this regard the rather good agreement of the behavior of $\lambda(T)$ and $\langle m_{res}^2 \rangle$, it seems to us, merits a special analysis.

In the framework of the stripe picture it is especially interesting to examine muon experiments with compounds based on heavy fermions. In the superconducting material URu_2Si_2 in the low-temperature phase of weak antiferromagnetism for $T<T_N=17.5$ K one observes an increase of λ with a subsequent rather rapid transition to the temperature-independent part.[44] Such behavior occurs on the "doorstep" of the superconducting transition at $T_c=1.2$ K. Comprehensive studies[44] show that in this compound $\lambda(T)$ reflects the behavior of small AF clusters. In that case, as was established a comparatively long time ago,[46] a gap feature with a value of approximately 65 cm^{-1} appears in the spectrum of spin excitations below T_N. All these processes take place in a coherent metallic phase observed below $T\approx50$ K.[46] Thus the indicated $\lambda(T)$ dependence reflects phase separation in URu_2Si into AF and metallic regions.

Another point that we think merits discussion is the different temperature trend of the peak I_{res} and integrated $\langle m_{res}^2 \rangle$ intensities of the (π,π) resonance. As is seen in Fig. 6, in the pseudogap state at $T_c<T<T^*$ both intensities have the same temperature dependence. Below T_c, however, the peak intensity continues to increase with decreasing temperature, while the temperature variation of the integrated intensity decreases sharply. The difference becomes especially noticeable if the neutron data are normalized to their value at T_c, as is done in Figs. 6 and 7. This difference can be explained by different temperature dependence of the peak intensity and width of the (π,π) resonance. If it is assumed that in the region $T_c<T<T^*$ only the intensity changes, while the width of the resonance remains practically unchanged, then one would expect the same trend of I_{res} and $\langle m_{res}^2 \rangle$. If a strong narrowing of the resonance occurs below T_c, then the integrated intensity will have weaker temperature behavior than the peak intensity. In fact it is seen from the data of Ref. 1 that the half-width of the resonance peak decreases by more than a factor of two as a result of the transition to the superconducting phase (the authors of Ref. 47 estimated $\hbar\gamma\approx10$ meV at 20 K). The decrease in γ can be attributed to the effect wherein the lifetime of AF fluctuations increases in the superconducting phase. In YBCO with a Zn impurity,[48] when the superconductivity is suppressed and the dynamic stripe structure is pinned, a broadening rather than a narrowing of the magnetic resonance peak at the superconducting transition is observed.[49]

Let us say a few words about the nature of the carriers in the stripe state. As we have said, the optical spectrum of the insulating phase at $x\approx0.3-0.35$ near the insulator–metal transition is formed under conditions in which localized carriers exist. It is known that localized carriers destroy the AF phase on account of their thermal promotion to the mobility level.[19,50] These localized carriers can have an appreciable polaron (polaron–magnon) component of the spectrum.[51,52] As a result, under conditions of phase separation one can assume the coexistence of two types of particles: heavy polarons in the bulk of the insulating regions, and light fermions in the conducting regions. In IR experiments on YBCO[52] such a coexistence is reflected in the two components of the spectra of the optical conductivity, which are most pronounced for $T<T^*$. We are talking about the rather narrow Drude component of the light carriers, which lies in the energy region below 500 cm^{-1}, and also an asymmetric, wide polaron component, with a maximum near 1200–2000 cm^{-1} (0.15–0.25 eV). These two components are also observed simultaneously for Bi and La cuprates.[52] In the optical absorption spectra of YBCO near E_g the band near 1.5 eV, which reflects the degree of metallization of the system, is enhanced with doping.[6] It is further enhanced with decreasing temperature in the region below T^*. This band coexists with the A, $A+3J$, and $A+4J$ components, apparently also reflecting the coexistence of light hole carriers in the metallic regions and heavy hole carriers in the AF regions.

6. CONCLUSIONS

1. On cooling of metallic superconducting YBCO films, both weakly doped and close to optimally doped, bands appear in the absorption spectra: an A band (at ≈1.8 eV, close to the optical gap E_g with charge transfer), an $A+3J$ band, and an $A+4J$ band, where $J\approx0.12$ eV is the exchange interaction constant. These bands arise in the temperature region $T_c<T<T^*$, which is known in the literature as the region of the pseudogap state in the spectrum of magnetic excitations.

2. It is found that for $T<T^*$, including the superconducting state, the temperature behavior of the integrated intensities $I_{3J,4J}$ of the $A+3J$ and $A+4J$ absorption components is very well correlated with the neutron data on the temperature evolution of the mean square fluctuational magnetic moment $\langle m_{res}^2 \rangle$ associated with the (π,π) resonance and also with the data on the muon dynamic spin relaxation $\lambda(T)$. The behavior of the optical, neutron, and muon data in the reduced coordinates satisfy scaling relation (1) in the form of a function $f(T/T_c)$ which in the superconducting phase depends weakly on temperature and is close to unity.

3. The discussion has shown that below T^* there is a growth of the antiferromagnetic correlations with the formation of a stripe state of AF (insulating) and metallic stripes. For samples with $T_c\approx70$ and 88 K the phase separation temperatures are $T^*\approx2.3T_c$ and $1.5T_c$, respectively. The AF correlations and stripe state are preserved in the superconducting state. The optical data suggest that in the superconducting state there is an AF gap of about the same value as in the insulator.

4. The observed absorption components A and $A+3J$ are attributed to a manifestation of exciton and exciton–bimagnon resonances, which exist both in the AF-ordered insulator and in the stripe state. The component $A+4J$ ap-

pearing in the stripe state is attributed to the excitation of two magnons which interact weakly with each other across a conducting antiphase domain wall.

5. The A, $A+3J$, and $A+4J$ components, which are located near the fundamental Hubbard gap with charge transfer, can be used efficiently for diagnostics of the stripe ordering in both the normal and superconducting phases. In terms of its sensitivity to AF correlations, optical spectroscopy of the $A+3J$ and $A+4J$ resonances is comparable to neutron and muon spectroscopy.

Optical studies of the behavior of these components in a magnetic field are undoubtedly of interest. First, a magnetic field causes noncollinearity of the AF sublattices, which should have a substantial influence on the integrated intensities of these bands; second, a magnetic field, depending on its strength, has different effects on the stripe and superconducting states and also on the magnetic (π,π) resonance.[38,53] Optical experiments with a magnetic field allow one to make more-informative use of the ''magnetic'' components of the absorption at interband transitions for studying the pseudogap, stripe, and superconducting states in copper oxides.

[*]E-mail: samovarov@ilt.kharkov.ua
[1)]The films were grown by the laser ablation method at the Physics Institute of the University of Erlangen, Germany.
[2)]Besides excitons at the interionic transitions in cuprates in the infrared region, excitons can also be manifested at single-ion dd transitions, which can have dipole-allowed absorption bands because of pd hybridization [V. M. Loktev, Fiz. Nizk. Temp. **20**, 173 (1994) [Low Temp. Phys. **20**, 139 (1994)].
[3)]The neutron data show that on cooling of YBCO with $T_c \approx 91-92$ K, the growth of I_{res} occurs practically at T_c (Ref. 1).

[1]Pengcheng Dai, H. A. Mook, S. M. Hayden, G. Aeppli, T. G. Perring, R. D. Hunt, and F. Dogan, Science **284**, 1344 (1999).

[2]J. E. Sonier and J. H. Brewer, Physica B **312–313**, 77 (2002).

[3]J. E. Sonier, J. H. Brewer, R. F. Kiefl, R. I. Miller, G. D. Morris, C. E. Stronach, J. S. Gardner, S. R. Dunsiger, D. A. Bonn, W. N. Hardy, R. Liang, and R. H. Heffner, Science **292**, 1692 (2001).

[4]T. Timusk and C. C. Homes, cond-mat/0209371.

[5]Ph. Bourges, B. Keimer, S. Pailhès, L. P. Regnault, Y. Sidis, and C. Ulrich, cond-mat/0211227.

[6]V. V. Eremenko, V. N. Samovarov, V. N. Svishchev, V. L. Vakula, M. Yu. Libin, S. A. Uyutnov, Fiz. Nizk. Temp. **26**, 739 (2000) [Low Temp. Phys. **26**, 541 (2000)]; V. V. Eremenko, V. N. Samovarov, V. L. Vakula, M. Yu. Libin, and S. A. Uyutnov, Fiz. Nizk. Temp. **26**, 1091 (2000) [Low Temp. Phys. **26**, 809 (2000)].

[7]V. N. Samovarov, V. L. Vakula, M. Yu. Libin, S. A. Uyutnov, and G. G. Sergeeva, Fiz. Nizk. Temp. **28**, 934 (2002) [Low Temp. Phys. **28**, 674 (2002)].

[8]S. L. Cooper, G. A. Thomas, A. J. Millis, P. E. Sulewski, J. Orenstein, D. H. Rapkine, S.-W. Cheong, and P. L. Trevor, Phys. Rev. B **42**, 10785 (1990); M. Imada, A. Fujimori, and Y. Tokura, Rev. Mod. Phys. **70**, 1040 (1998).

[9]S. H. Blanton, R. T. Collins, K. H. Kelleher, L. D. Rotter, Z. Schlesinger, D. G. Hinks, and Y. Zheng, Phys. Rev. B **47**, 996 (1993).

[10]I. Fugol, V. Samovarov, A. Ratner, V. Zhuravlev, G. Saemann-Ischenko, B. Holzäpfel, and O. Meyer, Solid State Commun. **86**, 385 (1993).

[11]Yu. B. Gaididei and V. M. Loktev, Fiz. Nizk. Temp. **18**, 135 (1992) [Low Temp. Phys. **18**, 92 (1992)]; J. E. Hirsch, Physica C **364–365**, 37 (2001).

[12]R. Liu, M. V. Klein, D. Salamon, S. L. Cooper, W. C. Lee, S.-W. Cheong, and D. M. Ginsberg, J. Phys. Chem. Solids **54**, 1347 (1993).

[13]G. Blumberg, R. Lin, M. V. Klein, W. C. Lee, D. M. Ginsberg, C. Gu, B. W. Veal, and B. Dabrowski, Phys. Rev. B **49**, 13295 (1994); G. Blumberg, Moonsoo Kang, M. V. Klein, K. Kadowaki, and C. Kendziora, Science **278**, 1427 (1997).

[14]M. J. Holcomb, C. L. Perry, J. P. Collman, and W. A. Little, Phys. Rev. B **53**, 6734 (1996).

[15]A. I. Kirilyuk, N. M. Kreĭnes, and V. I. Kudinov, JETP Lett. **52**, 49 (1990).

[16]V. P. Gnezdilov, V. V. Eremenko, and V. I. Fomin, Fiz. Nizk. Temp. **17**, 828 (1991) [Sov. J. Low Temp. Phys. **17**, 432 (1991)].

[17]J. Lorenzana and G. A. Sawatzky, Phys. Rev. B **52**, 9576 (1995).

[18]A. V. Chubukov and D. M. Frenkel, Phys. Rev. B **52**, 9760 (1995); D. K. Morr and A. V. Chubukov, cond-mat/9705051.

[19]É. G. Petrov, *Theory of Magnetic Excitons* [in Russian], Naukova Dumka, Kiev (1976); V. V. Gorbach M. G. Ostapenko, and E. G. Petrov, Solid State Commun. **83**, 361 (1992).

[20]A. V. Eremenko, I. S. Kachur, V. G. Piryatinskaya, and V. V. Slavin, Fiz. Nizk. Temp. **18**, 380 (1992) [Low Temp. Phys. **18**, 258 (1992)].

[21]G. Yu, C. H. Lee, A. J. Heeger, N. Herron, E. M. McCarron, Lin Cong, G. C. Spalding, C. A. Nordman, and A. M. Goldman, Phys. Rev. B **45**, 4964 (1992).

[22]V. V. Eremenko, V. N. Samovarov, V. L. Vakula, M. Yu. Libin, S. A. Uyutnov, and V. M. Rashkovan, Fiz. Nizk. Temp. **27**, 1327 (2001) [Low Temp. Phys. **27**, 981 (2001)].

[23]M. E. Simòn, A. A. Aligia, C. D. Batista, E. R. Gagliano, and F. Lema, Phys. Rev. B **54**, R3780 (1996); F. C. Zhang and K. K. Ng, *ibid.* **58**, 13520 (1998).

[24]S. Pagliara, F. Parmigiani, P. Galinetto, A. Revcolevschi, and G. Samoggia, Phys. Rev. B **66**, 024518 (2002).

[25]Yu. P. Sukhorukov, A. S. Moskvin, N. N. Loshkareva, A. S. Ovchinnikov, A. A. Samokhvalov, and S. V. Naumov, JETP Lett. **63**, 267 (1996).

[26]V. V. Eremenko, N. F. Kharchenko, Yu. G. Litvinenko, and V. M. Naumenko, *Magneto-Optics and Spectroscopy of Antiferromagnets*, Springer-Verlag, Berlin (1992).

[27]M. Grüninger, D. van der Marel, A. Damascelli, A. Erb, T. Nunner, and T. Kopp, Phys. Rev. B **62**, 12422 (2000).

[28]J. Lorenzana, J. Eroles, and S. Sorella, Phys. Rev. **83**, 5122 (1999).

[29]S. Sugai, N. Hayamizu, and T. Hozokawa, cond-mat/0010472; S. Sugai and N. Hayamizu, cond-mat/0010305.

[30]A. Singh and Z. Tešanović, Phys. Rev. B **45**, 7258 (1992).

[31]J. M. Tranquada, G. Shirane, B. Keimer, S. Shamoto, and M. Sato, Phys. Rev. B **40**, 4503 (1989).

[32]V. G. Bar'yakhtar, V. M. Loktev, and D. A. Yablonskii, Physica C **156**, 667 (1988).

[33]B. Keimer, A. Aharony, A. Auerbach, R. J. Birgeneau, A. Cassanho, Y. Endoh, R. W. Erwin, M. A. Kastner, and G. Shirane, Phys. Rev. B **45**, 7430 (1992).

[34]Ph. Bourges, cond-mat/9901333.

[35]P. Knoll, C. Thomsen, M. Cardona, and P. Murugaraj, Phys. Rev. B **42**, 4842 (1990).

[36]M. Rübhausen, N. Dieckmann, A. Bock, U. Merkt, W. Widder, and H. F. Braun, Phys. Rev. B **53**, 8619 (1996).

[37]B. J. Sternlieb, G. Shirane, J. M. Tranquada, M. Sato, and S. Shamoto, Phys. Rev. B **47**, 5320 (1993).

[38]P. Dai, H. A. Mook, R. D. Hunt, and F. Dogan, cond-mat/0011019.

[39]A. Bianconi, D. Di Castro, G. Bianconi, A. Pifferi, N. L. Saini, F. C. Chou, D. C. Johnston, and M. Colapietro, Physica C **341–348**, 1719 (2000).

[40]F. Krüger and S. Scheidl, cond-mat/0211593.

[41]J. M. Tranquada, B. J. Sternlieb, J. D. Axe, Y. Nakamura, and S. Uchida, Nature (London) **375**, 561 (1995); V. J. Emery, S. A. Kivelson, and J. M. Tranquada, cond-mat/9907228.

[42]Ch. Niedermayer, C. Bernhard, T. Blasius, A. Golnik, A. Moodenbaugh, and J. I. Budnick, Phys. Rev. Lett. **80**, 3843 (1998).

[43]J. Satooka, Y. Kojima, S. Miyata, K. Suzuki, W. Higemoto, K. Nishiyama, and K. Nagamine, Physica B **326**, 585 (2003).

[44]H. Amitsuka, M. Yokoyama, S. Miyazaki, K. Tenya, T. Sakakibara, W. Higemoto, K. Nagamine, K. Matsuda, Y. Kohori, and T. Kohara, Physica B **312–313**, 390 (2002).

[45]I. Watanabe, T. Adachi, S. Yairi, Y. Koike, and K. Nagamine, Physica B **326**, 305 (2003).

[46] D. A. Bonn, J. D. Garret, and T. Timusk, Phys. Rev. Lett. **61**, 1305 (1988).

[47] D. Munzar, C. Bernhard, and M. Cardona, Physica C **317−318**, 547 (1999).

[48] I. Watanabe, M. Aoyama, M. Akoshima, T. Kawamata, T. Adachi, Y. Koike, S. Ohira, W. Higemoto, and K. Nagamine, Phys. Rev. B **62**, R11985 (2002).

[49] Y. Sidis, P. Bourges, B. Keimer, L. P. Regnault, J. Bossy, A. Ivanov, B. Hennion, P. Gautier-Picard, and G. Collin, cond-mat/0006265.

[50] I. Ya. Korenblit and A. Aharony, Phys. Rev. B **49**, 13291 (1994).

[51] G. G. Sergeeva and V. L. Vakula, cond-mat/0301037.

[52] D. Mihailovic, T. Mertelj, and K. A. Müller, Phys. Rev. B **57**, 6116 (1998).

[53] P. Pieri, G. C. Strinati, and D. Moroni, Phys. Rev. Lett. **89**, 127003 (2002).

Translated by Steve Torstveit

Barrier properties of superconducting structures based on niobium nitride and a molybdenum–rhenium alloy

V. E. Shaternik*

G. V. Kurdyumov Institute of Metal Physics, National Academy of Sciences of Ukraine, pr. Vernadskogo 36, 03142 Kiev, Ukraine

M. A. Belogolovskiĭ

A. A. Galkin Donetsk Physicotechnical Institute, ul. R. Lyuksemburg 72, 83114 Donetsk, Ukraine

Stable superconducting structures of the metal–insulator–metal type are made using niobium nitride. A comparison of the measured current–voltage characteristics with the theoretical curves calculated with allowance for possible fluctuations in the transparency of the insulating spacer layer shows that the potential barrier formed as a result of the oxidation of NbN is quite uniform. The possibility of making niobium nitride Josephson junctions for superconducting micro- and nanoelectronics is discussed. © *2003 American Institute of Physics.*
[DOI: 10.1063/1.1630714]

The most important question facing microelectronics right now is the creation of quantum devices with nanometer dimensions. A European Union analysis of the development of of nanoelectronics in the next 10 years[1] points out that of all the proposed schemes, superconducting fast single-quantum logic, the basic element of which is a Josephson junction, has the highest rate (100 GHz and higher) and the least power dissipation (1 μW per element). At the same time, superconducting micro- and, even more so, nanoelectronics have not found wide use. The authors of the review[1] surmise that the main obstacle lies in the need for cooling the niobium junctions down to a temperature of the order of 4 K, which requires either liquid helium or a three-stage cryorefrigerator. Replacing the pure niobium by niobium nitride, the superconducting transition temperature of which is twice as high, allows one to go to a temperature of the order of 10 K, so that two-stage cryorefrigerators may be used.[1] If such a transition comes to pass it will radically advance superconducting electronics, but, according to Ref. 1, the present-day technology of fabricating tunneling structures based on niobium nitride remains insufficiently developed. The goal of our research is to create stable metal–insulator–metal junctions based on NbN and to interpret the measured current–voltage characteristics.

The analysis of the corresponding experimental curves was directed primarily toward elucidating the nature of the insulating layer that forms as a result of the oxidation of NbN. From an applied standpoint, the main problem in creating Josephson junctions is to obtain sufficiently uniform and reproducible tunnel barriers. It should be noted that the properties of ultrathin insulating spacer layers formed through an oxidation reaction of one of the electrodes differ quite strongly from one another. For example, it has been found experimentally and confirmed theoretically[2] that SiO_2 layers thermally grown on the silicon surface already have all the properties of the bulk material at thicknesses of the order of 0.8 nm and are rather uniform over thickness. On

the contrary, barriers of aluminum oxide formed at room temperature come out much more disordered. As was shown in Ref. 3, the formation of an oxide layer leads to hybridization of its electronic states with states of the electrodes, as a result of which conducting channels appear within the oxide, leading to a local decrease of the barrier parameters and, hence, to a substantial scatter in the barrier heights. Studies[4] with an atomic force microscope have shown that this scatter in the barrier heights is more important than the variations of the thickness of the insulator. As far as we know, no analysis of the spatial distribution of the probability of tunneling through the barrier formed as a result of the oxidation of one of the metallic electrodes has yet been done; such an analysis is the main goal of this paper.

We studied film structures of the injector–insulator–superconductor type, in which a film of lead 300–500 nm thick or a film of a molybdenum–rhenium alloy MoRe was used as the injector, and the material to be investigated was a thin (around 100 nm) layer of niobium nitride. The layers were formed by the reactive cathode sputtering of a niobium target in an atmosphere of argon and nitrogen, with a subsequent deposition of the compound obtained on a heated sapphire substrate. The tunnel barrier was created by thermic oxidation of the NbN, after which a lead or MoRe film was deposited on top. The current–voltage characteristics $I(V)$ of the samples and their derivatives with respect to voltage were measured by the four-probe method with the use of the standard technique of detection of harmonics at temperatures from 1.5 K to room temperature. The normal-state resistance R_N of the structures was 0.1–1 Ω.

Let us now turn to the form of the current–voltage characteristic in the region of voltages equal to the sum of the energy gaps of the superconducting facings. The standard theory of tunneling in structures formed by two superconductors S_1 and S_2 separated by an insulating layer I proceeds from the assumption of a uniform barrier with a very low transparency T and predicts sharp growth of the current in
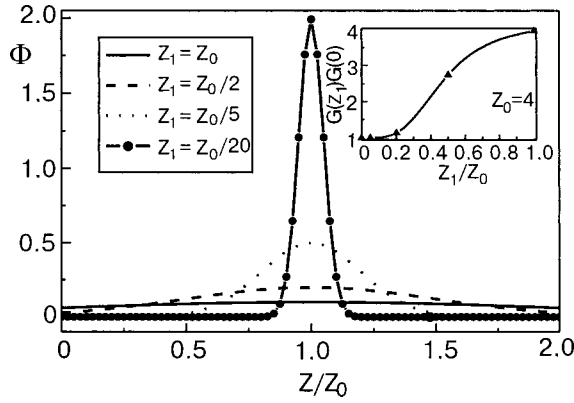
FIG. 1. Distribution function $\Phi(Z)$ [Eq. (3)] of the parameter Z [Eq. (1)] describing the effectiveness of the potential barrier at values of the parameter $Z_1 = Z_0$, $Z_0/2$, $Z_0/5$, and $Z_0/20$. The inset shows the dependence on Z_1 of the normalized conductance of the tunnel junction in the normal state. The calculations were done for a mean value $Z_0 = 4$.

the vicinity of the sum of the two energy gaps, $V^* = (\Delta_{S_1} + \Delta_{S_2})/e$.[5] We indeed observed a rise of the current I, but over a rather wide range of voltages, which may be due, first, to the finite transparency of the potential barrier separating the two conductors. Further, following Ref. 6, we shall assume that the insulating layer with the repulsive potential $V(x)$ is very thin, and we shall therefore describe it by the parameter

$$Z = k_F \int V(x)dx/\varepsilon_F, \qquad (1)$$

where the x axis is directed along the normal to the barrier, and k_F and ε_F are the Fermi wave vector and energy. The transparency of such a junction in the normal N state has the form[6]

$$T = 1/(1 + Z^2). \qquad (2)$$

The authors of Ref. 6 calculated the shape of the differential conductances of N–I–S junctions for any values of Z. Analogous calculations for the current–voltage characteristics of S–I–S heterostructures were done in Ref. 7. There the multiple Andreev reflection processes at barrier biases less than V^* were not taken into account. This means that the quantitative conclusions of Ref. 7 are actually restricted to voltages in the immediate vicinity of V^*, but, as was mentioned above, it is that region that we will be interested in below.

A new circumstance that will be taken into account in the present paper is the influence of nonuniformity of the tunnel barrier on the shape of the current–voltage characteristics of an S–I–S junction. We assume that the effectiveness Z of the barrier is different at different points of the structure under study, and we introduce the corresponding distribution function

$$\Phi(Z) = \frac{1}{Z_1\sqrt{2\pi}} \exp\left[-\frac{1}{2}\left(\frac{Z - Z_0}{Z_1}\right)^2 \right]. \qquad (3)$$

Here Z_0 is the mean value of Z, and Z_1^2 is the variance of the distribution. By varying both parameters Z_0 and Z_1 in the normal distribution law (3), one can describe arbitrary distri-

butions of the barrier characteristics Z, and, by comparing them with the measured curves, establish the degree of non-uniformity of the tunnel junction. We note that distribution (3) can easily be written as a function of the transparency T of the insulating spacer layer by using the relation (2) between these two quantities. The distributions $\Phi(Z)$ used in this study are shown in Fig. 1.

At finite temperature, the final expression for the current–voltage characteristic of an S–I–S structure with a nonuniform potential barrier, which follows from the results of Ref. 7, has the form

$$J(V) = \sum_Z \Phi_N(Z) 2N(0) e V_f A_J (1 + Z)^2$$

$$\times \int_{-\infty}^{\infty} f_0(E) \frac{dE}{2\pi} \int_0^{2\pi} d\varphi \left\{ \frac{g(E)}{g(E) + (1 + 2Z)^2} \right.$$

$$\Theta(E^2 - \Delta_2^2)\Theta[(E - eV)^2 - \Delta_1^2]$$

$$\left. + \frac{g^2(E) - 1}{g^2(E) - (1 + 2Z^2)^2} \Theta(E^2 - \Delta_2^2)\Theta[\Delta_1^2 - (E - eV)^2] \right\}. \qquad (4)$$

Here

$$f_0(E) = [f(E - eV) - f(E)],$$

$$g(E) = h(E) - p(E)\cos\varphi,$$

$$h(E) = \frac{E(E - eV)}{\sqrt{(E^2 - \Delta_2^2)[(E - eV)^2 - \Delta_1^2]}},$$

$$p(E) = \frac{\Delta_1\Delta_2}{\sqrt{(E^2 - \Delta_2^2)[(E - eV)^2 - \Delta_1^2]}},$$

$\Theta(z)$ is the Heaviside step function, $f(E)$ is the Fermi distribution function, $N(0)$ and v_F is the electron density of states and the electron velocity at the Fermi level, and Δ_1
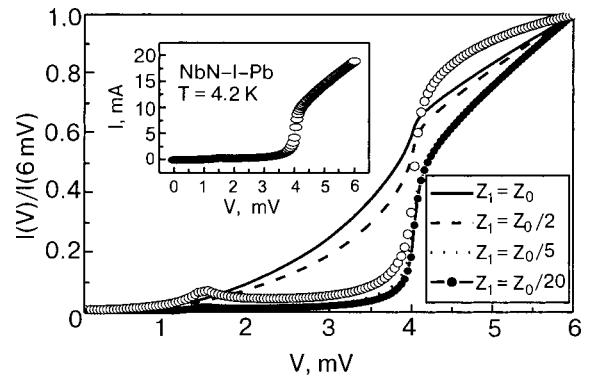

FIG. 2. Calculated value of the tunnel current I, normalized to the value of the current at 6 mV, versus the applied voltage V in the case of the distribution function $\Phi(Z)$ shown in Fig. 1. The circlets show the corresponding experimental data for an NbN–I–Pb junction. In the the calculations, as in the experiment, the temperature was 4.2 K, and the values of the energy gaps at that temperature are $\Delta_{NbN} = 2.95$ meV and $\Delta_{Pb} = 1.25$ meV. The inset shows the original current–voltage characteristic of an NbN–I–Pb tunnel junction.

and Δ_2 are the values of the energy gaps for the two super-conducting electrodes. Below we shall restrict discussion to the case of zero temperature.

Figure 2 shows the results of the calculations using the formulas given above with the parameter $Z_0 = 4$, which gives the best fit of the calculated curves to the current–voltage characteristics of one of the NbN–I–Pb tunnel junctions. Figure 2 demonstrates the influence of the degree of nonuni-formity of the potential barrier on the $I(V)$ curve for N_1–I–N_2 and S_1–I–S_2 junctions. A comparison of the mea-sured and calculated curves in Fig. 2b indicates that in our samples the scatter in the barrier parameters Z_1 is of the order of unity, which is much less than the mean value Z_0. Thus in this case we are dealing with rather small fluctua-tions over the thickness of the potential barrier.

In closing we note that in the course of the present stud-ies we were able to make tunnel junctions based on niobium nitride with quite reproducible electrical characteristics. Moreover, a comparison with the theoretical calculations generalizing the conclusions of Ref. 7 to the case of possible inhomogeneities of the insulating layer shows that the barrier formed as a result of the oxidation of NbN is rather

uniform over thickness. This indicates that the problem posed in the aforementioned review[1]—the creation of Josephson junctions capable of operating with a two-stage cryorefrigerator—may actually be solved with the use of nio-bium nitride.

*E-mail: shat@d24.imp.kiev.ua

[1] R. Compano (ed.), *Technology Roadmap for Nanoelectronics*, Office for Official Publications of the European Communities, Luxembourg (2001).
[2] J. B. Neaton, D. A. Muller, and N. W. Ashcroft, Phys. Rev. Lett. **85**, 1298 (2000).
[3] W. H. Rippard, A. C. Perrella, F. J. Albert, and R. A. Buhrman, Phys. Rev. Lett. **88**, 046805-1 (2002).
[4] Y. Ando, H. Kameda, H. Kubota, and T. Miyazaki, J. Appl. Phys. **87**, 5206 (2000).
[5] E. L. Wolf, *Principles of Electron Tunneling Spectroscopy*, Oxford University Press, New York (1985).
[6] G. E. Blonder, M. Tinkham, and T. M. Klapwijk, Phys. Rev. B **25**, 4515 (1982).
[7] Yu. V. Shlapak, V. E. Shaternik, A. L. Kasatkin, and É. M. Rudenko, Metallofizika i Noveĭshie Tekhnologii **20**, No. 3, 3 (1997).

Translated by Steve Torstveit

Phase-sensitive quantum effects in the Andreev conductance of an SNS system of metals with a macroscopic phase-breaking length

Yu. N. Chiang* and O. G. Shevchenko

B. Verkin Institute for Low Temperature Physics and Engineering, National Academy of Sciences of Ukraine, pr. Lenina 47, 61103 Kharkov, Ukraine

A study is made of the dissipative component of the electron transport in a doubly connected Andreev S–N–S (indium–aluminum–indium) interferometer with elastic mean free paths l_{el} in the metals of around 100 μm and a macroscopic phase-breaking length L_φ that is two or more orders of magnitude larger than L_φ in disordered nanostructures, including two-dimensional ones. The studies are done under conditions not studied before in such interferometers: $\bar{m} < l_{el}$ ($\bar{m}$ is the transverse size of the NS boundaries). At helium temperatures the samples are found to exhibit new phase-sensitive effects of a quantum-interference nature. Conductance oscillations with a period Φ_0/A (Φ_0 is the flux quantum and A is the aperture area of the interferometer) are observed in the non-domain (normal) state of the indium narrowing near the NS boundary. In the domain intermediate state of the narrowing, magneto-temperature resistive oscillations are observed, with a period $2\Phi_0/\xi^2_{H_c(T)}$ ($\xi_{H_c(T)}$ is the coherence length in a magnetic field close to critical). At sufficiently low temperatures ($T \approx 2$ K) the conductance of a macroscopic N region of the system has an oscillatory component of resonance shape which undergoes phase inversion relative to the phase of the nonresonance oscillations. An explanation for the effects is suggested in terms of the contribution to the Josephson current from coherent quasiparticles with energies of the order of the Thouless energy. The temperature behavior of the dissipative transport in a pure normal metal near an isolated NS point contact is investigated. © *2003 American Institute of Physics.* [DOI: 10.1063/1.1630715]

1. INTRODUCTION

Our previous experiments[1–4] with SNS structures based on pure metals established that even at not very low helium temperatures the dependence of the normal conductivity of the structures on the coherent phase difference of the superconducting "banks" can be preserved at distances L between the NS boundaries several orders of magnitude larger than the size L of the normal spacer layers in disordered SNS nanostructures, where quantum interference effects in the dissipative transport were first observed and continue to be widely studied.[5–13] The typical scale L for such structures is of the order of 1 μm and is limited by the phase-breaking length L_φ, which for nanostructures is a quantity of the same order. In metals with an electron elastic mean free path $l_{el} \sim 10^2$ μm the phase-breaking length is at least 10^3 times larger than in nanostructures with $l_{el} \sim 0.01$ μm (in systems with a two-dimensional electron gas $l_{el} \lesssim 1$ μm). The reason is apparently that at static defect densities leading to such values of l_{el} as in nanostructures, inelastic processes come into play in the scattering on these objects, limiting L_φ. At low defect densities in pure metals the contribution of such processes is unimportant. The macroscopic value of L_φ in pure metals allows one to increase the spatial region in which the long-range phase coherence (LPC) is investigated, expanding the interval of values $L/\xi_T > 1$ from values of the order of 10^0 in nanostructures to 10^2 in systems with pure metals.

In addition, we note that the coherence length ξ^d_T

$= \sqrt{\hbar D/k_B T}$ (D is the diffusion coefficient) in the "dirty" (diffusion) limit can be expressed in terms of the coherence length ξ^p_T in the "pure" limit $\xi^p_T \equiv \xi^{bal}_T = \hbar v_F/k_B T$:

$$\xi^d_T = [(1/3) l_{el} \xi^{bal}_T]^{1/2}, \quad l_{el} \ll \xi^{bal}_T.$$

It follows that the temperature regions T^p and T^d which determine the values of L/ξ_T in the pure and dirty samples with distances between NS boundaries L^p and L^d, should be connected by the relation

$$\frac{(T^p)^2}{T^d} = 3 \frac{\hbar v_F}{k_B l^d_{el}} \left(\frac{L^d}{L^p} \right)^2 \left[\frac{(L/\xi_T)^p}{(L/\xi_T)^d} \right]^2. \quad (1)$$

(We are presupposing that the phase-breaking length L_φ in each case is not less than L^p or L^d.) This means that the same values of the parameter $L/\xi_T = \sqrt{T/E_c}$ (E_c is the gap in the density of states),[14] characterizing the same behavior of the phase-coherent phenomena in the two limits, can be realized at very different temperatures—much higher for the pure systems. For example, in pure samples with $l_{el} \gg 1$ μm this parameter at 2 K is of the same order of magnitude as in diffusional samples with $l_{el} \sim 0.01$ μm at $T \lesssim 0.1$ K, for $L^p/L^d \sim 10$. (It will be shown below that the shift of the temperature regions of analogous behavior of the phase-coherent effects for 2DEG samples with $l_{el} \sim 1$ μm (Ref. 11) and 3D samples with $l_{el} \sim 0.01$ μm in the case $L^{3D}/L^{2D} \sim 1$ also corresponds to relation (1).)

Thus a manifestation of phase-coherent phenomena for $L/\xi_T > 1$, which implies the existence of LPC under conditions of an exponentially small (in magnitude) proximity ef-

fect for the main group of electrons, which are excitations with energy $\varepsilon \sim T$, in ultrapure structures can be observed on macroscopic scales even at not very low helium temperatures; this effect may be of extremely topical interest for solving the problem of extracting quantum information from various quantum systems via macroscopic channels, for example.

Generally speaking, the first indications of a long-range (not purely exponential in the parameter L/ξ_T) influence of a superconductor on the conductivity of a normal metal bordering are directly contained already in the results of experiments on structures with an isolated NS boundary, where such an influence has been noted at distances from the boundary corresponding to values $L/\xi_T \sim 5-10$.[15,16] The interference effects subsequently observed in doubly connected SNS systems containing disordered metals (nanostructures) with small L_φ have also been studied until recently in a range of L/ξ_T not exceeding the values indicated above. However, experiment shows that the manifestation of phase-coherent phenomena in doubly connected SNS systems is not limited to this interval of values of the parameter L/ξ_T, and the presently available results on the behavior of phase-coherent phenomena in that interval (see Fig. 7) have been interpreted in different ways; it is therefore necessary to expand the study of these phenomena, especially under conditions of different L/ξ_T ratios unrealizable in disordered nanostructures.

In the present study we have investigated the temperature and phase-sensitive features in the behavior of the conductance of SNS systems formed by the contact of two pure metals with $l_{el} \approx 100 \ \mu$m, aluminum (in the normal state) and indium, in an interferometer geometry for $L/\xi_T \approx 10^2$ under the conditions $L, l_{el} \gg \xi_T = \xi_T^p$. Under these conditions all three dimensions of the normal spacer layer of the SNS system are so much greater than the typical microscopic spatial parameters associated with the proximity effect that the contribution of a supercurrent due to the main group of carriers with energies $\varepsilon \sim T$ can be completely ruled out.

2. EXPERIMENTAL TECHNIQUE

Figure 1 shows a diagram of the overall layout and the equivalent circuit for the measurements (inset) of the investigated doubly connected system of two metals in contact, aluminum and indium. After the transition of the indium to the superconducting state, the system acquires an SNS configuration of the ''Andreev interferometer with cavity'' type. The area of the cavity between the aluminum girder (2 $\times$2 mm in cross section) and the indium strip, soldered at points a and b, was $A = ab \times h \approx 3$ mm$\times 15 \ \mu$m.

Unlike the SNS system which we studied previously in Refs. 3 and 4, which used copper and had wide soldered NS contacts with a characteristic dimension $\bar{m}$ which could not increase the contact resistance R_{cont}, since $\bar{m} \gg l_{el}$, in the present study the current regime was realized through contacts a and b with a significant distributed (Sharvin) resistance R_{Sh}, which usually arises for characteristic contact dimensions smaller than l_{el} (Ref. 17). Contacts of such a size were formed by spot welding the indium to the aluminum used in the present study. Here, as we have repeatedly confirmed in previous studies, the direct welding of ultrapure
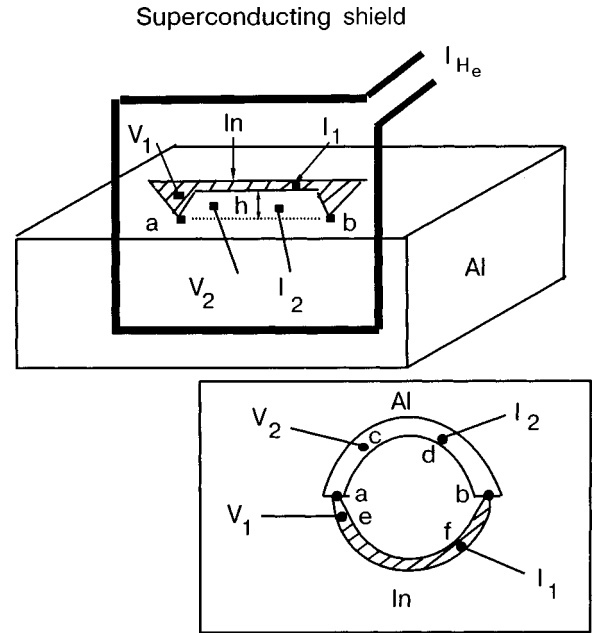

FIG. 1. Schematic illustration of the SNS interferometer and the equivalent circuit of the measurements (inset). The shaded region is the bulk part of the indium.

materials with ratios of the resistances at 300 and 4.2 K of $RRR \gtrsim 10^4$ ($l_{el} \approx 100 \ \mu$m) brings about a close to zero barrier height z in the contacts, which corresponds to a transmission coefficient $t = (1 + z^2)^{-1} \approx 1$ (Ref. 18; $z \neq 0$ for technologies that do not partially or completely destroy the oxide layer or other kinds of contamination on the surface of the metals).

The characteristic dimensions of the contacts a and b (see Fig. 1) can be estimated by noting that for $l_{el} > \bar{m}$ the total current through a contact of two metals in the normal state should be related to the contact area $\mathcal{A}_{cont}$ by the expression[18]

$$I_{NN} = 2\nu(\varepsilon)e^2 v_F \mathcal{A}_{cont} U_{Sh} t \equiv U_{Sh}/R_{Sh}, \qquad (2)$$

where $\nu(\varepsilon)$ is the density of states in one of the metals of the contact, and U_{Sh} is the voltage drop across the distributed resistance R_{Sh}. Choosing aluminum as the 3D part of the system, with a normal conductivity of $\sigma_N = (1/3)e^2 v_F \nu(\varepsilon) l_{el}$, and taking into account that $I_{NN} = j^{Al} A^{Al} = j_{cont} \mathcal{A}_{cont}$ (j^{Al} and j_{cont} are the current density in the aluminum and in the contact, respectively), we obtain from (2) the area over which the two metals touch:

$$\mathcal{A}_{cont} = (1/6)(l_{el}^{Al}/L^{Al})(U^{Al}/U_{Sh})A^{Al}. \qquad (3)$$

Here $A^{Al} \approx 4$ mm^2 is the cross section of the aluminum girder, $L^{Al} \approx 1.5$ mm is the length of the corresponding part of the Al between one of the contacts, e.g., a, and the measuring probe V_2 (ac in Fig. 1), with a potential difference across this part equal to $U^{Al} = I_{NN} R^{Al}$, where R^{Al} is the resistance of that part, measured independently in the case when the second contact is excluded. By measuring the voltage U across the probes V_1 and V_2 in this scheme, one can find the voltage drop across the distributed resistance as

$$U_{Sh} = U - I_{NN}(R_{Al} + R_{narr,N}^{In}),$$

where $R^{In}_{narr,N}$ is the resistance of the indium narrowing in the normal state in the near-contact region (see the inset in Fig. 1). Measurements of the quantities necessary for evaluating $\mathcal{A}_{cont}$ gave the following results: $R^{Al} \approx 4 \times 10^{-10} \, \Omega$; $R_{Sh} \approx 1.1 \times 10^{-8} \, \Omega$; $R^{In}_{narr,N} \approx 1.7 \times 10^{-8} \, \Omega$. In accordance with (3) we find that the characteristic ''spot'' size $\bar{m}$ in contacts a and b could be around 25 μm, which corresponds to the inequality $l_{el} > \bar{m}$ which gives rise to an additional distributed resistance of the residual type, which in our experiment exceeds the resistance of the N-metal segment ac of the system by two orders of magnitude.

After the contacts were formed, the indium narrowing at contact b was thinned (by drawing) so that the resistance of the interferometer branches dbf and daf (inset in Fig. 1) were in a relation $R_{dbf} \gg R_{daf}$ ($R_{dbf} = R^{In}_{b,narr} \sim 10^{-3} \, \Omega$). The measuring current was introduced to the system through normal probes, one of which, I_1, was mounted in the indium outside the narrowing region and the second, I_2, was in the aluminum. For resistances of contacts a and b obeying the above relation, practically all of the conduction current flowed along the loop I_1–indium narrowing–contact a–aluminum–I_2. The possibility of regulating a macroscopic phase difference is preserved.

The macroscopic phase difference in the interferometer was controlled by an external magnetic field H_e produced by a rectangular wire loop glued directly on the face of the aluminum girder and carrying a current I_{H_e}. The planes of the loop and interferometer cavity were parallel to each other, the cavity lying along the axial line of the loop, a position convenient for calculation of the value of the field produced in the cavity by the loop. For compensation of external fields the sample with the loop was placed in a closed superconducting shield. The normal (copper) probes V_1 and I_1 were soldered to the indium, and V_2 and I_2 were spot welded to the aluminum. The potential difference across the probes V_1 and V_2 was measured to an error of $(0.5-1) \times 10^{-12}$ V or better by a device utilizing a thermomagnetic superconducting modulator,[19] which made it possible, in particular, to study the effects down to 0.1% in the conductance of an N region of macroscopic dimensions. The error for the measurements of the working currents and temperature was 0.01–0.001%.

3. RESULTS AND DISCUSSION

3.1. $H_e = 0$. Temperature dependence

Figure 2 (curves *1* and *2*) shows the temperature dependence of the potential difference U, divided by the working current ($I \approx 0.5$ A) introduced to the system through probes I_1 and I_2 of the interferometer (Fig. 1) in the case $R^a_{cont} \ll R^b_{cont}$. At the transition through the critical temperature of the bulk part of the indium, $T^{In}_c = 3.41$ K, where an NS boundary appears, a jumplike increase in the resistance of the part cae of the system is observed; this jump is like that which was first observed by the authors in 1988[15] and is a characteristic quantum effect accompanying the appearance of Andreev reflection.[20]

An analysis of the values given in the previous Section for the contributions to the resistance from individual elements of the system and curves *1* and *2* in Fig. 2 implies,
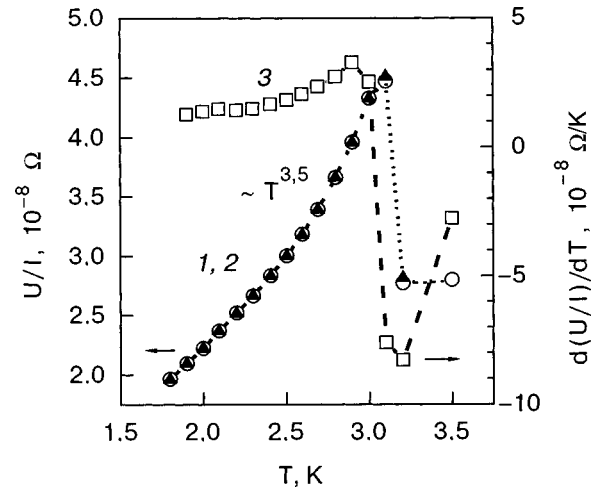

FIG. 2. Temperature dependence of the resistance of the indium narrowing at the contact a of the interferometer for $R^a_{cont} \ll R^b_{cont}$ (curves *1* and *2*) and its derivative (curve *3*). Curves *1* ($\bigcirc$) and *2* ($\blacktriangle$) are the measurements at the minimum ($H_e = 0$) and maximum ($H_e = 0.3$ mOe), respectively, of the resistive oscillations observed at 3.2 K. The jump on curves *1* and *2* corresponds to a twofold increase in the resistance of the indium narrowing when the NS boundaries appear (the values include the distributed resistance of the contact).

first, that the resistance jump near T^{In}_c and the subsequent change in the resistance of the system in the temperature interval down to ~ 1.8 K can only be due to the resistance of the indium narrowing (R_{Sh} is independent of temperature, and $R_{Al} \ll R^{In}_{narr,N}$). A comparison of the values of the resistance of the indium narrowing in the NN state ($\approx 1.7 \times 10^{-8} \, \Omega$ at $T = 3.5$ K) and for the NS configuration of the system ($\approx 3.4 \times 10^{-8} \, \Omega$ at $T = 3.2$ K) indicates a twofold increase in the resistance of the narrowing.

According to the microscopic theory,[21,22] such an increase in the normal resistance upon the onset of Andreev reflection, due to the twofold increase in the cross section for electron scattering on normal-metal impurities located within the coherence length ξ^p_T of the NS boundary (of the order of 10 μm for In at $T \approx 3$ K), can take place under the condition $L \sim \xi^p_T$, where L is the dimension of the metal layer reckoned from the boundary. A simple estimate of the dimensions of the narrowing with the use of the values $RRR_{In} \approx 4 \times 10^4$, $\mathcal{A}_{cont}$, and R^{In}_{narr} shows that the size of the narrow boundary region of indium, L_{narr} (i.e., the distance from the ''spot'' to the place of the transition to the bulk part of the indium, where an NS boundary arises for $T < T^{In}_c$) is of the order of 10 μm, i.e., comparable to ξ^p_T. Thus the conclusion of the theory that a twofold increase in resistance will occur upon the onset of Andreev reflection under the conditions $L_{NS} \sim \xi_T$ has apparently found its first direct confirmation. Previously the largest resistance increase that we had been able to observe did not exceed 60%.[23]

Curves *2–5* in Fig. 3 show the results of measurements of the conductance on the opposite side from contact a, on the normal aluminum side, as functions of the thickness of the normal layer adjacent to the NS boundary, i.e., on the distance L_{NS} between the normal probe N and the superconducting (S) point contact a. Measurements were made with the interferometer ring broken, permitting the use of a four-contact null method of measurement (see the inset in Fig.
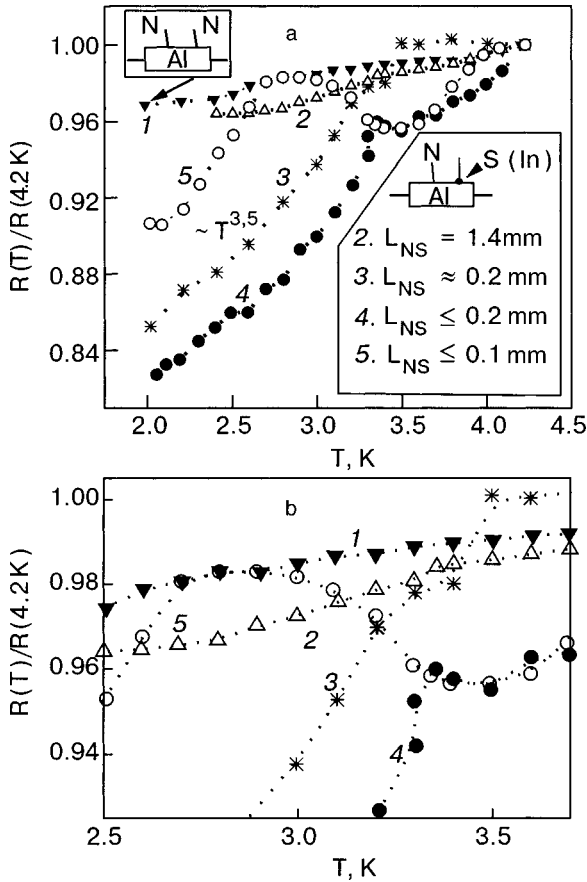
FIG. 3. Dependence of the rise of the resistance of aluminum near the boundary (in region ac, Fig. 1) on the distance between the N probe and the NS boundary; $H_e = 0$.

FIG. 4. Current–voltage characteristic for the smallest distance between the N probe and NS boundary (in the geometry $L_{NS} \leqslant 0.1$ μm, corresponding to the distance L_{NS} for which curve 5 in Fig. 3 was measured) and its derivative. $T = 3.2$ K, $H_e = 0$.

3a), which eliminated the contribution $R_{Sh} + R_{narr}^{In}$ of the contact itself. Also shown for comparison in this figure is the temperature dependence of the resistance of the same aluminum (curve *1*) measured with the use of only normal probes that had been arc-welded on.

The curves in Fig. 3 (Figure 3a and 3b differ only in scale) demonstrate how the increase of the resistance of the near-contact layer in the aluminum upon the formation of an NS boundary evolves as with changing L_{NS}. It follows from a comparison of the curves in Figs. 2 and 3 that the change in resistance (an increase with decreasing temperature) upon the formation of an NS boundary, observed on both sides of the point contact a, is analogous to the effects observed in NS systems with pairs of different metals for an arbitrary area of the NS boundaries and for other positions of the probes.[2,23] The nature of the effect, as we have said, is due to the interference of coherent electrons appearing upon Andreev reflection, and its value under the conditions $L_\varphi \gg l_{el} \gg \xi_T$ depends only on the ratios $\xi_T/L_{NS}, l_{el}$ if $L_{NS} < L_\varphi$.

The results given in Fig. 3 again confirm that LPC can be maintained in a pure metal in the investigated temperature range over macroscopic distances, in our case at least 1.5 mm ($L/\xi_T \approx 10^2$), which, as before,[1–4,23] indicates that the phase-breaking length is of at least that scale.

It also follows from Figs. 2 and 3 that the temperature dependences of the resistance of both the indium and aluminum, measured on the two sides of the NS boundary a, in the low-temperature region of the jump and where $\xi_T < L_{NS}$ obey
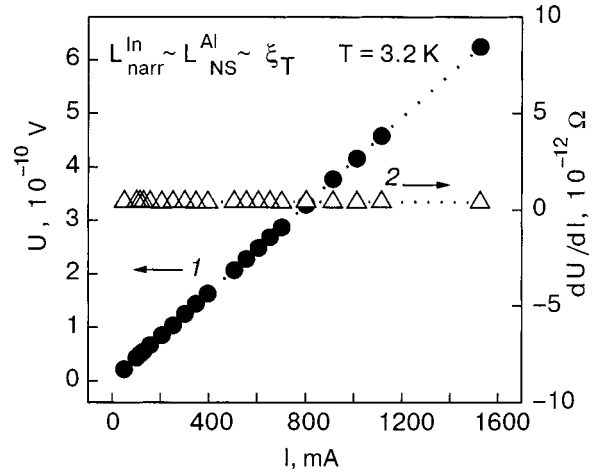
the same power law ($\sim T^{3.5}$) and correspond to our previous result for aluminum, obtained in an NS system with a different method of measurement.[2] This fact provides additional confirmation of the role of the temperature dependence of the phase-breaking length in determining the temperature dependence of the conductance of a metal layer as a whole within the range $\xi_T < L_{NS} < L_\varphi$ under conditions of multiple Andreev reflection (see Ref. 2).

Figure 4 shows the current–voltage characteristic (curve *1*) measured at a temperature of 3.2 K and corresponding to case *5* in Fig. 3, and its derivative (curve *2*). It is seen that there are no nonlinear effects associated with the contact over a wide range of currents, including the measuring current 0.2–0.5 A.

3.2. $H_e \neq 0$

3.2.1. Nonresonance oscillations

In measurements of the potential difference U across probes V_1 and V_2 at a temperature of 3.2 K, depending on the magnetic field H_e of the wire loop, a component oscillatory in H_e with a period $(hc/2e)/A$ is observed, where A is the area in the gap h (see Fig. 1). The amplitude of the
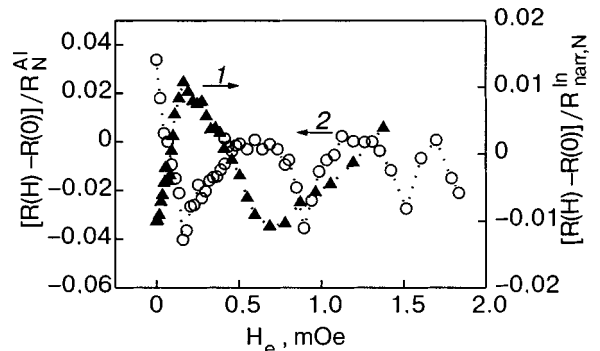

FIG. 5. Nonresonance oscillations of the phase-sensitive dissipative component of the resistance at $T = 3.2$ K in the indium narrowing (curve *1*) and the resonance oscillations of this component at $T = 2$ K in the aluminum (curve *2*) for an interferometer with $R_a \ll R_b$, as functions of the external magnetic field.

oscillatory component, shown by curve *1* of Fig. 5 in relative units, $U/I \propto (R_H - R_{H=0})/R_{H=0}$, has a value in absolute units $\Delta(U/I) = (R_{max} - R_{min}) \approx 4.5 \times 10^{-10}$ Ω, which corresponds to ≈2% of the resistance of the indium narrowing, $R_{narr,SN}^{In}$, with $R_{min} \equiv R_{H=0}$. Figure 6 shows the temperature dependence of the difference $\Delta(U/I) = (R_{H=0.3 \text{ mOe}} - R_{H=0})$, which, like the character of the temperature dependence of $d(U/I)/dT$ (curve *3* in Fig. 2), indicates that a domain intermediate state of the indium narrowing is realized on decreasing temperature no earlier than ≈3.1 K, as is indicated by the temperature position of the jumps on the corresponding curves. The same conclusion also follows from an independent analysis with the use of the size L_{narr}, which does not correspond to the condition for the onset of a domain structure with more than 1 domain in the presence of the self-magnetic field of the current (~10 Oe), since it is not comparable to the size of the domains for $T > 3.1$ K.[3] The transition of the narrowing to the domain intermediate state is evidenced by the appearance, at temperatures below 3 K, of magnetotemperature resistance oscillations with a period corresponding to the period of oscillations in the critical magnetic field, $\Delta_{H_c(T)} \sim hc/e\xi_H^2$, with $\xi_H \approx 2\sqrt{qR_L[H_c(T)]}$ ~1 μm for 3.0 K (q is the screening radius of the impurity, and $R_L(H_c)$ is the Larmor radius).[1,3]

Let us compare the parameters of the oscillations observed at 3.2 K (curve *1* in Fig. 5) with the theory and the presently available results of other authors. The most characteristic results[7,11,13] on the temperature dependence of the relative amplitudes $|\Delta R/R_N|$ of the observed resistive oscillations are collected in Fig. 7, where they are plotted as functions of the parameter $T_{Th}/T \equiv (\xi_T/L)^2$ with the values of the "Thouless temperatures" T_{Th} adopted by the authors. Also shown there is the theoretical curve $|\Delta R/R_N| = |R_{max} - R_N|/R_N$, where R_{max} and R_N are the values of the resistances at the maximum and minimum of the oscillations, which were obtained in Ref. 24 by a numerical simulation
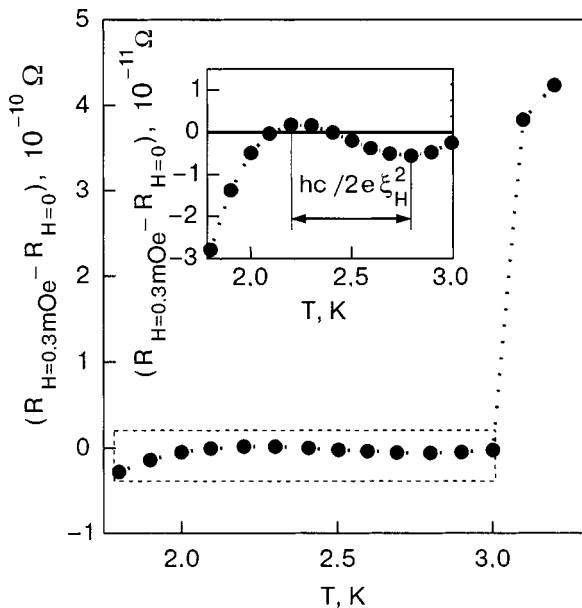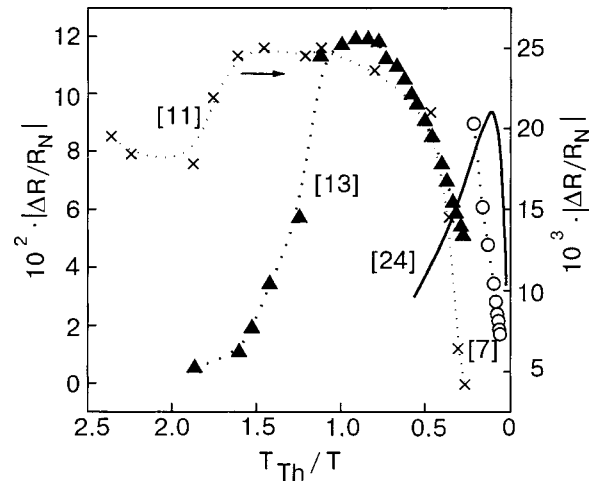

FIG. 7. Temperature dependence of the amplitude of the phase-sensitive nonresonance oscillations of the conductance from the experimental papers.[7,11,13] The solid curve is the theory.[24]

for $\varphi = \pi$ and $\varphi = 0$, respectively, with $T_{Th} = D/\pi L^2$. The apparent disagreement of the experimental results on the parameter $T_{Th}/T = (\xi_T/L)^2$ with the theory and with each other is eliminated practically completely if the gap that arises in the density of states upon localization by Andreev reflections of the coherent excitations in the normal space between the NS boundaries is everywhere taken equal to the energy criterion $T^* = D/2\pi L^2$ for the "dirty" limit from Ref. 25. Figure 8b shows the same results as in Fig. 7 but plotted with the "Thouless temperature" taken equal to the parameter T^* in the form indicated above, with L taken equal in all cases

FIG. 6. Temperature dependence of the difference of the resistances for $H_e = 0.3$ mOe and $H_e = 0$ for an interferometer with $R_a \ll R_b$ (the inset shows the dependence on an expanded scale).
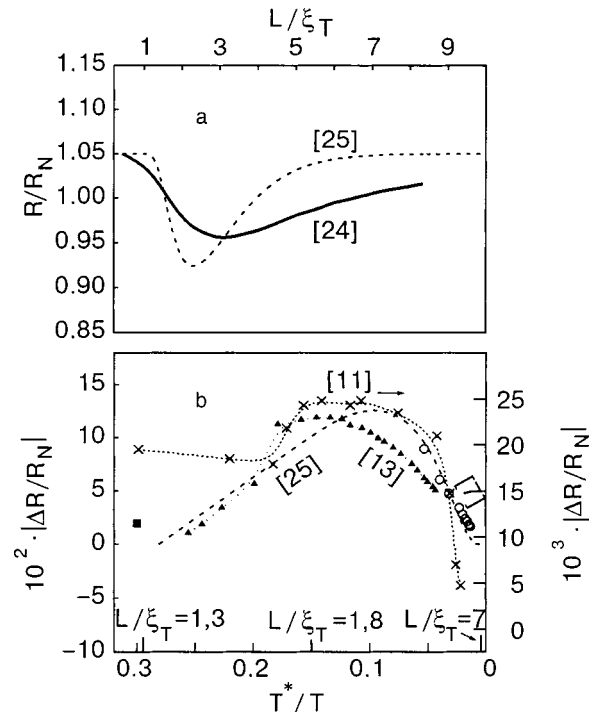

FIG. 8. Dependence of the resistance of an SNS system on the parameter L/ξ_T from Refs. 24 and 25 (a) and the temperature dependence of the amplitude of the nonresonance oscillations of the conductance from Refs. 7, 11, and 13 (see Fig. 7) after modification in accordance with the theory of Ref. 25 (b); ■—the amplitude of the nonresonance oscillations in our experiment.

to the distance between the superconducting "mirrors." It is seen that the set of experimental results thus modified forms a regular relation in the behavior of the amplitude of the oscillations with respect to the parameter T^*/T. As it turned out, this feature follows directly from the results of a theoretical analysis carried out back in 1968 by Aslamazov, Larkin, and Ovchinnikov.[25] Indeed, using the fact that the quasiparticle dissipative current ($\sim f(\cos \Delta\chi)$, where $\Delta\chi$ is the macroscopic phase difference) is the difference between the total current and the supercurrent,[26] we find on the basis of the analytical expressions for the nondissipative current ($\sim \sin \Delta\chi$) given in Ref. 25

$$\frac{R_{\Delta\chi=\pi/2}}{R_N} = \left[1 - \frac{1}{\pi} \frac{L}{\xi_T} \exp\left(-\left(\frac{L}{\xi_T} + 1 \right) \right) \right.$$
$$\left. \times \ln\left(\alpha \left(\frac{L}{\xi_T} \right)^{-2} \right) \right]^{-1}, \tag{4}$$

where $L/\xi_T \equiv (T/T^*)^{1/2}$ and α is a coefficient of the order of unity.

The curve corresponding to this expression for $\alpha = 2$ is shown in Fig. 8a together with the curve for $R_{\Delta\chi=0}/R_N$ from Ref. 24. It is easy to see that both results predict the existence of LPC, i.e., nonexponential damping of the oscillatory dissipative component in the conductance of an SNS system for $L/\xi_T \gg 1$. The positions of the curves on the L/ξ_T scale do not coincide because of the difference of a factor of $\sqrt{2}$ between ξ_T in Refs. 24 and 25. The theoretical curve for the relative amplitude of the oscillations, $|\Delta R/R_N|$, corresponding to the curve from Ref. 25 in Fig. 8a, is shown by the dashed curve in Fig. 8b. It is seen that it describes completely the position on the temperature scale of all the experimental results presented in Fig. 7, confirming the conclusion about the relationship of the temperature intervals made on the basis of expression (1). (In processing the results of Ref. 11 we took into account that the size of the normal region in one of the directions is greater than l_{el} and does not satisfy the ballistic criterion ξ_T^p, and we were forced to make a substantial re-evaluation of the Thouless temperature.) The same curve also gives a correct quantitative estimate of the oscillation amplitude $|\Delta R/R_N|$ in the corresponding temperature intervals, except for the values given in Ref. 11, where the authors chose for R_N not the resistance of the region between the "mirrors," as required, but the resistance of the whole sample.

In contrast to the experimental results discussed,[7,11,13] the region of observation of which, as an analysis shows, most likely corresponds to the region of values $L/\xi_T > 1$ ($T^*/T < 0.3$), i.e., the "dirty" limit, the oscillations pertaining to the indium narrowing in the contact at 3.2 K, as was shown, are reasonably attributed to the quasiballistic oscillation regime, $L_{narr}^{In}/\xi_T \sim 1$. For this regime the characteristic temperature is $T^{bal} = \hbar v_F/k_B L$. The position of the oscillation amplitude (the square data point in Fig. 8b) calculated with the use of this parameter for $L = L_{narr}^{In}$ is also in agreement with the theoretical curve from Fig. 8b.

3.2.2. Resonance oscillations

The oscillations shown by curve *2* in Fig. 5 are at first glance surprising from the standpoint of the dimensions of the system. These oscillations, which have a resonance shape, are observed at temperatures of ~ 2 K and differ from the oscillations measured at 3.2 K. Since at 2 K the resistance of the indium narrowing is already comparable in value to the resistance of the aluminum on the segment ac (see the inset in Fig. 1) and the phase of the resonance oscillations is shifted by π with respect to the phase of the nonresonance oscillations at 3.2 K, it can be assumed that the nature of the resonance oscillations is due to features of the phase-coherent interference in the aluminum. The period of these oscillations, like that of the oscillations observed at 3.2 K, is equal to $(hc/2e)/A$. (The above-mentioned phase inversion of the resistive oscillations has also been observed in other studies (e.g., Refs. 11 and 13) in a different geometry of the SNS interferometers (nanostructures) and with another method of measurement.)

First, as we emphasized before, in the system which we investigated the phase-breaking length is either much larger than the distance between electron injectors, as is the case in the indium narrowing in the domain state, or is of the order of that distance, as in the aluminum region (~ 1 mm); this is the first necessary condition for the manifestation of quasiparticle phase-coherent phenomena in the conductance of systems with a large distance between boundaries. The next fundamental argument, which was examined in detail in the theory of Ref. 27, is the restriction imposed on the possibility of establishing a coherent phase difference under these conditions. It concerns the dimensions of the injectors, which, playing the role of reservoirs, should, in particular, in the ballistic transport regime (like the regime in the indium narrowing) bring about a splitting of the electron beam at the place where the injectors are joined (at least, one of them). This is required for the creation of conditions of no return to the injector for a hole excitation after the first Andreev reflection, under which it is possible to form quasiclassical trajectories of low-energy electrons with energies $\varepsilon \lesssim E_c \sim \hbar v_F/L$ (or $\hbar D/2\pi L^2$); these trajectories connect the two superconducting "mirrors" and thereby establish the coherent phase difference between "mirrors." It has been shown that for this to take place in the regime indicated, the aperture of the injector–reservoir should not exceed the de Broglie wavelength λ_B (this circumstance was first pointed out in Ref. 28). It is not hard to understand that this restriction loses meaning if the role of at least one of the injectors is played by one of the superconducting "banks," since in that case splitting is not required for the formation of a trajectory connecting the two superconducting "banks." In our SNS system, where the current is introduced through one of the "mirrors" (Fig. 1), there is no restriction on the formation of a coherent phase difference, both for the indium narrowing, which is found in the ballistic regime, and for the aluminum region, which is in a regime that is close to diffusional.

Since the characteristic energy scale of the Andreev spectrum $\sim \hbar v_F/L$, one can assume that the oscillations observed at 2 K are due to the fine Andreev spectrum of low-energy electrons in the aluminum region, since the oscillations in the narrowing ($T = 3.2$ K) do not have a resonance shape, nor do the conductance oscillations of the normal region (Cu) in the case of a large area of the "mirrors" when the current is not introduced through a "mirror."[4] If the

observed oscillation amplitude is attributed to the resistance of the aluminum between the ''mirrors,'' then, as is seen in Fig. 5, the relative amplitude of the oscillations of resonance shape amounts to about 4%, which corresponds to the ratio $E_c(L_{acb}^{Al})/T$ for the aluminum and not for the narrowing. According to the theory of Refs. 27 and 29, the appearance of oscillations of resonance shape can be expected because of degeneracy at the Fermi level of transverse modes with the energies of the Andreev levels

$$\varepsilon_n^\pm = \frac{\hbar v_F}{2L}[(2n+1)\pi \mp \Delta\chi]$$

($\Delta\chi$ is the macroscopic coherent phase difference between the ''mirrors''), when $\Delta\chi = (2n+1)\pi$ ($\varepsilon_n^\pm = 0$). The degeneracy condition thus presupposes an inversion of the phase of the resonance oscillations with respect to the phase of the nonresonance oscillations, which corresponds to $\Delta\chi = 2n\pi$. Such an inversion does take place for the oscillations of resonance shape which we observed.

CONCLUSIONS

The phase-coherent component of the dissipative electron transport in doubly connected hybrid systems with pure metals (In and Al) with elastic mean free paths of the order of 100 μm and a phase-breaking length of over 1 mm has been investigated at helium temperatures. The studies were done in the geometry of an Andreev SNS interferometer with In in the superconducting and Al in the normal state, with a characteristic size of the NS boundaries less than the mean free path and with the length of the normal region between boundaries comparable to the macroscopic phase-breaking length. In dissipative transport, when the current is introduced both through one of the NS boundaries and in an arrangement bypassing the boundaries, a number of phase-sensitive effects of a quantum interference nature are observed, which are indicative of the presence of a coherent component due to Andreev reflections. The effects pertaining to the different regions of the SNS system are separated.

Resistive oscillations with a period Φ_0/A (Φ_0 is the flux quantum, A is the aperture area of the interferometer) are observed, associated with the behavior of the electron transport in the indium narrowing at the boundary in the non-domain (normal) state of the narrowing. The appearance of the observed oscillations of a magnetotemperature character, with a period $2\Phi_0/\xi_{H_c(T)}^2$ ($\xi_{H_c(T)}$ is the coherence length in a magnetic field equal to the critical), are attributed to the domain intermediate state.

For $T \lesssim 2$ K we have observed resistive oscillations of a resonance shape which undergo phase inversion (a shift by π) with respect to the phase of the nonresonance oscillations; we attribute their appearance to the macroscopic normal region of the system (Al) and link to the degeneracy at the Fermi level of transverse modes of the Andreev spectrum of coherent quasi-particles with energies of the order of the Thouless energy.

We have studied the temperature behavior of the phase-coherent component of the transport in a pure metal near an isolated NS point contact.

The appearance of resonance phase-sensitive oscillations for a macroscopic distance L between boundaries in the normal region of the SNS system is attributed to the contribution of coherent excitations with the Thouless energy, for which the transport regime between the reservoir and the NS boundaries in the pure metal ($l_{el} \gg \xi_T^{bal}$) can be ballistic. Since under these conditions when an NS boundary is used as one of the electron injectors the appearance of phase coherence does not depend on L as long as $L \lesssim L_\varphi$, one can assume that the possibility of observation of phase-sensitive effects in the conductance of macroscopic SNS systems is restricted to such values of L for which the normal reflection becomes predominant at the NS boundaries. The latter will take place for $E_c/T < \sqrt{E_c/\varepsilon_F}$ (Ref. 27), which corresponds, for $L_\varphi \to \infty$ and $T \sim 2$ K, to $L > 10$ cm—the limiting scale of interboundary distance for which the appearance of long-range phase coherence is possible at helium temperatures ($L/\xi_T^{bal} \sim 10^4$).

The experimentally observed phase-sensitive quantum effects in the conductance of an SNS system of pure metals in the region of not very low helium temperatures with $L/\xi_T^{bal} \sim 10^2$ find a completely reasonable explanation in the framework of the indicated scale of long-range phase coherence due to the contribution of low-energy coherent excitations with energies $E_c \ll T, \Delta$.

[1] Yu. N. Chiang, JETP Lett. **71**, 334 (2000).

[2] Y. N. Chiang, S. N. Gritsenko, and O. G. Shevchenko, Zh. Éksp. Teor. Fiz. **118**, 1426 (2000) [JETP **91**, 1235 (2000)].

[3] Yu. N. Chiang and O. G. Shevchenko, Fiz. Nizk. Temp. **27**, 1357 (2001) [Low Temp. Phys. **27**, 1000 (2001)].

[4] Yu. N. Chiang and O. G. Shevchenko, JETP Lett. **76**, 670 (2002).

[5] V. T. Petrashov, V. N. Antonov, P. Delsing, and T. Claeson, Phys. Rev. Lett. **70**, 347 (1993); **74**, 5268 (1995).

[6] A. Dimoulas, J. P. Heida, B. J. van Wees, T. M. Klapwijk, W. van de Graaf, and G. Borghs, Phys. Rev. Lett. **74**, 602 (1995).

[7] H. Courtois, Ph. Gandit, D. Mailly, and B. Pannetier, Phys. Rev. Lett. **76**, 130 (1996).

[8] P. Charlat, H. Courtois, Ph. Gandit, D. Mailly, A. F. Volkov, and B. Pannetier, Phys. Rev. Lett. **77**, 4950 (1996).

[9] H. Takayanagi and T. Akazaki, Phys. Rev. B **52**, R8633 (1995); Physica B **249–251**, 462 (1998).

[10] S. G. den Hartog, B. J. van Wees, Yu. V. Nazarov, T. M. Klapwijk, and G. Borghs, Physica B **249–251**, 467 (1998).

[11] E. Toyoda and H. Takayanagi, Physica B **249–251**, 472 (1998).

[12] P. G. N. de Vegvar, T. A. Fulton, W. H. Mallison, and R. E. Miller, Phys. Rev. Lett. **73**, 1416 (1994).

[13] A. Kadigrobov, L. Y. Gorelik, R. I. Shekhter, M. Jonson, R. Sh. Shaikhaidarov, V. T. Petrashov, P. Delsing, and T. Claeson, Phys. Rev. B **60**, 14589 (1999).

[14] F. Zhou, P. Charlat, B. Spivak, and B. Pannetier, J. Low Temp. Phys. **110**, 841 (1998).

[15] Yu. N. Tszyan (Chiang) and O. G. Shevchenko, Fiz. Nizk. Temp. **14**, 543 (1988) [Sov. J. Low Temp. Phys. **14**, 299 (1988)].

[16] V. T. Petrashov, V. N. Antonov, S. V. Maksimov, and R. Sh. Shaĭkhaĭdarov, JETP Lett. **58**, 49 (1993).

[17] Yu. V. Sharvin, Zh. Éksp. Teor. Fiz. **48**, 984 (1965) [Sov. Phys. JETP **21**, 655 (1965)].

[18] G. E. Blonder, M. Tinkham, and T. M. Klapwijk, Phys. Rev. B **25**, 4515 (1982).

[19] Yu. N. Chian, Prib. Tekh. Éksp. , No. 1, 202 (1981).

[20] A. F. Andreev, Zh. Éksp. Teor. Fiz. **46**, 1823 (1964) [Sov. Phys. JETP **19**, 1228 (1964)]; Zh. Éksp. Teor. Fiz. **49**, 655 (1965) [Sov. Phys. JETP **22**, 455 (1966)].

[21] J. Herath and D. Rainer, Physica C **161**, 209 (1989).

[22] A. M. Kadigrobov, Fiz. Nizk. Temp. **19**, 943 (1993) [Low Temp. Phys. **19**, 671 (1993)]; A. M. Kadigrobov, R. I. Shekhter, and M. Jonson, Physica B: Condens. Matter **218**, 134 (1996).

[23] Yu. N. Chiang and O. G. Shevchenko, Fiz. Nizk. Temp. **25**, 432 (1999) [Low Temp. Phys. **25**, 314 (1999)].

[24] Yu. V. Nazarov and T. H. Stoof, Phys. Rev. Lett. **76**, 823 (1996).

[25] L. G. Aslamazov, A. I. Larkin, and Yu. N. Ovchinnikov, Zh. Éksp. Teor. Fiz. **55**, 323 (1968) [Sov. Phys. JETP **28**, 171 (1969)].

[26] A. I. Svidzinskiĭ, *Spatially Inhomogeneous Problems in the Theory of Superconductivity* [in Russian], Nauka, Moscow (1982).

[27] H. A. Blom, A. Kadigrobov, A. M. Zagoskin, R. I. Shekhter, and M. Jonson, Phys. Rev. B **57**, 9995 (1998-II).

[28] B. Z. Spivak and D. E. Khmel'nitskiĭ, JETP Lett. **35**, 412 (1982).

[29] I. O. Kulik, Zh. Éksp. Teor. Fiz. **57**, 1745 (1969) [Sov. Phys. JETP **30**, 944 (1970)].

Translated by Steve Torstveit